JYU DISSERTATIONS 395

Samuli Heiskanen

Application of Direct Laser Writing for the Fabrication of Superconducting Tunnel Junctions and Phononic Crystal Structures

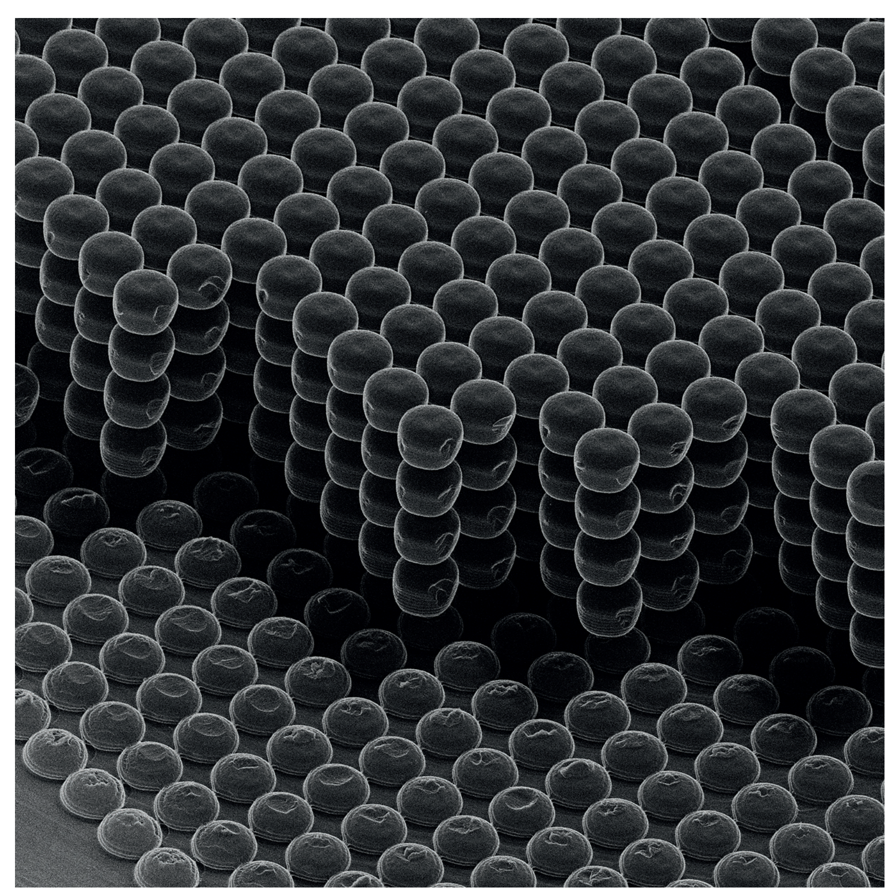

UNIVERSITY OF JYVÄSKYLÄ
FACULTY OF MATHEMATICS AND SCIENCE

JYU DISSERTATIONS 395

Samuli Heiskanen

Application of Direct Laser Writing for the Fabrication of Superconducting Tunnel Junctions and Phononic Crystal Structures

Esitetään Jyväskylän yliopiston matemaattis-luonnontieteellisen tiedekunnan suostumuksella julkisesti tarkastettavaksi kesäkuun 18. päivänä 2021 kello 12.

Academic dissertation to be publicly discussed, by permission of the Faculty of Mathematics and Science of the University of Jyväskylä, on June 18, 2021 at 12 o'clock noon.

JYVÄSKYLÄN YLIOPISTO
UNIVERSITY OF JYVÄSKYLÄ

JYVÄSKYLÄ 2021

Editors
Ilari Maasilta
Department of Physics, University of Jyväskylä
Ville Korkiakangas
Open Science Centre, University of Jyväskylä

Copyright © 2021, by University of Jyväskylä

ISBN 978-951-39-8696-4 (PDF)
URN:ISBN:978-951-39-8696-4
ISSN 2489-9003

Permanent link to this publication: http://urn.fi/URN:ISBN:978-951-39-8696-4

ABSTRACT

Heiskanen, Samuli
Application of Direct Laser Writing for the Fabrication of Superconducting Tunnel Junctions and Phononic Crystal Structures
Jyväskylä: University of Jyväskylä, 2021, 83 p. (+included articles)
(JYU Dissertations
ISSN 2489-9003; 395)
ISBN 978-951-39-8696-4 (PDF)

Phononic crystals (PnC) are periodic structures analogous to the more common photonic crystals. Instead of a periodic dielectric constant they have a periodic elasticity and density, and thus they alter the flow of vibrational energy (heat and/or sound) through a material. This thesis focuses on the fabrication of three-dimensional (3D) PnC structures, integration of tunnel junction devices with them and studying their thermal properties.

The 3D PnC structures, which in this case are 3D square lattices of spheres, were fabricated with 3D lithography using established methods. However, getting the exact wanted geometry required a lot of work and thus part of the thesis revolves around the optimization of the design. Then we had to develop a method for the fabrication of measurement electronics on these 3D structures as no conventional methods really allow such fabrication.

Next we wanted to prove that the developed method can produce the necessary measurement devices. In this case the devices are superconductor-insulator-normal metal-insulator-superconductor (SINIS) junction pairs. We show that the method can produce good quality SINIS junctions, both on a flat substrate and on a 3D structure, using low-temperature measurements.

The last part of the thesis focuses on the thermal conductance measurements of the fabricated PnC structures. These measurements were made for two different PnC structures with sphere diameters of 3.1 μm and 5.0 μm, and also for a control bulk structure with the same geometry. The results of these measurements are compared to finite element method simulations made with a ballistic model.

Keywords: Phononic crystal, 3D lithography, thermal conductance, low temperature

Author Samuli Heiskanen
Department of Physics
University of Jyväskylä
Finland

Supervisor Professor Ilari Maasilta
Department of Physics
University of Jyväskylä
Finland

Reviewers Professor Sami Franssila
Aalto University
Finland

Associate Professor Bartlomiej Graczykowski
Adam Mickiewicz University
Poland

Opponent Directeur de recherche Olivier Bourgeois
Institut Néel CNRS
France

TIIVISTELMÄ (FINNISH ABSTRACT)

Heiskanen, Samuli
Suoran Laserpiirron Käyttö Suprajohtavien Tunneliliitosten ja Fononikiderakenteiden Valmistukseen
Jyväskylä: University of Jyväskylä, 2021, 83 s. (+artikkelit)
(JYU Dissertations
ISSN 2489-9003; 395)
ISBN 978-951-39-8696-4 (PDF)

Fononikiteet (PnC) ovat jaksollisia rakenteita, jotka ovat analogisia tunnetumpien fotonikiteiden kanssa. Jaksollisen dielektrisen vakion siasta niillä on jaksollinen elastisuus ja tiheys, ja siksi ne muuttavat värähtelyenergian (lämpö ja/tai ääni) liikettä materiaalin läpi. Tämä väitöskirja keskittyy kolmiulotteisten (3D) PnC rakenteiden valmistukseen, tunneliliitosten integroimiseen niiden kanssa ja niiden lämpöominaisuuksien tutkimiseen.

3D PnC rakenteet, jotka tässä tapauksessa ovat palloista koostuvia 3D neliöhiloja, valmistettiin 3D litografian avulla käyttäen vakiintuneita menetelmiä. Halutun geometrian saavuttaminen vaati kuitenkin paljon työtä ja siksi osa väitöskirjasta keskittyy rakenteen mallin optimointiin. Sitten meidän täytyi kehittää menetelmä, jolla voidaan valmistaa tarvittavat mittauslaitteet näiden 3D rakenteiden päälle, koska tälläaiseen valmistukseen ei oikeastaan ole tavanomaista menetelmää.

Seuraavaksi halusimme todistaa, että kehitetyllä mentelmällä on mahdollista valmistaa tarvittavat mittauslaitteet. Tässä tapauksessa laitteet ovat suprajohde-eriste-normaali metalli-eriste-suprajohde (SINIS) liitospareja. Me näytämme matalan lämpötilan mittauksilla, että menetelmällä voidaan valmistaa laadukkaita SINIS liitoksia sekä tasaiselle substraatille että 3D rakenteen päälle.

Väitöskirjan viimeinen osio keskittyy valmistettujen PnC rakenteiden lämmönjohtavuuden mittauksiin. Nämä mittaukset tehtiin kahdenlaisille PnC rakenteille, joissa pallojen halkaisijat olivat 3.1 μm ja 5.0 μm, sekä resistimateriaalista tehdylle kontrollirakenteelle, jonka geometria on sama. Mittausten tuloksia verrataan ballistisella mallilla tehtyihin elementtimenetelmäsimulaatioihin.

Avainsanat: Fononikide, 3D litografia, lämmönjohtavuus, matala lämpötila

PREFACE

With this thesis my nine year journey in the University of Jyväskylä is coming to an end. On the one hand it is relieving that it is finally over but on the other hand I know I will miss my colleagues and the working atmosphere here. The last two years of my PhD project were undoubtedly the roughest years of my life, as it seemed that it was almost impossible to get this project done in time. The project has been plagued with equipment break downs and in the end, when everything began to work out, the whole COVID situation started. The lock-downs of the university made the already busy schedule even worse. However, in the end I can be even prouder of myself for being able to overcome all these problems.

Now I am eager to start the next chapter of my life by working outside the university setting. I feel extremely lucky that I was able to find a job here in Jyväskylä as I have really grown to like this city. I also have to thank Ilari Maasilta for pushing me to start looking for a job early enough. I am sure that my studies have prepared me well for the various tasks to come. Especially my time in the group of Ilari Maasilta has given me a wide range of skills as a large part of the work involved fixing and building measurement setups. In the end I am happy that I chose this career path.

ACKNOWLEDGEMENTS

The work presented in this thesis has been carried out between 2017 an 2021 at the Department of Physics and Nanoscience Center at the University of Jyväskylä. Here, in the beginning of this thesis, I want to acknowledge all the people who have helped me during this project and made my graduation possible.

First, I would like to thank my supervisor Professor Ilari Maasilta for giving me the opportunity to do research in his group all the way from my second year in the university. His guidance helped me to become an independent researcher and his support allowed me to get a good position to continue my career.

From our research group I would especially like to thank Zhuoran Geng who basically thought me everything about all the laboratory and cleanroom equipment. He has been a vital support all the way from my first traineeship. The numerous discussions we had about my project were the main way to find new perspectives and solutions. Special thanks go also to Tuomas Puurtinen for doing all the elasticity simulations for my project. I also would like to thank my other fellow group members Teemu Loippo, Ari Helenius, Ilmo Räisänen, Tatu Korkiamäki, Miika Leppänen and Aki Ruhtinas for helping me with various issues and for enjoyable and enlightening discussions.

I would like to thank our laboratory engineers Kimmo Kinnunen and Tarmo Suppula for keeping the vital research equipment in order and also for giving helpful tips on different nanofabrication processes. Thanks go also to all other colleagues for providing a friendly and helpful working environment.

Special thanks go also to my family for always supporting me and encouraging me to push forward. For providing me relaxing and fun activities outside of physics I would like to thank all my friends. The value of things that can detach you from the stresses at work cannot be overstated.

I would also like to acknowledge the financial support I received from the University of Jyväskylä and the Academy of Finland.

LIST OF INCLUDED ARTICLES

PI Heiskanen, S., Geng, Z., Mastomäki, J. & Maasilta, I.J. *Nanofabrication on 2D and 3D Topography via Positive-Tone Direct-Write Laser Lithography*. Adv. Eng. Mater. **22**, 1901290 (2020).

PII Heiskanen, S. & Maasilta, I.J. *Superconducting tunnel junction fabrication on three-dimensional topography based on direct laser writing*. Applied Physics Letters **117**, 232601 (2020).

PIII Heiskanen, S., Puurtinen, T. & Maasilta, I.J. *Controlling thermal conductance using three-dimensional phononic crystals*. Submitted manuscript.

PIV Tian, Y., Isotalo, T.J., Konttinen, M.P., Li, J., Heiskanen, S., Geng, Z. & Maasilta, I.J. *Integrating metallic wiring with three-dimensional polystyrene colloidal crystals using electron-beam lithography and three-dimensional laser lithography*. J. Phys. D: Appl. Phys. **50**, 055302 (2017).

Author's contribution

The author wrote the first drafts of articles PII and PIII, and partly of article PI. The author was responsible for all the sample fabrication for articles PII and PIII. For articles PI and PIV, the author did a part of the sample fabrication. The author measured all the data in articles PII and PIII. The author did all the data analysis in article PII and a part of the analysis in articles PI and PIII.

CONTENTS

ABSTRACT
TIIVISTELMÄ (FINNISH ABSTRACT)
PREFACE
ACKNOWLEDGEMENTS
LIST OF INCLUDED ARTICLES
CONTENTS

1 INTRODUCTION 13

2 BACKGROUND 15
2.1 Heat transfer 15
2.2 Thermal properties 16
2.2.1 Phonons 16
2.2.2 Heat capacity 18
2.2.3 Thermal conduction in PnCs 18
2.2.4 Linear elasticity simulations 19
2.3 NIS junction devices 21
2.3.1 Superconductivity 21
2.3.2 NIS junction 22
2.3.3 NIS thermometry 25
2.4 Previous phononic crystal studies by our group 25
2.4.1 2D phononic crystals 25
2.4.2 3D phononic crystals 29

3 FABRICATION METHODS 32
3.1 Two-photon lithography 32
3.1.1 3D-lithography 34
3.2 Reactive ion etching 34
3.3 Physical vapor deposition 36

4 EXPERIMENTAL METHODS AND FABRICATION RESULTS 39
4.1 Development of the 2.5D fabrication method for devices on large topographies 39
4.2 Fabrication of the phononic crystal structure 41
4.2.1 Creating the 3D design for the structure 41
4.2.2 The fabrication procedure 43
4.2.3 Optimizing the PnC structures 43
4.3 Fabrication of the SINIS junctions 49

5 MEASUREMENT SETUP 54
5.1 Measurement procedure 54

6 MEASUREMENT RESULTS 57

6.1 NIS junctions on a substrate 57
6.2 What causes the double gap feature? 60
6.3 SINIS junctions on a 3D structure 66
6.4 Thermal conductance of the PnC structures 69

7 CONCLUSIONS 74

BIBLIOGRAPHY... 76

INCLUDED ARTICLES

1 INTRODUCTION

Phononic crystals (PnCs) are periodic structures analogous to photonic crystals, which instead of a periodic dielectric constant have a periodic density and elasticity. PnC structures can introduce changes to the phononic band structure of the material and can even lead to complete band gaps at certain frequencies caused by Bragg interference [1, 2] and local mechanical resonances [3, 4]. Limitations in fabrication methods forced early experimental studies to focus on macroscopic structures with periods in the millimeter-scale [5]. The dominant frequency in such systems is in the range of sonic or ultrasonic waves (MHz frequencies), and thus typical applications for such structures include acoustic filtering, focusing or wave-guiding [3, 5, 6]. More advanced fabrication methods like interference lithography and colloidal crystallization allowed the fabrication of micro- and nano-scale periodic structures whose dominant frequency is in the hypersonic range (GHz frequencies) [7, 8]. One example of applications for such structures is in the RF communication technology [9]. Because of the difficulties in the fabrication of nano-scale 3D PnC samples, even some recent experimental wave transmission studies have been done for macroscopic structures [10]. However, there is less work focusing on thermal properties of micro- and nano-scale PnC structures (for reviews, see [4, 11]), especially at low temperatures, where experimental studies have been done on 2D PnC structures fabricated into a thin SiN film [12, 13]. Before this thesis there have been no such low temperature studies for 3D crystal structures and we know of only one study at higher temperatures [14].

Controlling thermal transport at low temperatures is crucial for several applications, for example in ultrasensitive radiation detection [15] limiting thermal transport is necessary. Similarly the control of thermal transport could be used for quantum bits, where people are already planning to use PnC structures [16]. Previously thermal transport has been suppressed by phonon mean free path shortening employing scattering centers such as impurities and nanoparticles [17–19]. It has been shown, however, that such control of the thermal transport can also be achieved with periodic PnC structures [20–22]. As was theoretically and experimentally demonstrated by our group in Reference [12], PnC structures change the thermal conductance of the material at low temperatures by coherently modify-

ing its phononic band structure. This demonstration was done with two dimensional crystals. The same idea can be applied also for three dimensional crystals as is shown in this thesis. For applications, the benefit of three dimensional PnC structures is that they allow the isolation of any kind of devices instead of just devices on suspended membranes as is the case with two dimensional crystals.

It has been shown that 3D PnCs can be fabricated via self-assembly using colloidal crystallization of mono-disperse spherical particles [8, 23–25]. However, it is difficult to integrate any measurement devices with these crystals. Our group developed a method to harden the spheres with an electron beam exposure using an SEM to allow fabrication of metallic wires onto the crystals [**PIV**], but there are still issues with making continuous wiring due to the cracking of the crystals and separation from the substrate at the edges of the crystals. In this thesis, we use 3D laser lithography to fabricate the crystals and develop a new method for general device fabrication on large topographies using the same 3D lithography and lift-off. The 3D lithography is based on two-photon absorption and it allows the fabrication of almost any kind of 3D structure with a resolution limit of around 200 nm. These properties make 3D lithography a very versatile method, which means that integration of devices is also easier. However, this method cannot reach as small periodicities as colloidal crystallization. The same 3D lithography was chosen to be the basis for the heater and thermometer device fabrication as well due to its inherent 3D capabilities. However, to use this method a new fabrication process with completely different resists had to be developed, as the resists typically used in 3D lithography are negative-tone liquid phase resists, whereas positive-tone solid phase resists are needed for the device fabrication. The devices needed in our case are normal metal-insulator-superconductor (NIS) tunnel junctions, serving as local thermometers at low temperatures. We show that the developed method can produce good quality NIS devices.

The PnC structures studied in this thesis are 3D simple cubic lattices consisting of spheres. This crystal type was chosen for simplicity. Two different PnC structures with sphere diameters of 3.1 μm and 5.0 μm were studied together with a control bulk structure. The bulk structures had the same shape and volume but the volume was filled with bulk resist instead of a lattice of spheres. The thermal conductance of these structures was measured using two pairs of NIS junctions or SINIS junctions fabricated on top of them. The results of these measurements are compared with finite element method (FEM) simulations. The results demonstrate that the fabricated 3D PnCs can be used for controlling thermal transport. The crystal size and the filling factor of both PnC structures were the same, which means that classically they should have the same thermal conductance. However, in these measurements there is a large difference between them. Surprisingly, the fabricated PnC structures, contrary to our expectations, enhanced the thermal conductance compared to the bulk instead of reducing it. This is most likely caused by the chosen geometry, but is not fully clear yet. This behaviour could possibly be explained by going back to simpler geometries or by making samples where the interface effects between a film and a PnC can be directly studied.

2 BACKGROUND

2.1 Heat transfer

Heat can be transferred through three different mechanisms: convection, radiation and conduction. Convection means the transfer of heat due to the bulk movement of molecules within liquids and gasses. Heat transfer through radiation is usually described with the Stefan-Boltzmann Law. The law gives the power radiatied from a body in terms of its temperature:

$$P = A\epsilon(\lambda)\sigma T^4 \tag{1}$$

where T is the temperature, A is the surface area, $\epsilon(\lambda)$ is the emissivity ($\epsilon(\lambda) \leq 1$) which is 1 for a black body, and σ is the Stefan-Boltzmann constant. The constant is given by $\sigma = \pi^2 k_B^4/(60c^2\hbar^3)$, where k_B is the Boltzmann constant, c is the speed of light in vacuum, and $\hbar$ is the reduced Planck constant.[26]

The important mechanism for this study is conduction, which is the dominant one in solids at low temperatures. Thermal conduction is usually described with the Fourier's law:

$$\boldsymbol{J_u} = -\kappa \nabla T, \tag{2}$$

which describes describes the energy flux density $\boldsymbol{J_u}$ in terms of the thermal conductivity κ and the temperature gradient ∇T. In this thesis it is assumed that there is a net transport of energy, but not of electrons [26], i.e. we only consider phononic heat transport.

At low temperatures the Fourier's law can break down. This can happen when the scattering processes (phonon-phonon and phonon-impurity) which determine the thermal conductivity die out. In other words, the scattering length becomes longer than the sample size and the heat conduction becomes ballistic. At this point in 3D solids the emitted power actually starts to follow a law similar to Equation 1 with the Stefan-Boltzmann constant altered to a phononic Stefan-Boltzmann factor [27].

2.2 Thermal properties

2.2.1 Phonons

Phonons are the quantization of lattice vibrations in solids analogous to photons, which are the quanta of electromagnetic waves. By using the properties of phonons we can find the different thermal properties of insulators and semiconductors. We just need an expression for the internal energy $U(T)$ and from that we can derive thermal properties such as heat capacity. To get to the internal energy we need to describe the distribution of phonons.

We start by calculating the thermal average number of phonons in a mode. Assuming that the phonons are in equilibrium with a bath at temperature T we can use the Boltzmann distribution $P_n \propto e^{-E_n/k_BT}$. We know that the energy of a state E_n with n quanta in the mode is

$$E_n = \left(n + \frac{1}{2}\right)\hbar\omega, \tag{3}$$

where ω is the angular frequency and $(1/2)\hbar\omega$ is the quantum mechanical zero-point energy of the mode [26]. Using this we can write the partition function Z for the system, which is the sum over all the states:

$$Z = \sum_{n=0}^{\infty} e^{-\left(n+\frac{1}{2}\right)\hbar\omega/k_BT}. \tag{4}$$

This is a sum of the form $\sum x^n$, with $x \equiv \exp(-\hbar\omega/k_BT)$. Because we know that x is smaller than one, the infinite sum has a known value $1/(1-x)$, thus we can write

$$Z = \frac{e^{-\hbar\omega/2k_BT}}{1 - e^{-\hbar\omega/k_BT}}. \tag{5}$$

Since the Boltzmann distribution is used, the probability of the the system being in state n is given by the Boltzmann factor:

$$P_n = \frac{e^{-\left(n+\frac{1}{2}\right)\hbar\omega/k_BT}}{Z} \text{ [26]}. \tag{6}$$

Knowing this we can derive the thermal average value of n. It is simply given by the sum

$$\langle n \rangle = \sum_{n=0}^{\infty} nP_n = \sum \frac{ne^{-n\hbar\omega/k_BT}}{1 - e^{-\hbar\omega/k_BT}}. \tag{7}$$

With $y \equiv \hbar\omega/k_BT$, the summation is of the from:

$$\sum ne^{-ny} = -\frac{d}{dy}\sum e^{-ny} = -\frac{d}{dy}\left(\frac{1}{1-e^{-y}}\right) = \frac{e^{-y}}{(1-e^{-y})^2}. \tag{8}$$

Using this and Equation 7 we get

$$\langle n \rangle = \frac{e^{-y}}{1 - e^{-y}}. \tag{9}$$

Changing the form a little bit, we get the familiar Bose-Einstein distribution:

$$\langle n \rangle = \frac{1}{e^{\hbar\omega / k_B T} - 1}. \tag{10}$$

Using the above equation we now can write an expression for the internal energy:

$$U(T) = \sum_{\mathbf{k},j} \left(\langle n_{\mathbf{k},j} \rangle + \frac{1}{2} \right) \hbar\omega_j(\mathbf{k}) = \sum_{\mathbf{k},j} \frac{\hbar\omega_j(\mathbf{k})}{e^{\hbar\omega_j / k_B T} - 1} + \sum_{\mathbf{k},j} \frac{1}{2} \hbar\omega_j(\mathbf{k}), \tag{11}$$

where the summation is done over all wave vectors $\mathbf{k}$ and phonon modes j, which have dispersion relations described by $\omega_j = \omega_j(\mathbf{k})$. The dispersion relations can be determined for different structures by simulations. For our PnC structures we have used FEM simulations based on continuum linear elasticity theory to calculate the phonon band structure, examples of which for some lattice types are shown in Figure 1.

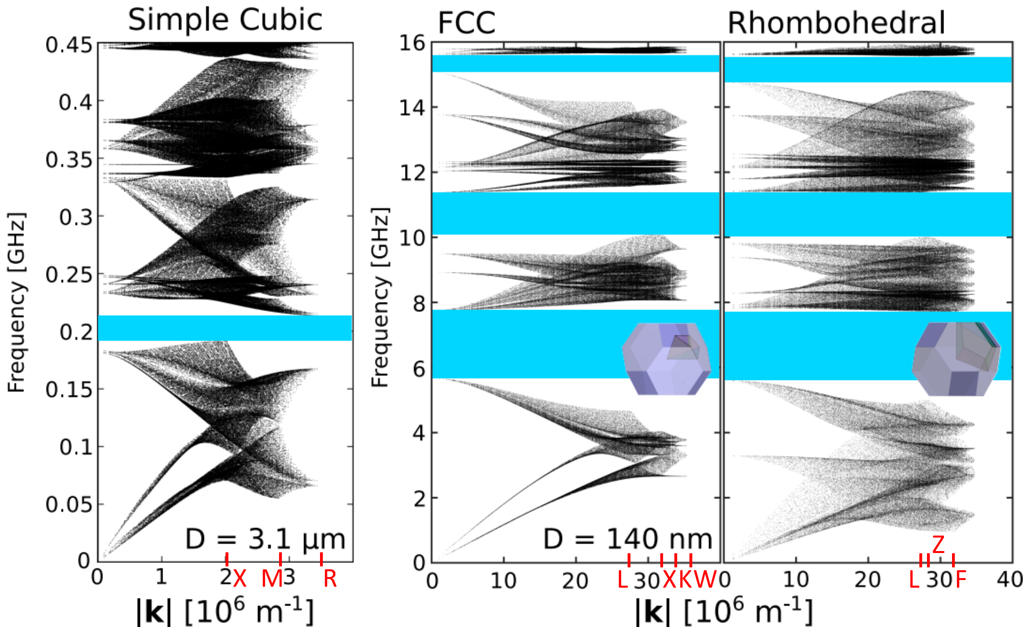

FIGURE 1 The lowest spectral branches obtained from the FEM simulations for different lattice types. The simple cubic simulation was done for the 3.1 µm spheres and the other ones for smaller 140 nm spheres used in the colloidal crystallization. The material for the 3.1 µm PnC is IP-Dip resist by Nanoscribe GmbH and polystyrene for the 140 nm PnCs. The contact area between spheres was 0.95 µm^2 for the 3.1 µm spheres and 219 nm^2 for the 140 nm spheres. Energy gaps are shown in blue and high symmetry points are marked in red.

2.2.2 Heat capacity

The low temperature phononic heat capacity $C(T)$ of an insulator can be calculated by differentiating the internal energy of the crystal $U(T)$ with respect to temperature:

$$C(T) = \frac{\partial U(T)}{\partial T} = \frac{\partial}{\partial T} \sum_{\mathbf{k},j} \frac{\hbar\omega_j(\mathbf{k})}{e^{\hbar\omega_j/k_B T} - 1}. \tag{12}$$

When we change the summation to integration over the K-space, divide by the volume and then go through the temperature differentiation, we get the volume-specific heat capacity as

$$C_V(T) = \frac{\hbar^2}{32\pi^3 k_B T^2} \sum_j \int_K d\mathbf{k} \frac{\omega_j^2(\mathbf{k})}{\sinh^2(\hbar\omega_j/2k_B T)} \tag{13}$$

with the units $\mathrm{J}/(\mathrm{K} \times \mathrm{m}^3)$.[28]

We can derive the Debye T^3 law from the above equation by carrying out the integration only over the two transverse and one longitudinal bulk acoustic phonon modes, which have velocities c_t and c_l. This is called the Debye approximation. By assuming isotropy and changing the variable to $x = \hbar c_j k/2k_B T$, one gets

$$C_D = \frac{4\pi^3}{15} \frac{k_B^4}{\hbar^3} \left(\frac{2}{c_t^3} + \frac{1}{c_l^3} \right) T^3 \tag{14}$$

which can be simplified with the Debye temperature Θ_D into

$$C_D = \frac{12\pi^4}{5} \left(\frac{T}{\Theta_D} \right)^3. \tag{15}$$

Θ_D is the temperature corresponding to a crystal's highest normal mode of vibration.

2.2.3 Thermal conduction in PnCs

The simplest sample geometry for the thermal conductance measurements has a 3D sphere array with a rectangular heater on top of it (Figure 2). In such a geometry the thermal conduction of the PnC can be calculated from the phonon emission of the heater element. The net phonon heat flow travels outwards into the 3D crystal in all directions, emitted by the heater. At the low temperatures (<1 K) used for the measurements this heat flow is typically ballistic as shown in References [12, 29], meaning that the phonon emission is radiative rather than diffusive. Only the phonon modes propagating outward with energies $\hbar\omega_j(\mathbf{k})$ carry the energy, so the phonon emission can be written as

$$P(T) = \frac{1}{8\pi^3} \sum_j \int_\gamma d\gamma \int_K d\mathbf{k} \hbar\omega_j(\mathbf{k}) n(\omega_j, T) \frac{\partial \omega_j(\mathbf{k})}{\partial \mathbf{k}} \cdot \hat{\mathbf{n}}_\gamma \Theta \left(\frac{\partial \omega_j}{\partial \mathbf{k}} \cdot \hat{\mathbf{n}}_\gamma \right), \tag{16}$$

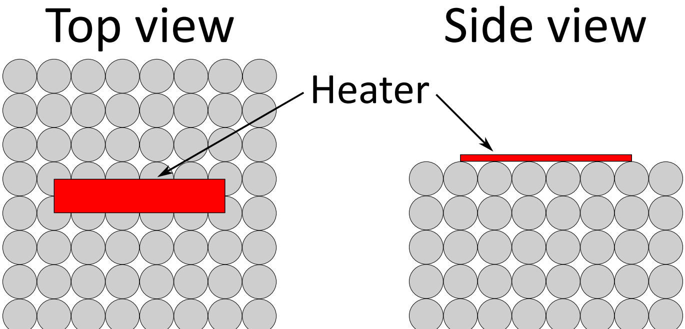

FIGURE 2 A schematic of the simplest sample geometry. The heat sink is below the lattice of spheres.

where γ is a planar rectangular heater element with length l and width d [30]. Here $\hat{\mathbf{n}}_\gamma$ is the unit normal on the rectangular heater and Θ is the Heaviside step function. The term $n(\omega, T)$ is the Bose-Einstein distribution. As shown in Equation 10 it describes the thermal occupation of the phonons. The last term $\partial\omega_j/\partial\mathbf{k}$ describes the group velocity of the modes j [30]. So again similarly to Equation 11, the only unknown is the set of dispersion relations $\omega_j = \omega_j(\mathbf{k})$, which can be numerically calculated. In this study we used the finite element method to find these relations.

Knowing the radiative phonon emission power P, the thermal conductance can be easily calculated. The definition of thermal conductance is $G \equiv \Delta P/\Delta T$, where ΔT is the temperature difference between the environment and the object. If ΔT is small, the definition becomes $G = \partial P/\partial T$ [31]. This means that G has a dependence $G \propto 1/c^2$, as can be seen from the Stefan-Boltzmann law (Equation 1). Using this definition we can simply write the thermal conductance as

$$G_\gamma = \frac{\partial}{\partial T} P(T). \tag{17}$$

In Figure 3 we show examples of theoretical heat capacity and thermal conductance curves for different sphere PnC structures and the bulk material used for their fabrication. The curves for the PnC structures were calculated using linear elasticity simulations explained in the following chapter. From Figure 3 we see that large reduction of thermal conductance is expected due to the PnC.

2.2.4 Linear elasticity simulations

As stated earlier the phonon band structure of the phononic crystals can be numerically calculated. We used the finite element method (FEM) to solve the 3D elasticity equations for the studied structures. This methods starts with the definition of a FEM mesh. The FEM mesh of the unit cell for one of the studied PnCs is shown in Figure 4. When solving the band structure three types of equations are needed. The first is the equation of motion (Newton's second law) which is

$$\nabla \cdot \sigma = \rho \ddot{\mathbf{u}} = -\rho\omega^2 \mathbf{u}, \tag{18}$$

where ρ is the density of the material and $\mathbf{u}$ is the displacement vector [32]. Here

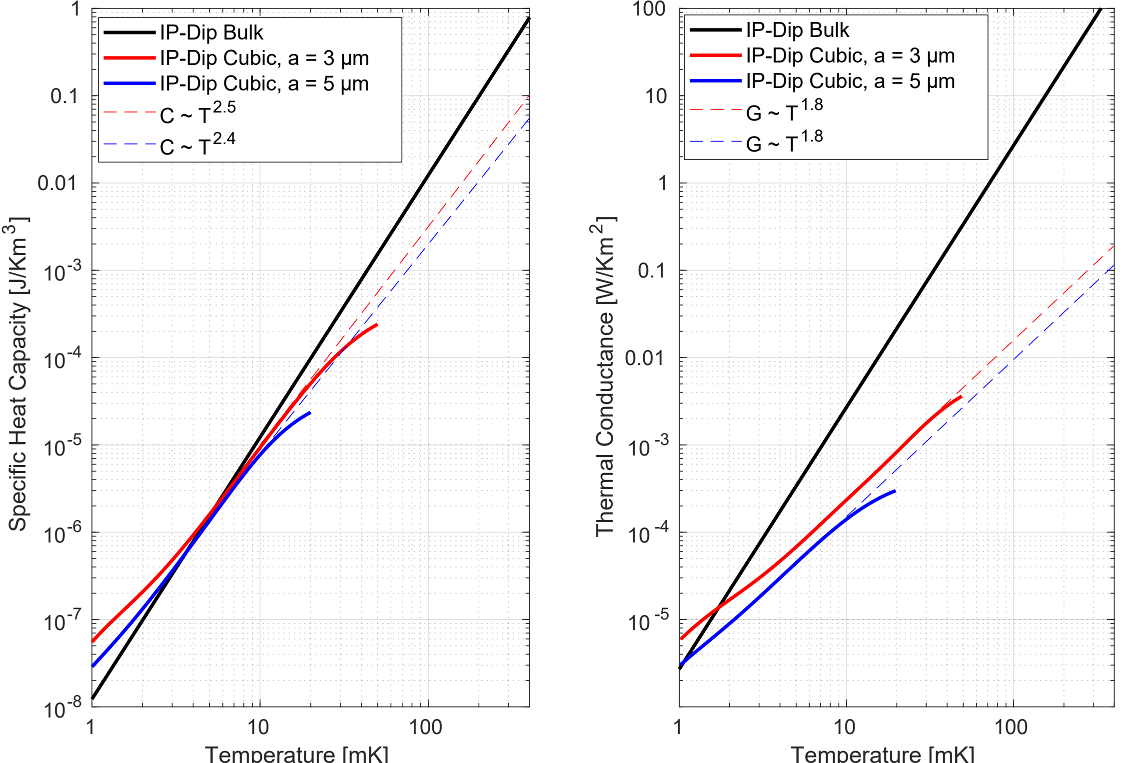

FIGURE 3 Theoretical heat capacity and thermal conductance of cubic PnC structures and the bulk material used for their fabrication as a function of temperature.

σ is the Cauchy stress tensor, which is given by the generalized Hooke's law. Hooke's law is the constitutive equation for elastic materials and in tensor form it can be written as

$$\sigma = \mathbf{C} : \varepsilon, \tag{19}$$

where $\mathbf{C}$ is the fourth-order stiffness tensor and ε is the infinitesimal strain tensor [32]. The strain tensor can be calculated using a strain-displacement equation:

$$\varepsilon = \frac{1}{2}\left[\nabla \mathbf{u} + (\nabla \mathbf{u})^{\mathrm{T}}\right] \text{ [32].} \tag{20}$$

When dealing with a homogeneous and isotropic material, Equation 18 can be written in the form

$$\mu \nabla^2 \mathbf{u} + (\mu + \lambda)\nabla(\nabla \cdot \mathbf{u}) = -\rho\omega^2 \mathbf{u}, \tag{21}$$

which is called the Lamé-Navier or the Navier-Cauchy equation [32]. The Lamé parameters λ and μ are related to the material parameters Poisson's ratio ν and Young's modulus E, by the relations $\mu = E/[2(1+\nu)]$ and $\lambda = E\nu/[(1+\nu)(1-2\nu)]$ [32]. The values used for the IP-Dip resist are shown in Table 1. To solve the eigenvalue problems we used Bloch's theorem conditions for the boundaries $B^{\pm}$ between spheres:

$$\mathbf{u}_{B^+} = \mathbf{u}_{B^-} e^{-i\mathbf{k}(\mathbf{r}_{B^+} - \mathbf{r}_{B^-})}, \tag{22}$$

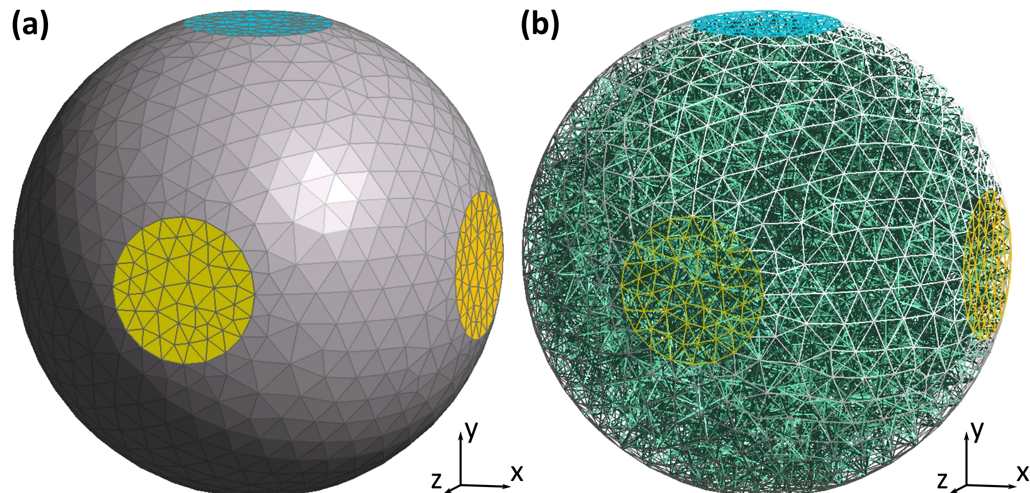

FIGURE 4 The mesh used for the elasticity simulations of the 5.0 µm PnC structure. (a) The surface of the unit cell for clarity. (b) The whole mesh for the unit cell. Yellow regions form the contacts between neighboring spheres. The sizes of the contact areas were determined by scanning electron microscopy of the fabricated samples.

where $\mathbf{k}$ is the wave vector. The boundaries $B^{\pm}$ are also the boundaries of the unit cell of the 3D lattice. Since we are using Bloch's theorem, we know that there are plane wave-type solutions $\mathbf{u}_j(x,\ y,\ z;\ \mathbf{k})$ which have eigenfrequencies $\omega_j(\mathbf{k})$. These eigenfrequencies then give us the dispersion relations (Figure 1) needed to calculate the thermal properties of the PnC structure.

TABLE 1 The material parameters used for the IP-Dip resist [33].

Parameter	Value
Density ρ	1100 kg/m^3
Young's modulus E	2.5 GPa
Poisson's ratio ν	0.49

2.3 NIS junction devices

2.3.1 Superconductivity

Superconductivity is a physical phenomenon where the resistance of a material goes to zero below it's critical temperature T_C. This happens only for certain materials, which are called superconductors. This phenomenon was first discovered by H. K. Onnes in 1911 [34], by cooling mercury in liquid helium. In addition to perfect conductivity superconductors also exhibit perfect diamagnetism. This phenomenon, called Meissner effect, was discovered by W. Meissner and R. Ochsenfeld in 1933 [35], by studying the distribution of magnetic field outside superconducting tin and lead samples.

In 1957 J. Bardeen, L. N. Cooper and J. R. Schrieffer presented a microscopic theory, which explained the origin of superconductivity [36]. This theory is called the BCS theory after their names. According to the theory, the superconducting ground state consists of Cooper pairs which are formed by electron-phonon interaction. A Cooper pair is a pair of electrons, which are attracted to each other due to the motion of the ion cores around them. The first electron attracts the ion cores, and thus polarizes the medium, which leads to the second electron being attracted by these extra ion cores.

One very interesting prediction of the BCS theory is that for a single particle excitation there is an energy gap (Δ) between the BCS ground state and the first excited state. What this means is that an energy of 2Δ is required to break a Cooper pair and excite the two quasi-particles. The size of the energy gap at 0 K is related to the critical temperature of the material according to

$$2\Delta(0) = 3.528 k_B T_C. \tag{23}$$

The theory also predicts that the energy gap is dependent on temperature. When temperature goes from T_C to 0 K the gap goes from 0 to $\Delta(0)$. Close to T_C, the relation between $\Delta(0)$ and $\Delta(T)$ is approximately

$$\frac{\Delta(T)}{\Delta(0)} \approx 1.74 \left(1 - \frac{T}{T_C}\right)^{1/2}. \tag{24}$$

This kind of relation to the square root of ($T_C - T$) is characteristic for all mean field theories.[36, 37]

2.3.2 NIS junction

The energy gap of superconductors can be used for a variety of applications. One interesting application is the NIS junction. Such junctions are used for heating and thermometry in this study. The NIS junction is simply a device where there is a normal metal and a superconductor separated by an insulating layer. The insulating layer works as a tunneling barrier. Electrons can tunnel through the insulator only if it is very thin (few nanometers), since the tunneling probability drops exponentially with the thickness [37, 38]. This kind of device was studied first by Fisher and Giaever, who used $Al/Al_2O_3/Pb$ devices with Pb being the superconductor and Al the normal metal [39].

These kinds of devices are more generally called tunnel junctions. The electrodes separated by the insulator can be superconductors or normal metals. Therefore, the NIS junction is one of three types, the others being the normal metal-insulator-normal metal (NIN) junction and the superconductor-insulator-superconductor (SIS) junction [37, 38]. In an NIS junction an electron can tunnel through the barrier only when its energy is higher than the energy gap of the superconductor. Therefore, the tunneling current depends on the bias voltage V and the temperature of the normal metal T_N, as is schematically described in Figure 5. The dependence is highly non-linear and thus the NIS junction can be used

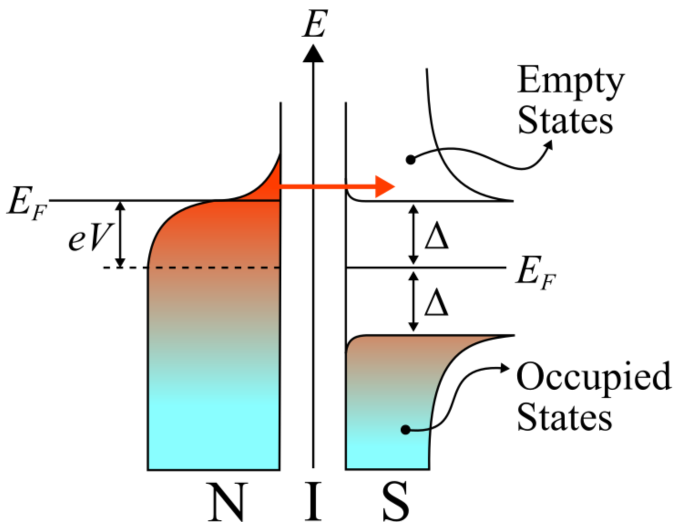

FIGURE 5 The energy graph of an NIS junction. E_F is the Fermi energy and the arrow represents electrons tunneling through the insulator.

as a thermometer in the sub-Kelvin range [40–42]. In some cases NIS junctions may be considered to be primary electron thermometers [43].

Because NIS junctions can be fabricated in scales below one micron and they are very sensitive, they can be used as local sensors for example in heat transfer measurements [12, 13, 44, 45]. By using a microwave readout it is possible to operate NIS junctions fast in microsecond time scales [46, 47]. It might also be possible to use them as the sensors in bolometrically operated radiation detectors [48–51]. Usually the superconducting material in the NIS junction is aluminum, as in this study, which limits the working range of the devices to below 1 K temperatures. However, by choosing superconductors with higher transition temperatures, the working range of NIS junction thermometers can be increased. Different choices include for example Nb [52, 53], NbN [54], TiN [55], TiN_2 [56] and TaN [57]. NIS junctions also have many other applications, such as metrology [58, 59], electronic cooling [60, 61] and thermal rectification [62]. NIS junction cooling has been demonstrated on different geometries like macroscopic and mesoscopic platforms [63–65] and nanoscale beams [42, 66]. Cooling has also been demonstrated on various devices, such as radiation detectors [67], remote devices via photons [68, 69] and components of quantum information devices [70].

To calculate the current through an NIS junction we first need the density of states. The density of states of the superconductor $\mathcal{N}_S(E)$ can be obtained from

$$\mathcal{N}_S(E)dE = \mathcal{N}_N(\xi)d\xi, \tag{25}$$

because the quasi particle excitations (energy E) have creation operators which are in one-to-one correspondence with the operators for the normal metal (energy ξ) [37]. We are mostly interested in energies close to the Fermi energy, and thus we can equate $\mathcal{N}_N(\xi) = \mathcal{N}(0)$, where $\mathcal{N}(0)$ is the normal state density of states at the Fermi energy. With this we arrive at the result

$$N_S(E) = \frac{\mathcal{N}_S(E)}{\mathcal{N}(0)} = \frac{d\xi}{dE} = \frac{|E|}{\sqrt{E^2 - \Delta^2}}, \text{ if } |E| > \Delta$$
$$= 0, \text{ if } |E| < \Delta \text{ [37]}. \quad (26)$$

Considering only the first order, single particle tunneling theory and disregarding higher order processes we can now write an expression for the current:

$$I_{NIS} = \frac{1}{eR_i} \int_{-\infty}^{\infty} d\epsilon N_S(\epsilon)[f_S(\epsilon) - f_N(\epsilon + eV)], \quad (27)$$

where ϵ is the energy, R_i is the tunneling resistance of junction i, and $N_S(\epsilon)$ is the normalized superconducting density of states. This is the standard result for a voltage biased NIS junction. The tunneling resistance can be written as

$$R_i = \frac{\hbar}{4\pi^2 e^2 A |t_o|^2 \mathcal{N}(0) \mathcal{N}_S(0)}, \quad (28)$$

where A is the area of the junction, $|t_o|^2$ is the tunneling probability, and $\mathcal{N}_S(0)$ is the superconducting density of states at the Fermi energy.[37, 41, 71]

To take into account nonidealities in the junction, the expression for the superconducting density of states needs to be altered from the normal BCS expression. We can use the expression intoduced by Dynes et al. [72], which is

$$N_S(\epsilon, T_S) = \left| \text{Re}\left(\frac{\epsilon + i\Gamma}{\sqrt{(\epsilon + i\Gamma)^2 - \Delta^2(T_S)}} \right) \right|, \quad (29)$$

where Γ is the so called Dynes parameter, which describes the broadening of the density of states. This parameter is set-up dependent in the case of photon-assisted tunneling [40]. The $\Delta(T_S)$ here, is the superconducting energy gap, with temperature dependence. This form for the density of states is particularly appropriate for Al junctions, in which it has been shown that the broadening is caused by environmentally assisted tunneling events [73].

For practical applications usually two junctions (NIS and SIN) are fabricated in series forming a SINIS junction. For example, when used as a thermometer this increases the signal response by a factor of two. Let's assume that the two junctions are symmetrical, meaning that the tunneling resistance R_i is the same for both junctions. This leads to the voltage drop V being the same for both junctions. Therefore, we can write the current for the SIN junction as

$$I_{SIN} = \frac{1}{eR_i} \int_{-\infty}^{\infty} d\epsilon N_S(\epsilon)[f_N(\epsilon - eV) - f_S(\epsilon)]. \quad (30)$$

The current for both junctions must of course be the same since they are in series. We can also write the current for the SINIS junction in a symmetric form, where there is no more dependence on f_S:

$$I_{SINIS} = \frac{1}{2eR_i} \int_{-\infty}^{\infty} d\epsilon N_S(\epsilon)[f_N(\epsilon - eV) - f_N(\epsilon + eV)] \text{ [74]}. \quad (31)$$

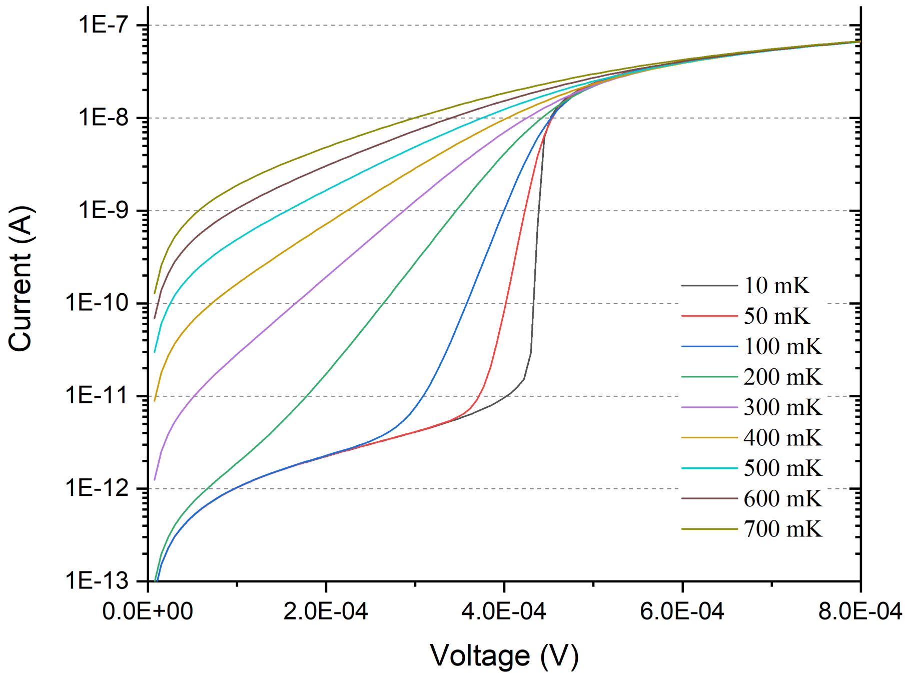

FIGURE 6 Simulated I-V curves for a SINIS junction pair with Al as the superconductor, to illustrate how the junctions can be used for thermometry.

2.3.3 NIS thermometry

At temperatures below the T_C, the I-V curve of an NIS juction is highly nonlinear for voltages smaller than the energy gap of the superconductor. This nonlinearity is also highly dependent on temperature, as is shown in Figure 6 for a SINIS junction. We can use this characteristic for thermometry by biasing the junction with a current that matches the nonlinear part and then measuring the voltage. However, this is only a secondary thermometer so it has to be calibrated for the selected bias current. Normally two different current biases are used, because with a smaller current the sensitivity is better at lower temperatures, and with a higher current the sensitivity is better at higher temperatures. In the case of Figure 6 the low bias current should be around 3×10^{-11}A and the high bias around 4×10^{-10}A.

2.4 Previous phononic crystal studies by our group

2.4.1 2D phononic crystals

Our group demonstrated both theoretically and experimentally in 2014 that phonon thermal conductance can be controlled at low temperatures by using nanoscale periodic structures [12]. These periodic structures alter the phonon band structure of the material and are thus called phononic crystals (PnC). These first studies were done with 2D crystals which were thin films periodically perforated

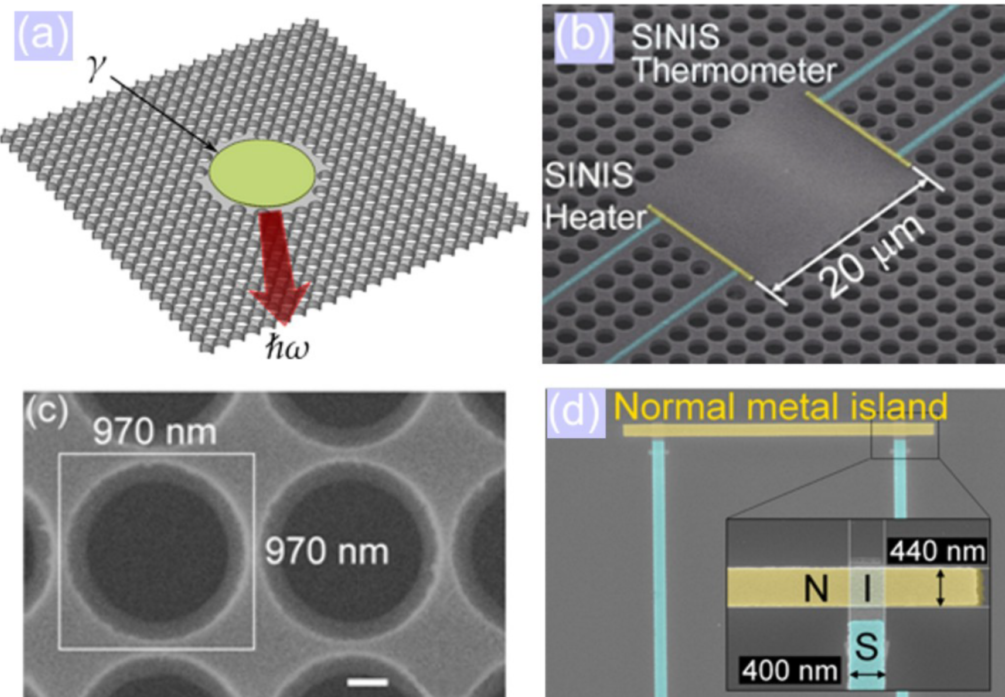

FIGURE 7 The 2D PnC structure fabricated by etching holes into a SiN membrane. (a) A schematic representation of the perforated hole lattice which was patterned by e-beam lithography. The central region is not perforated to leave room for a heater and a thermometer. (b) A false colour SEM image of the heater and the thermometer on the sample with the period of a = 2425 nm. The areas colored in yellow (Cu) and blue (Al) are the metallic lines for the SINIS junctions on the membrane. (c) An SEM image of the the perforations on the sample with the shorter period, showing the size of the unit cell (970 nm x 970 nm). The length of the scale bar is 200 nm. (d) A zoomed-in scanning electron micrograph of the SINIS junction structure, which consists of aluminum (blue) and copper (yellow) wires with tunneling barriers between them. Reprinted from Reference [12], with permission of Springer Nature, copyright 2014.

by round holes. The 2D crystals were fabricated from a 485 nm thick SiN film. A square array of round holes with a filling factor of 0.7 was etched into the film (Figure 7). Two different hole sizes were chosen creating lattices with different periodicities. The first lattice had a period of 970 nm (Figure 7) which according to theoretical calculations has a band-gap at the characteristic energy of the phonons that are thermally dominant at 0.1 K. A 2425 nm period was chosen for the second lattice, because it is supposed to have no band-gap at all. Then two Al-AlO_x-Cu SINIS junctions were fabricated on the films, so that one could be used as the heater and the other could be used to measure the local phononic temperature. A small part of the film was left unperforated so that there was a platform for the SINIS junctions (Figure 7b).

The measured emitted power P is shown as a function of the temperature of the film in Figure 8. Results for both the PnC structures and a full membrane are presented together with theoretical lines. The emitted power is obviously lower for the PnC structures compared to the unperforated membrane in the whole temperature range, meaning that the thermal conductance is reduced with both lattices. The crystal with the larger period has a lower thermal conductance than the crystal with the smaller period. This initially unexpected result showed that the band-gap is not the only main cause for the suppression of the thermal conductance in the crystals. The results also show that the reduction of the thermal conductance is dependent on the temperature. It is clear that simple geometrical effects cannot be the cause for the reduction of the thermal conductance, because classically the amount of reduction is only dependent on the filling factor [75], and here both lattices had the same filling factor. Further study into the PnC structures showed that the main cause for the lower thermal conductance is the reduction in group velocity of phonons [12]. The theoretical curves in Figure 8 were calculated using the finite element method for both the PnC samples and the full membrane. The calculations were done using the elastic Lamé equations and a ballistic transport model (Equation 16) [12]. It is clear from comparing the results that the theory is in quantitative agreement with the measurements.

Later more studies were made with 2D PnC structures with even larger periods [13]. The samples were similar to the earlier studies except this time the normal metal on the SINIS junctions was a TiAu bi-layer. This time 300 nm thick SiN films were used and the chosen periods were 4 μm, 8 μm and 16 μm. The filling factor was still 0.7 as in the earlier studies. The results of these measurements are shown in Figure 9 together with theoretical curves. The theoretical curves were calculated with the same ballistic model [13]. Again the emitted phonon power is reduced in all the phononic crystal samples compared to the uncut membrane. The difference is around an order of magnitude.

What's interesting about these results is the fact that the PnC with the lowest thermal conductance is the 8-μm PnC instead of the 16-μm PnC. This means that by increasing the period, the thermal conductance can only be reduced up to a limit. The results thus show that this limit is between the 4 μm and 16 μm periods. However, this is not what is predicted by the coherent theory as shown by the theoretical curves in Figure 9. This observed nonmonotonous behaviour of the

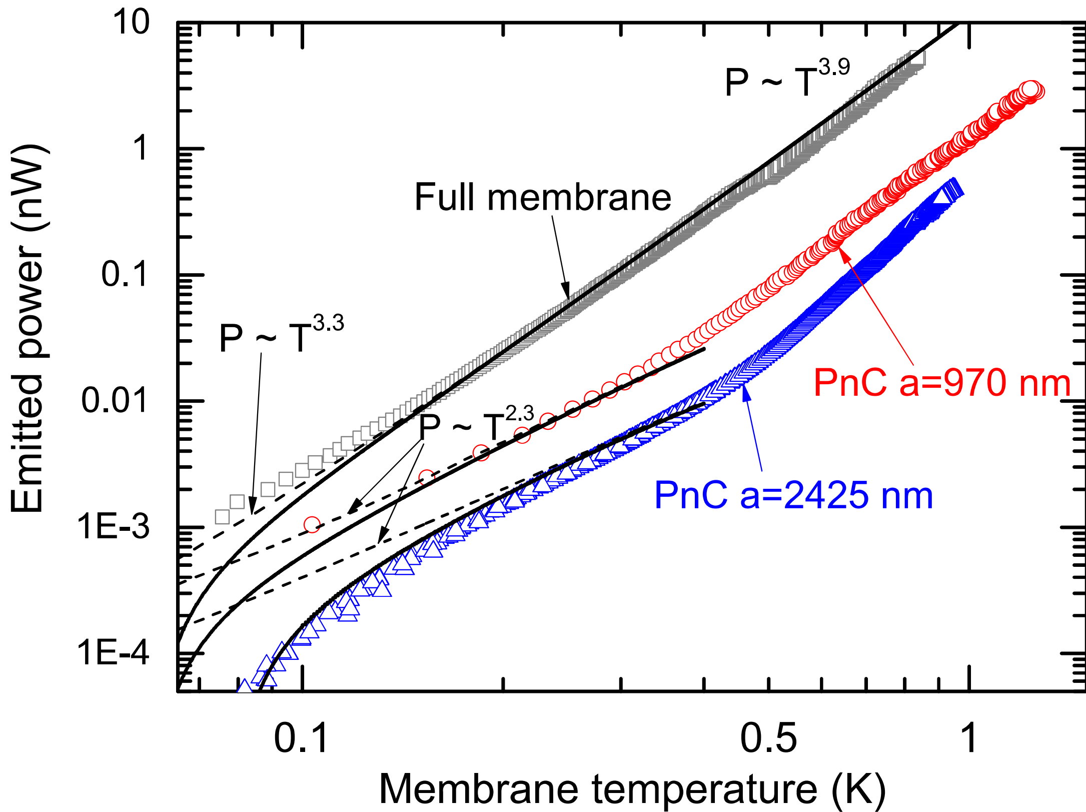

FIGURE 8 The measured emitted power of the heater as a function of the membrane temperature. The gray squares represent the measured data for the unperforated membrane. The red circles and blue triangles show the data measured for the two different PnC samples. The theoretical curves were calculated with the ballistic theory using the band structures calculated for the different cases. The solid lines were calculated with the back radiation of phonons from the substrate and the dashed line without it. All the theoretical curves were fitted to the measured data using the same single scale parameter. Reprinted from Reference [12], with permission of Springer Nature, copyright 2014.

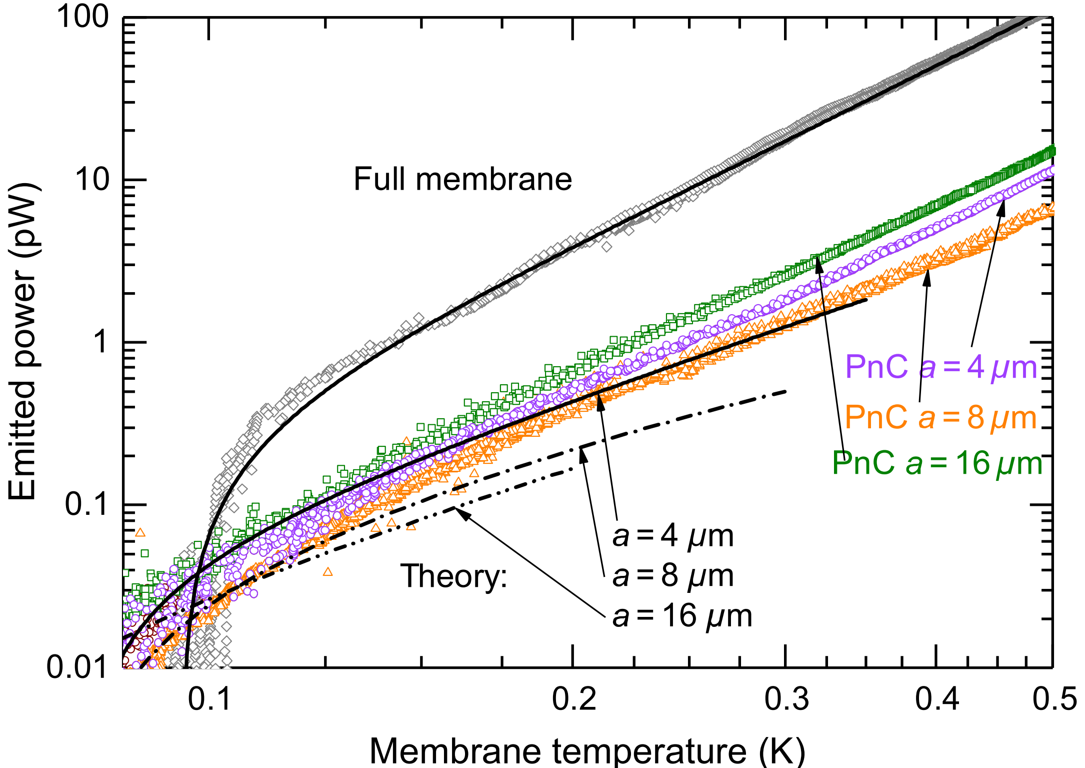

FIGURE 9 The measured emitted power as a function of the membrane temperature for the phononic crystals with different periods (purple, 4 µm; orange, 8 µm; green, 16 µm). Measured data for an uncut control membrane (gray) is also shown. Theoretical curves computed with the ballistic model are shown as lines (solid, 4 µm PnC and full membrane; dot-dash, 8 µm PnC; dot-dot-dash, 16 µm PnC). Reprinted from Reference [13], with permission of American Physical Society, copyright 2019.

thermal conductance as a function of the PnC structure's period can be explained by the interplay between incoherent and coherent phonons. The results suggest that incoherent phonons become more dominant with the growing period. This means that there is a practical limit for the period where the coherent phonons still dominate. This limit depends on the geometry of the sample and in this case was around the 10 µm scale.

2.4.2 3D phononic crystals

This section is partly based on article PIV. The earlier 3D PnC studies in our group are focused only on sample fabrication. The studied fabrication method was colloidal crystallization of mono-disperse spherical sub-micron particles [25]. With this method the PnC is created by the self assembly of the spherical particles. This kind of self-assembly of colloidal particles can be achieved in three main ways, which include capillary assembly, gravitational sedimentation and vertical deposition [76]. The method studied by our group was vertical deposition and polystyrene (PS) was chosen for the material of the spheres since PS spheres are commercially available as colloidal suspensions.

3D PnC structures were achieved by using substrates with in-situ etched confinement boxes. When using vertical deposition the spheres self-assemble into the etched boxes. The confinement boxes allow one to determine the size of the PnC, but they also reduce cracking of the crystal and increase the size of domains in the crystal. Samples fabricated using 260 nm PS spheres with confinement boxes of different sizes are shown in Figure 10a,b. The boxes were etched into a SiN substrate and then the substrate was coated with a layer of TiOx to increase the hydrophilicity of the surface. As can be seen from Figure 10a, even the largest 250 μm boxes have crystals with a single domain. This domain size is a lot larger than the surrounding domains on the substrate surface [25]. It was also shown that the fabrication of continuous metallic wires on top of these crystals is possible using e-beam lithography and lift-off [**PIV**].

Another way to fabricate the confinement boxes is to use the same 3D lithography method that is used in this study for PnC fabrication [**PIV**]. A 20 μm high surrounding structure was made out of IP-L 780 resist on a glass substrate and later with IP-Dip resist on a silicon substrate. Then vertical dipping was done with a solution of 260 nm PS spheres as with the in-situ etched boxes before. A sample fabricated with this method using an IP-L 780 confinement structure is shown in Figure 10c. Again a crystal is formed inside the box but interestingly no spheres were deposited on top the surrounding structure. This is a promising result as measurement electronics need to be fabricated on top the crystal for measurements and the deposition of spheres outside of the confinement box would make the fabrication almost impossible.

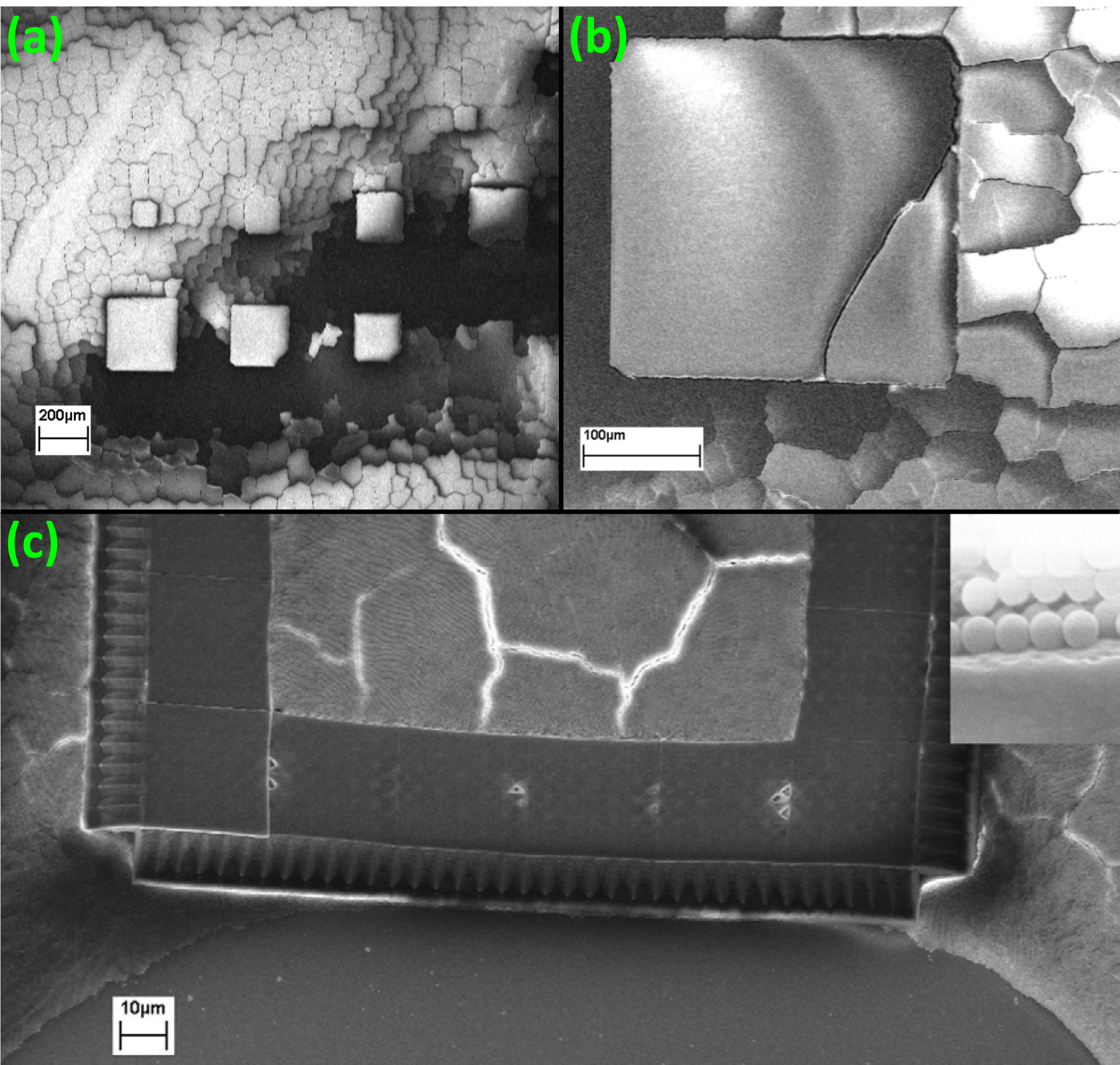

FIGURE 10 (a) A scanning electron micrograph of a range of different etched confinement boxes on a sample dipped in a 10 % solution using a speed of 0.02 mm/min. The areas outside the boxes have domains ranging from 30 - 70 μm while the domains in the etched boxes are significantly larger [25]. (b) A close-up view of a 250 μm x 250 μm confinement box, which has a continuous crystal region that is several times larger than the domains in the surrounding area [25]. (c) A scanning electron micrograph of PS colloidal crystals deposited into the confinement box structure fabricated with 3D lithography. Inset: a magnified image of the edge of the confinement box, showing the cracking happening there [**PIV**]. Adapted from References [25] and [**PIV**], with permission of Elsevier (copyright 2014) and IOP Publishing (copyright 2017).

3 FABRICATION METHODS

3.1 Two-photon lithography

Two-photon or multiphoton lithography is a lithography process which utilizes multiphoton absorption [77]. Usually two-photon absorption is used with infrared (IR) light so that the absorption happens at the UV region and UV sensitive resists can be used. Two-photon lithography allows one to expose a three dimensionally isolated point in a resist due to the nonlinearity of the two-photon absorption process. The absorption is dependent on the square of the the radiation intensity. The two-photon absorption process is usually described by a very straightforward expression, which gives the change in the radiation intensity I over a distance dz. This expression takes the form

$$-\frac{dI}{dz} = \alpha I + \beta I^2 \tag{32}$$

where the coefficients α and β are the absorption coefficient for single-photon and two-photon absorption respectively [78]. The two-photon absorption coefficient β is medium dependent and for radiation of a single wavelength, as is the case for lasers, it is given by the expression

$$\beta = \frac{8\pi^2\omega}{c^2\epsilon}\mathrm{Im}\,\chi^{(3)} \tag{33}$$

where c is the speed of light, ϵ is the dielectric constant and $\chi^{(3)}$ is the third-order nonlinear susceptibility in the case of two-photon absorption [77]. The expression tells us, that for a chosen wavelength the coefficient β is linearly proportional to $\mathrm{Im}\,\chi^{(3)}$. Therefore, from Equation (32) we can say that two-photon absorption becomes relevant only when dealing with high intensities.

Simply put, Equation 32 tells us that, two photons can be absorbed at the same time only when the intensity of the radiation becomes high enough. When the two photons are absorbed by the material, it transitions from its ground state to an exited state. The energy of this excited state is equal to the sum of the

energies of the photons. Since it is not possible for the two photons to always be absorbed simultaneously, usually a virtual state model is used to describe the two-photon absorption process. Using this model, the process starts with the first photon exciting the material to a virtual state. Then a secondary absorbed photon causes the material to excite from this virtual state to the real excited state [79]. The energies of the absorbed photons thus don't need to be equal as long as the combined energy is enough to go from the ground state to the excited state. However, in practice commonly just one wavelength is used, as focused lasers are needed to reach the required high intensities.

Two-photon lithography can be done with resists which have been specifically designed for it, but most common UV resists can also be used. The negative-tone resists designed for two-photon lithography are often in liquid phase as is the case with the IP resists (Nanoscirbe GmbH) used in this project. The wavelength has to be set so that it is about double the wavelength required for the resist. So for example with UV resists, IR radiation needs to be used, because then the combined energy of the IR photons will equal the energy of a UV photon. Due to the non-linearity of the two-photon absorption process, it can only take place in a place where light is tightly focused to an extremely high intensity. This means that using two-photon absorption, it is possible to expose the resist material in a small three-dimensionally isolated spot i.e. a voxel [80]. If linear one-photon absorption was used for the exposure of the resist, the polymerization would take place all along the path of the light. This difference is schematically shown in Figure 11, where the volumes for both processes are compared using UV resist as an example. This difference is the reason why two-photon absorption makes three-dimensional lithography possible. The needed high intensity is the only requirement to achieve two photon absorption in practice. One way to do this is focusing a femtosecond pulsed laser with a microscope objective. This method is used in the Photonic Professional system by Nanoscribe GmbH which was used in this thesis. The system uses a 780 nm laser with a pulse rate of 80 MHz.

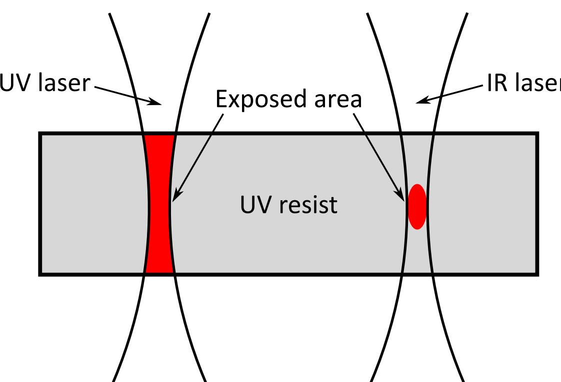

FIGURE 11 The difference between two-photon and single-photon absorption when exposing a UV resist. With UV light the resist is exposed everywhere in the path of the light, but with IR light and two-photon absorption the resist is exposed only in a small voxel where two-photon absorption takes place.

3.1.1 3D-lithography

The usual way of using two-photon absorption for nanofabrication is 3D-lithography. This is the main fabrication method for which devices like the Photonic Professional were designed. In this method the focused laser is used to expose a liquid or soild phase negative-tone resist to fabricate 3D structures out of the resist material [81–84]. The sample is moved accurately in three dimensions for example by using piezoelectronic actuators in such a way that the voxel created by the focused laser draws the wanted structure into the resist. Then, the extra resist is removed with a developer similarly to traditional lithography. This method has been used for a variety of applications such as photonics [85, 86], micro-optics [87, 88], microfluidics [89, 90], mechanical metamaterials [91, 92], biomimetics [93, 94] and micro and cell biology [95–97], to just name a few. The aim of most of these applications is the direct patterning of complex shapes and thus negative-tone resists are often used. In addition, often the highest resolutions are provided by liquid resists, which allow only negative-tone operation. In our case liquid phase IP-Dip or IP-L (Nanoscribe GmbH) are used, since they are specifically designed for our instrument.

With the Photonic Professional system there are traditionally two main writing modes for 3D structures, which are shown in Figure 12a,b. The immersion oil mode (Figure 12a) works only with transparent substrates, since the laser beam needs to go through the substrate. However, this mode allows the use of any type of resist, even solid state resists. The more versatile mode is the dip-in mode (Figure 12b) where any type of substrate can be used, since the laser is focused directly into the resist. With the dip-in mode, you are limited to liquid phase resists, which was not an issue for the 3D PnC fabrication step, since a liquid phase resist was going to be used anyway. This was mainly because opaque Si substrates were needed instead of glass ones since their thermal conductivity high enough not to interfere with the measurements. The fact that any substrate can be used with the dip-in mode is the main reason why it was used for the fabrication of the 3D PnC structures in this project. In addition the immersion oil mode has issues with tall structures since the laser has to travel through the already drawn structure. The modes shown in Figure 12c,d are used with 2D or 2.5D lithography and they are discussed in Section 4.1.

3.2 Reactive ion etching

Reactive ion etching (RIE) was used in this project to clean the samples between different fabrication steps. RIE is a type of dry etching [98], where RF-plasma is used to etch a solid substrate. Reactive gas is fed into the vacuum chamber, where the RF-plasma forms both ionized and excited molecular species. The formed excited molecules are extremely reactive, and thus chemical etching of the substrate takes place. The ionic species are accelerated by the plasma causing also phys-

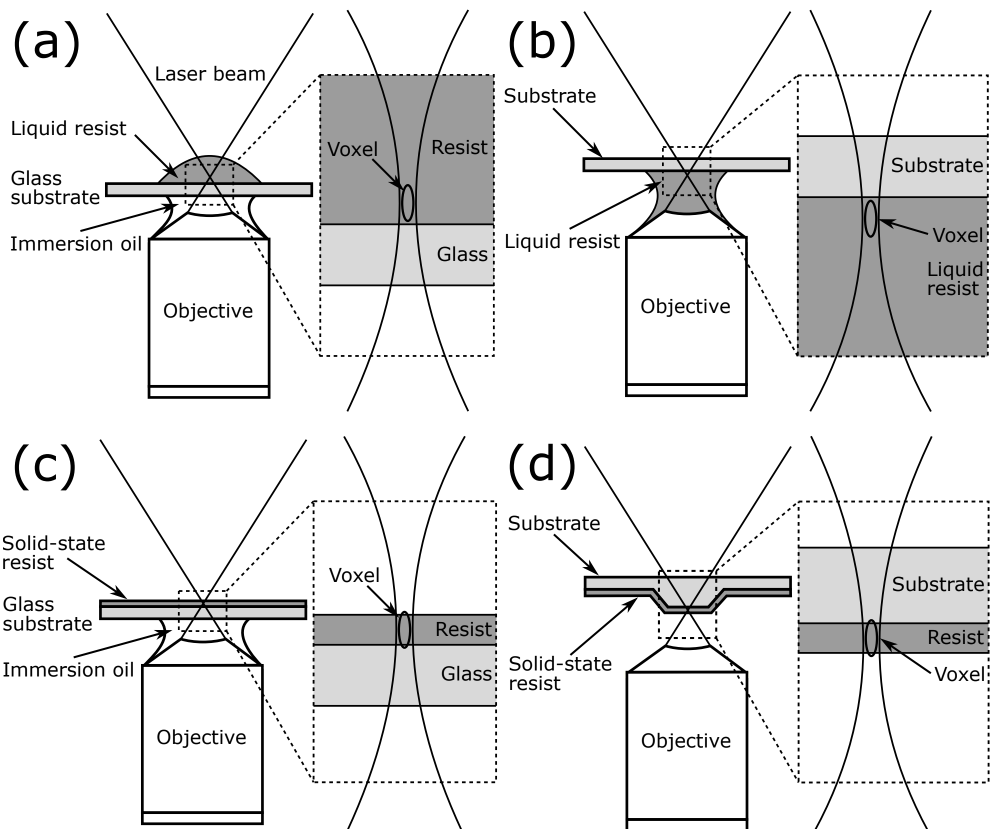

FIGURE 12 Different exposure methods for two-photon lithography with liquid or solid-state photoresists. (a) The oil-immersion method, where an inverted high numerical aperture (NA) objective is in contact with an immersion oil. The refraction index of the oil is matched to the used glass substrate. A laser beam is well focused into a liquid resist on the other side of the substrate, where the two-photon absorption process forms the voxel. The sample can be moved in all three dimensions allowing the drawing of a 3D structure into the resist. (b) Dip-in lithography method for liquid negative-tone photoresists. An inverted objective is dipped into the liquid resist and the laser is focused directly into the resist. (c) Immersion-oil or air-gap objective method with a glass substrate. The laser is focused with an inverted objective through the glass into the interface of the resist and the glass substrate. (d) The air-gap objective method for patterning over uneven topography. An inverted air-gap objective is used to focus the laser from the resist side. The sample is moved in z-direction so that the focus spot of the laser follows the topography on the substrate surface.

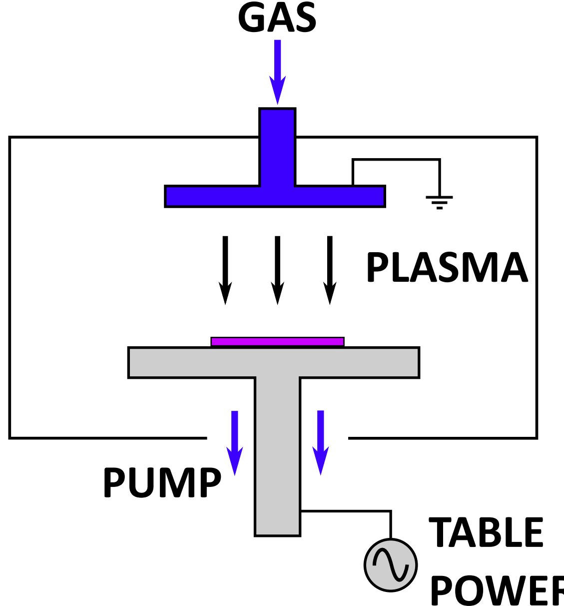

FIGURE 13 A simple schematic of a reactive ion etcher. The process gas is fed from the top through the top electrode. Then the plasma is created between the electrodes. The sample is placed on the bottom electrode. The reaction products are pumped away from the bottom.

ical etching processes. In Figure 13 there is a simple depiction of a reactive ion etcher.[98]

By increasing the RF power the amount of physical etching processes can be increased. This enhancement can also be achieved by lowering the pressure, biasing the substrate and adding a stabilization gas like N_2 or Ar. By controlling the amount of ion enhancement the etching process can be changed between chemical and physical etching processes. When there is little ion enhancement, the chemical etching processes are dominant and vice versa. With chemical etching, the etching profile is isotropic and selective since the gasses can be selected so that only certain reactions are possible. With physical etching processes, the etching is anisotropic and unselective instead. With RIE different gasses are used for different processes. In this project only oxygen was used for removing resist residue and other impurities from the sample surface.

3.3 Physical vapor deposition

Physical vapor deposition (PVD) is normally used to describe the ejection of material from a solid state target. This process can be used for thin film deposition of various materials. The material ejected from the target is transported through vacuum to the surface of a substrate. The material that arrives at the substrate is then deposited on the surface. The ejection of atoms from a target material can be achieved in many ways. The two most common techniques are evaporation and ion bombardment or sputtering. Both of these methods were used for different

purposes in this study.

In theory, evaporation is a very simple deposition method. At least with metals, the evaporation can be achieved just by heating the target, since the vapor pressures of hot metals are high enough. If a hot metal is put into a vacuum chamber, the evaporating atoms can be transported onto the surface of a substrate. The instruments used for evaporation can have different levels of vacuum. Usually they are either high vacuum (HV, $1 \times 10^{-1} - 1 \times 10^{-7}$ Pa) or ultrahigh vacuum (UHV, $1 \times 10^{-7} - 1 \times 10^{-9}$ Pa) systems. In this study, a UHV evaporator was used for the evaporation of the metals for the NIS junction fabrication, as line-of-sight transport is required. A HV evaporator was used for the evaporation of aluminum oxide, because the evaporation of insulators would cause complications for a UHV system.[98]

With a high enough vacuum, the ejected metal atoms will not collide with any other particles while moving through the vacuum. No collisions will take place because the mean free path (MFP) has become larger than the size of the evaporation chamber, and therefore the ejected atoms will transfer to the substrate surface via a direct line-of-sight route. This line-of-sight transport, in combination with low deposition temperatures, leads to film deposition only on planar horizontal surfaces and vertical planes such as the sidewalls of a 3D structure will not be coated. For this reason, with evaporation a sample needs to be coated from multiple angles to get good coverage over all the wanted features in many cases. When doing evaporation, the target can be heated in many ways. The most common way is to use an electron beam. This method is schematically described in Figure 14a and it is also the method applied in both the HV and UHV instrument used in this project.[98]

In the second PVD method, sputtering, a target is charged negatively and atoms are ejected from it using positive ions (usually argon) coming from a glow discharge plasma. Then like with the evaporation method, the ejected atoms are transported through vacuum onto the substrate. With this method, the atoms arrive at the substrate with high energy, which improves adhesion and film density, since loosely bound impurity atoms will be knocked out of the surface by the energetic atoms. However, too high energies can lead to damage to the sample. With sputtering, usually higher deposition rates than with evaporation can be achieved. Also due to the higher pressures used in sputtering, contrary to evaporation, the atoms ejected from the target will experience a lot of collisions before arriving at the substrate. This means that in sputtering there is no line-of-sight transport, thus better coverage over topographies can be achieved without using multiple deposition angles. The sputtering process is depicted in Figure 14b. In this study sputtering was used to coat samples with gold for SEM imaging, because the sputtering instrument is a lot faster to use than the evaporators.[98]

With PVD the deposited film thicknesses are usually in the 10-100 nanometer range, so the thickness needs to be monitored at the ångström scale. In practice, this can be done with a quartz crystal microbalance (QCM). A QCM is device that uses a single crystal quartz resonator to detect a change in mass. The resonant vibration frequency of the quartz crystal can be measured very precisely,

and it depends on the mass of the resonator. Piezoelectric effect can be used to measure the vibration frequency. As material is added on the crystal due to the deposition, the total mass of the resonator will change which in turn leads to a change in vibration frequency. The change in the frequency is then detected by the QCM. A QCM can be so precise that it is even possible to detect differences of one or a few atomic layers. Both the evaporators used in this study were fitted with QCMs.

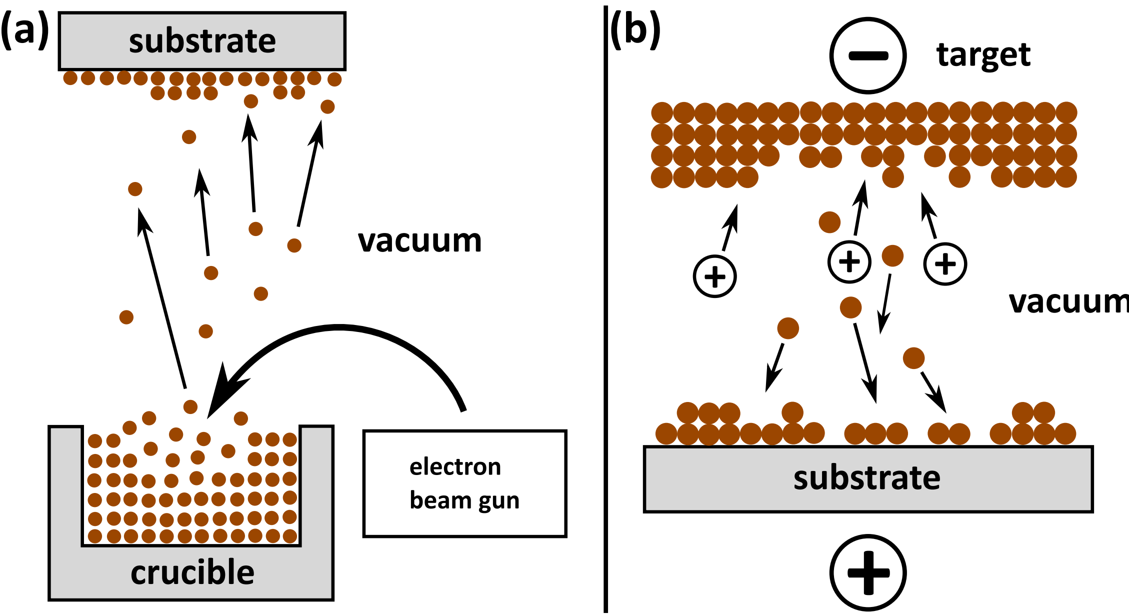

FIGURE 14 (a) Metal evaporation using an electron beam. A magnetic field is used to direct the electron beam into the crucible which leads to the vaporization of the metal. The evaporated atoms then transport through the vacuum onto the substrate above. (b) Metal deposition with sputtering. Positive ions formed by the glow discharge plasma cause atoms from the negatively charged target to eject. These ejected atoms then transfer through vacuum onto the substrate.[98]

4 EXPERIMENTAL METHODS AND FABRICATION RESULTS

This chapter is based on articles PI, PII and PIII. The sample fabrication of the PnC samples consisted of two main steps. The first step was the fabrication of the phononic crystal and the second was fabricating the measurement devices on the crystal structure. The measurement devices consisted of two SINIS junctions, one of which is used as a heater and the other as a thermometer. In this chapter I will first go through the development of the new 2.5D fabrication method for device fabrication on large topographies. Then I will present the basic fabrication procedures and also how the fabrication processes were optimized during the study.

4.1 Development of the 2.5D fabrication method for devices on large topographies

A new method had to be developed for the fabrication of the SINIS junctions on the 3D PnC structures, as no established method available to us allowed such fabrication. The 3D laser lithography used for the PnC structures was chosen to be the basis due to its inherent 3D capabilites. Previously there had been very few attempts to use two-photon lithography with positive-tone solid state resists for the fabrication of metallic nanostructures. There were some examples of groups using two-photon lithography in combination with electrodeposition of metals and lift-off for 3D structuring of photonic metamaterials [99], magnetic microrobots [100] and magnetic nanostructures [101]. Recently, there was one study [102], which pointed out the relevance of two-photon absorption direct writing in the fabrication of 2D, large metal nanostructures with the smallest features being around 400 nm, utilizing a positive-tone resist and lift-off.

We first studied the capabilities of two-photon lithography with a positive-tone resist for 2D fabrication of metallic leads. We showed that this method is very suitable for fast large area fabrication with line widths down to 330 nm [**PI**].

The maskless nature of the method makes it an interesting alternative to traditional UV lithography. Similar fabrication can also be done with UV lasers using single photon absorption, but at least in theory the two-photon method should allow faster writing speeds due to the quadratic scaling of the writing speed in relation to intensity.

For this project I developed this method even further. For studying the 3D PnC structures I needed a fabrication method capable of making measurement devices on top of a 3D structure. Using two-photon lithography came naturally since we had shown its capability for 2D fabrication, and two-photon lithography instruments like the Photonic Professional are designed for 3D fabrication. Using the three-dimensionally manipulatable piezo-stage it is possible write a pattern on any known 2.5D topography. The dimensions of the topography have to be known since the system can't automatically follow the topography. However, due to size of the voxel this information does not need to be very precise. First as a proof of concept we showed that it is possible to fabricate metallic wiring on a 20 μm high topography [**PI**]. Furthermore, I showed that with more advanced resist systems and improved patterning, the fabrication of advanced superconducting devices on a similar topography is possible with this method [**PII**].

The fabrication process does not differ from traditional UV or electron-beam lithography, except for the exposure. Normal positive-tone UV sensitive resists can be used, which in our case were the AR-P 3120 and AR-P 3540 by Allresist GmbH. The resist coating can be done by any method. However, for 2.5D-lithography the use of spray coating would be preferred, since more conformal coatings can be achieved over different topographies [103]. In our setup there are two different writing modes, which are suited for a variety of samples. For writing purely 2D patterns the mode in Figure 12c can be used. In this mode either an immersion oil or air-gap objective is used to focus the laser through the substrate, so transparent substrates need to be used. The highest resolutions can be achieved using this mode with the oil-immersion objective. For 2D lithography on an opaque substrate or for 2.5D lithography over a topography, the mode shown in Figure 12d is needed, since now writing through the substrate is not possible and the objective can't be in contact with the sample. This is the more versatile mode, but since an air-gap objective has to be used the resolution is more limited.

The width of the exposed line w (voxel size) can be easily controlled by the laser power and the writing speed v. An expression for the width can be theoretically derived if linear motion of the focus spot of the laser is assumed. This expression takes the form

$$w = \omega_0 \sqrt{\ln\left(\frac{\sigma_2 \omega_0}{C} \frac{\sqrt{\pi}}{2} \frac{I_0^2}{v}\right)}, \tag{34}$$

where ω_0 is the waist of the Gaussian beam at the focal plane, I_0 is the time-averaged photon flux intensity of the laser beam at the center (photons/area/s) and σ_2 is the effective two-photon cross section [**PI**]. $C = \ln[\rho_0/(\rho_0 - \rho_{th})]$ is a ma-

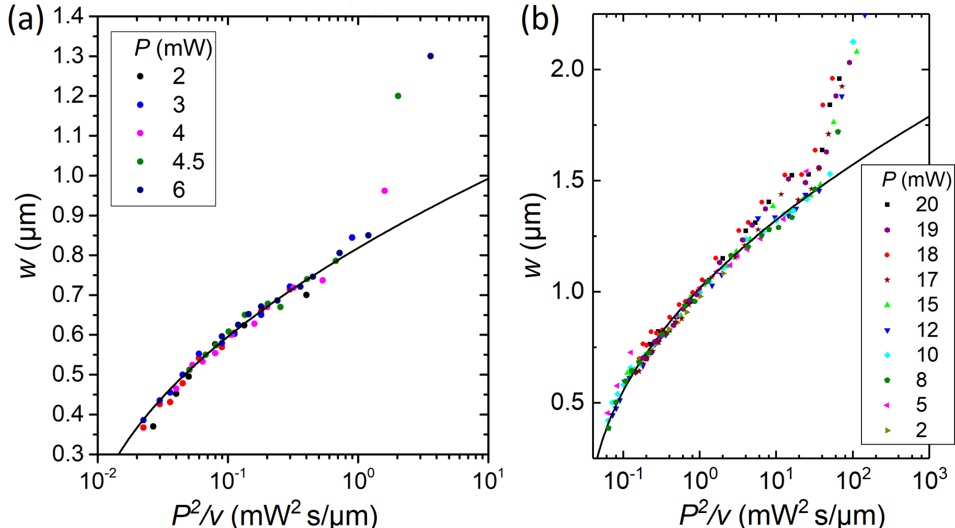

FIGURE 15 The measured line width as a function of P^2/v for lines drawn with an immersion oil objective (a) and an air-gap objective (b).The measured data is shown as the solid points and the lines are two-parameter fits based on Equation 34. The deviation at high P^2/v values is due to the collapse of the undercut profile of the resist. Reprinted from Reference [**PI**], with permission of Wiley-VCH GmbH, copyright 2020.

terial parameter depending on the resist, with ρ_0 being the initiator density and ρ_{th} the threshold radical density needed to cause a reaction inside the resist [**PI**, 104, 105]. In setups like ours, the parameter determining I_0 is the output power of the laser P, as the terms are directly proportional. In consequence, Equation 34 tells us that the line width scales as P^2/v. Measurement data supporting this scaling is shown in Figure 15.

4.2 Fabrication of the phononic crystal structure

All the 3D phononic crystal structures, that were measured in this study, were fabricated with 3D-lithography using the Photonic Professional system by Nanoscribe GmbH. This is a system that uses two-photon absorption to produce 3D structures out of a negative resist. The instrument has a femtosecond pulse laser with a pulse rate of 80 MHz and a wavelength of 780 nm. This wavelength has been chosen so that with two photon absorption the system works with UV sensitive resists.

4.2.1 Creating the 3D design for the structure

The design of the structure has to be provided to the Photonic Professional system as a GWL (general writing language) file. This file has to contain the start and end points of all the lines which need to be exposed to create the wanted structure. In addition to the point coordinates, the file must contain all the writing parameters

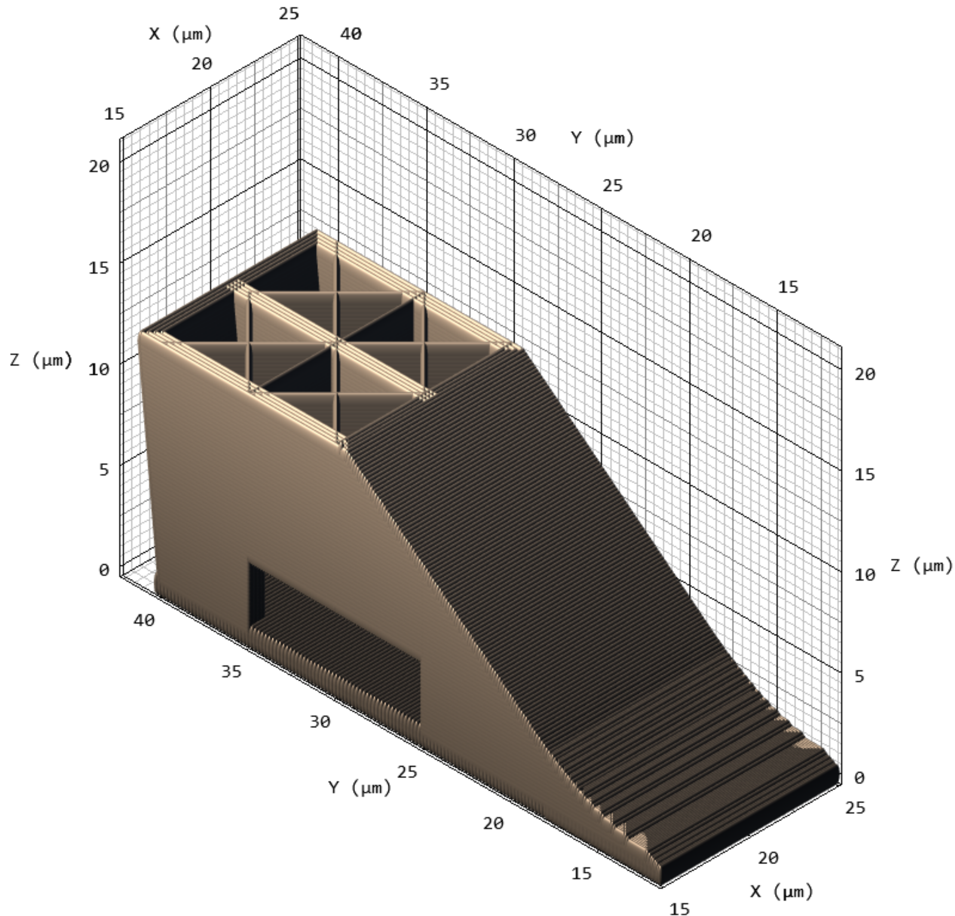

FIGURE 16 A 3D model of one of the ramps generated with the DeScribe program. The model is taken at a point when the ramp is about halfway drawn, so that the supporting structures inside are visible. There is a hole on the side, so that after the exposure the liquid resist has a way to escape.

like laser power and writing speed. This file can be made in many different ways. The simplest way is to generate the file directly using Nanoscribes DeScribe program that is provided with the system. However, this way is also the most limited since the program allows only very limited coding, basically only for-loops can be used. For this reason we mainly use this method only for small test structures and for combining designs made in other ways.

A design can also be generated by using CAD software. After creating a 3D design with CAD, it can be sliced using the DeScribe program to create the GWL file for the lithography instrument. With this method, DeScribe only uses the outer shell of the provided design and fills the inside with a chosen preset hatching style. So this method allows fast and easy design of simple shapes, but is not suitable for more complex designs. The only way to fully control how a structure is drawn is to use a script to directly create the GWL file containing the coordinates for the lithography system.

For the PnC structures in this study I used all three methods mentioned here. The spheres for the PnC structure were modeled with Autodesk Inventor CAD software. These 3D models where then sliced with the DeScribe program

so that they are filled by drawing concentric circles. The sphere designs were combined into the 3D lattice using the DeScribe program. The designs for all the other more complicated parts were created with Python scripts. The design of one of the ramps created with Python is shown in Figure 16. All the different parts of the structure can be combined into one GWL file, which is then given to the computer controlling the lithography system.

4.2.2 The fabrication procedure

With the GWL file containing the 3D design for the structure finished, the actual fabrication can start. First a small piece of substrate (8 mm x 8 mm) is cleaned in hot acetone using a sonicator. The substrate materials used in this study were sapphire for the earlier samples and nitridized silicon for the later samples. The writing mode used for the fabrication was the dip-in mode presented in Section 3.1.1. For this mode we use the liquid IP-Dip resist made by Nanoscribe GmbH. With this mode the substrate is glued onto the sample stage, so that it will sit upside down in the instrument, thus facing the focusing objective. A droplet of the liquid resist is put on the cleaned substrate after gluing it onto the sample stage. The 3D design of the structure is given to the system via a computer, which controls the whole system. The design file also has all the parameters for the process. After giving the design file, the coordinate system of the instrument can be fixed by measuring the z-coordinate of the substrate surface and the tilt of the substrate. The tilt is measured by finding the z-coordinate of the interface (substrate surface) in a grid of points. Then the instrument will draw the structure automatically into the resist.

After the structure has been exposed into the liquid resist, the sample is developed by keeping it in propylene glycol methyl ether acetate (PGMEA) for 20 minutes. Then the sample is rinsed in isopropanol (IPA). To strengthen the structure and minimize shrinkage, a post-print UV curing is done for the PnC samples [106] as follows: without drying, the sample is directly transferred to an IPA bath containing 0.5 wt% 2,2-dimethoxy-2-phenylacetophenone (DMPA) and a 20 minute exposure is done with 366 nm UV light. The DMPA works as a photoinitiator, which together with the UV light adds more cross-linking to the resist, making the structure stronger. After this the sample is rinsed with IPA again and then dried with N_2 gas. The final step in fabricating the PnC structure is the evaporation of a 200 nm AlOx capping layer, using a high vacuum electron-beam evaporator. This is done to both strengthen the structure and to create a homogeneous more smoothed surface. Both before and after the evaporation, the structure is baked on a hotplate at 150 °C for 20 minutes to release the stresses in the structure.

4.2.3 Optimizing the PnC structures

The first thing to optimize was the fabrication of the lattice of spheres for the PnC structures. Getting the wanted simple cubic lattice required a lot of optimization

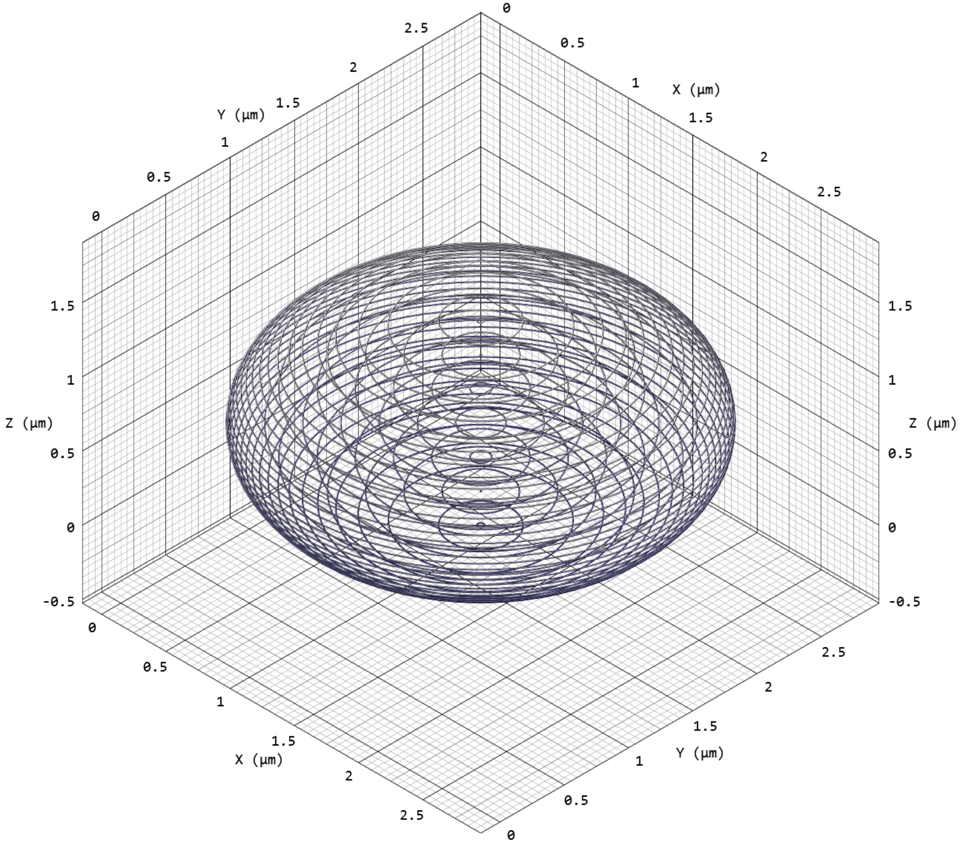

FIGURE 17 A 3D model showing the path of the voxel when drawing a sphere with a 3.1 µm diameter. The model was generated with the DeScribe program by Nanoscribe GmbH. Due to the voxel elongation in z-direction, an ellipsoidal shape of the path will produce a spherical structure.

of the writing parameters and the design. The design for the spheres has to be distorted just the right way, because the voxel has a tall and thin shape like a rice grain [107]. The final design, which produced a good spherical shape is shown in Figure 17. To get the smallest possible contact area between the spheres, important for maximal impact of the crystal to the band structure, the lattice constants and the writing parameters had to be tightly optimized. After a lot of tests with different parameters I got a good result for spheres with a diameter of 3.1 µm. An SEM image of such a structure is shown in Figure 18. This was the smallest diameter with which a good spherical shape was still achievable. The writing parameters used for the exposure are shown in Table 2. After finding the smallest possible diameter, a diameter of 5.0 µm was chosen for the second PnC structure as spheres of that size could still be feasibly simulated with FEM. Larger spheres require the calculation of a higher number of modes and thus take more time to simulate. The spheres are exposed completely by drawing concentric circles at different layers. This simple hatching style was available in the DeScribe program, so the designs were made with CAD software as stated in the previous section.

To be able to fabricate the SINIS junctions on the PnC, there has to be a flat surface on top of the sphere lattice. Also to connect leads to the junctions, there

TABLE 2 The writing parameters used for the PnC structure fabrication with the Photonic Professional system.

Parameter	Value	Parameter	Value
PiezoScanMode	On	PowerScaling	∼2.7
ContinuousMode	On	LaserPower	20 % (∼10.8 mW)
ConnectPoints	On	SettlingTime	200 ms
PerfectShape	Off	ScanSpeed	70 μm/s

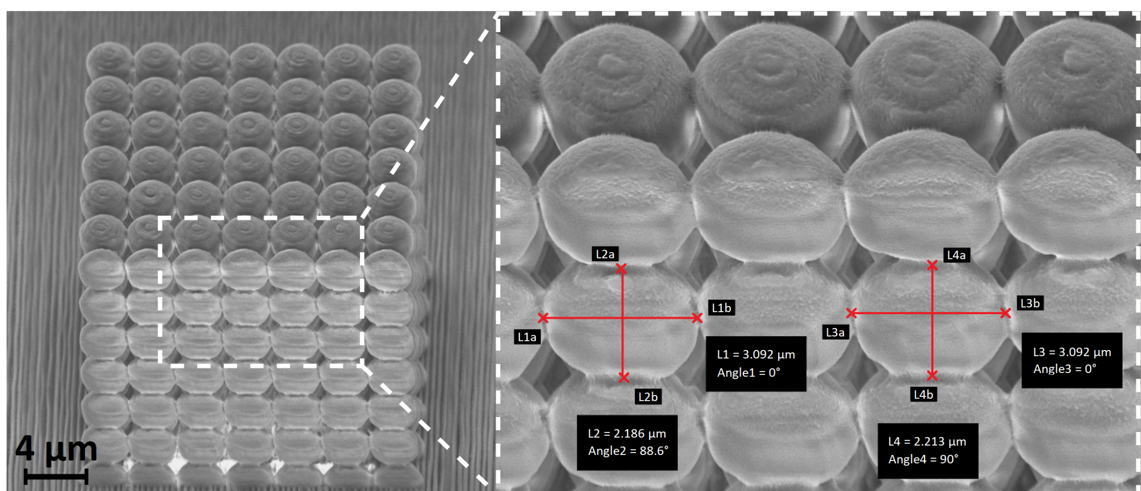

FIGURE 18 An SEM image of the PnC consisting of spheres with a diameter of 3.1 μm. The closest face consists of half spheres and the image is taken from a 45° angle. After correcting for the imaging angle, the diameter is reasonably consistent all around.

have to be slopes for the wiring to climb on to the structure. Therefore, slopes and a suspended plate of thickness 1.6 μm are fabricated on the structure according to the schematic in Figure 19. The fairly gently sloping ramps are needed mostly due to the following resist coating steps needed for lithography. The spin coating method used here can't create a uniform film on steep topographies. If for example spray coating was available the ramps could be made a lot steeper. For the same reason small walls (height 3.5 μm) are drawn at the edges of the top of the structure, to force the spin coated resist to stay on the platform. For earlier samples the top film was connected to a full layer of spheres, but early measurements showed that when using such a geometry, the thermometer signal was too weak. This was because the solid angle subtended by the thermometer was so small. So for later samples, the film on top was made suspended in the middle, as shown in Figure 19, to limit the direct flow of heat from the heater to the 3D PnC making sure that the thermometer couples to the heater better. The same geometry was used for bulk control samples and PnC samples with both sphere diameters.

The fabrication of the ramps had already been mostly optimized in earlier studies [108]. Drawing the film on top was also simple for the earlier samples with full lattices of spheres underneath. There was no issue drawing the film with straight lines. However, when we moved to the suspended geometry, we

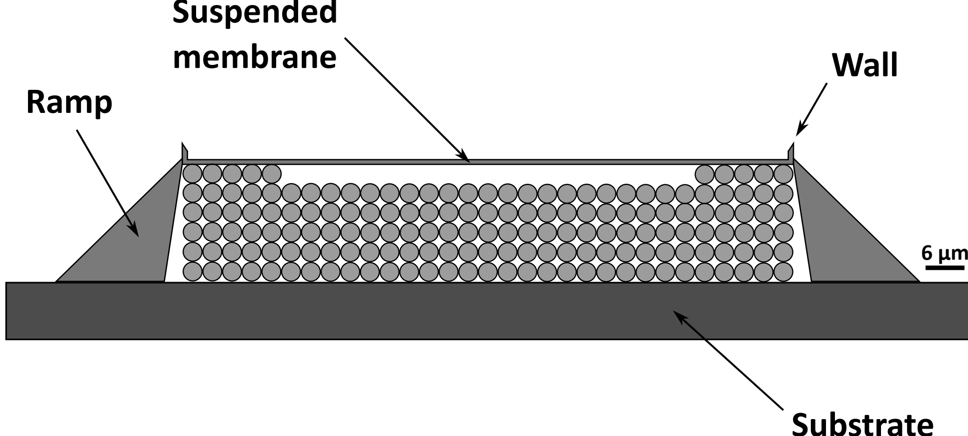

FIGURE 19 A to-scale schematic cross-section of the phononic crystal structure completed with ramps, and a film on top for the measurement junctions. The ramps are sloped also on the side of the lattice to reduce the contact area to the PnC structure. In the abandoned geometry the empty area below the film was also filled with spheres. The thickness of the membrane is 1.6 µm.

ran into a problem. The film drawn using straight lines had a large dent in the middle, as shown in Figure 20a. This dent made the following lithography step impossible, since with spin coating a good resist coverage could not be achieved. The dent is caused by the difference in the shrinkage of the base structure and the film. To our surprise, after doing some tests we found out that the shrinkage can be controlled by altering the laser drawing path when exposing a structure. This means that the shrinkage depends on the direction of the patterned lines and seems to be worst perpendicular to the drawn lines, as shown by the curving of the sidewalls in Figure 20a.

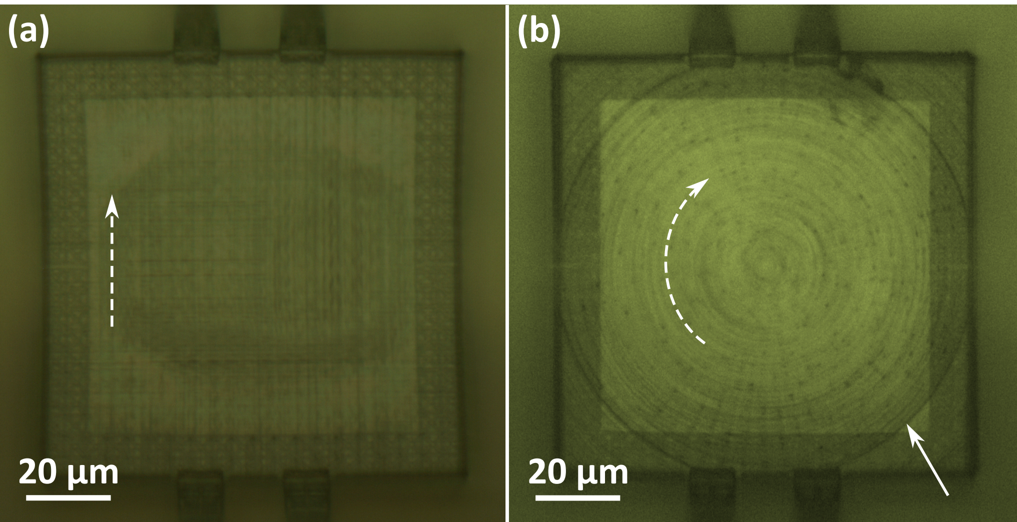

FIGURE 20 Optical micographs of the difference between the two drawing styles for the film. (a) A film drawn with straight lines, which has a large dent (darker area). (b) A film drawn with concentric circles, creating a flat membrane surface. Arrow points to the dark line caused by the different design styles. The dashed arrows show the drawing directions.

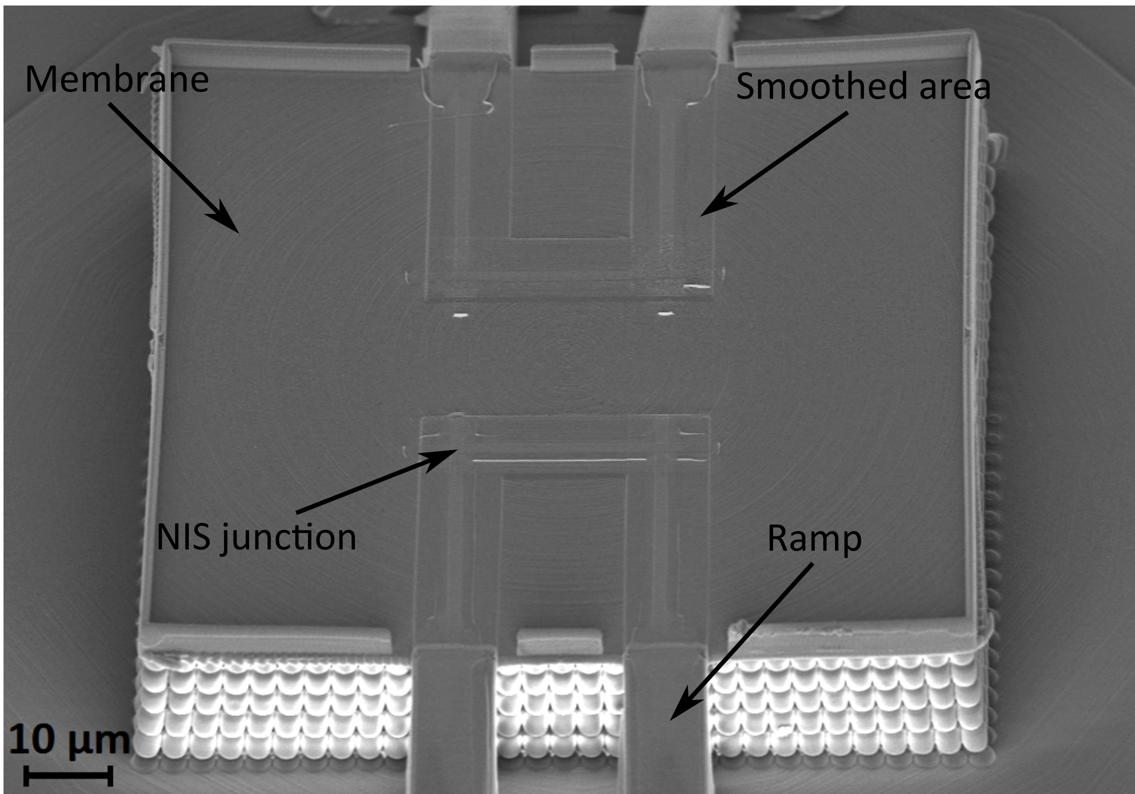

FIGURE 21 An SEM micrograph of the full PnC structure with the free hanging film and ramps. The SINIS junctions, fabricated later on the smoothed areas, are also visible in the figure.

After trying different drawing styles to fabricate a flat suspended film with the 3D lithography system, I found out that the best way to make the film is to expose the whole film using concentric circles. In addition, the circles need to be drawn with varying starting locations in order to not create a highly exposed line into the film. A structure with the suspended membrane drawn with this method is shown in Figure 20b. Because of the square shape of the structure, the corners of the film had to be designed with a Python script, but the circular middle part could be hatched with DeScribe so the design for it was done with CAD. A dark line is visible at the interface between the differently designed parts in Figure 20b.

Using the circular drawing style provided a flat film but introduced another issue. After fabricating metal leads on the film and testing them, we found that the leads were not continuous. Changing the drawing style altered the directionality of the unavoidable surface roughness. Now the ridges caused by the voxel ran almost perpendicular to the metal leads and introduced breaks in them. So in addition to the circular drawing style, the film had to be smoothed at the locations where metal lines will be deposited. The smoothing is done by drawing straight lines on the film with really high density of lines. The smoothed areas are lifted a little over the film to fully cover the ridges on the film. The smoothing is done only at the specific locations to save time and reduce the introduced tension. An example of the full structure with the smoothed platform is shown in Figure 21.

Figuring out the fact that the circular drawing style reduced the shrinkage

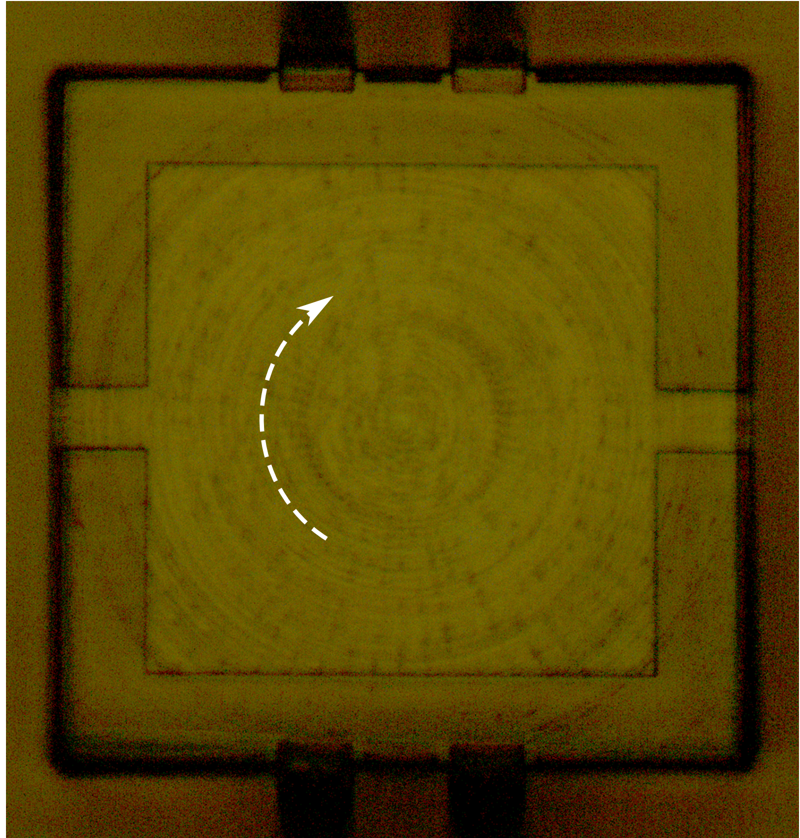

FIGURE 22 An image of one of the bulk control samples taken with an optical microscope. The hollowed volume with gaps in the sides is visible through the film. The dashed arrow shows the drawing direction.

issue with the resist also solved another problem. This far we had had large issues, when trying to fabricate any bulk structures with the 3D lithography instrument, and for this study we needed bulk samples as controls. Using straight lines to draw bulk structures introduced a lot of tension into the structures and deformed them badly. Now with the circular drawing method, making nice bulk samples was very easy. In Figure 22 there is an optical micrograph of one of the bulk control samples fabricated with the circular drawing style. There is no deformation of the shape at all, and similarly to Figure 20b, the suspended film is flat. For the bulk samples, small gaps had to be left into the sides (Figure 22), so that the liquid resist could escape the hollow volume under the film.

Even if such a complex 3D structure was fabricated successfully, the required additional steps for the SINIS junction fabrication introduced more issues. The coverage of the spinned resist was very inconsistent on the 3D structure. During the lift-off, as will be described later, the whole structure tended to get removed from the substrate very easily. Because of these issues, we decided to add a 200 nm thick AlOx capping layer on the entire sample. The layer was grown by evaporation using a high vacuum electron-beam evaporator. This material was chosen out of convenience but other materials could also be used. This step both strengthened the whole structure and provided a more homogeneous and smoother surface. Now the spinned resist consistently covered the structure and

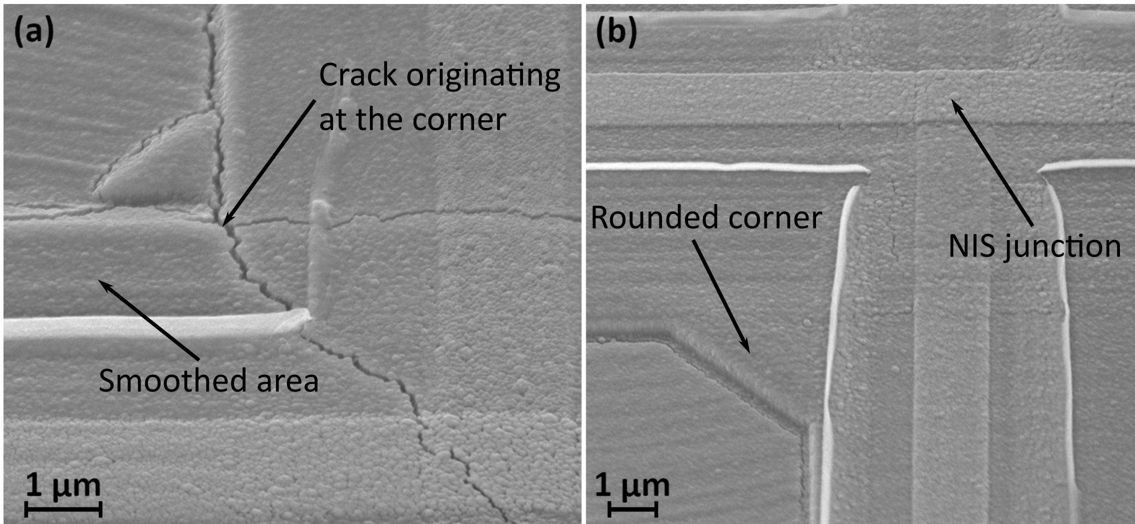

FIGURE 23 Cracking of the AlOx capping layer. (a) An SEM micrograph of a structure without rounding showing cracks originating at the inside corner of the smoothed area. (b) An SEM micrograph of a structure with rounding showing no cracks.

the structure was difficult to remove in the lift-off step. Both before and after the evaporation, the sample was baked on a hotplate at 150 °C for 20 minutes to release the stresses in the structure. However, even with all these steps the capping layer tended to crack at the inner corners of the smoothed area on the platform (Figure 23a). This cracking happened at the end of the following lithography process for the SINIS junctions. The different drawing styles between the film and the smoothed area introduces tension during the lift-off, which leads to the cracking of the capping layer. I was able to minimize this cracking issue by rounding the corners as shown in Figure 23b. Despite this solution, similar cracking at different positions on the structure remained an occasionally reoccurring problem, which reduced the yield considerably.

4.3 Fabrication of the SINIS junctions

After the PnC structure was finished, it was cleaned with reactive ion etching (RIE) using oxygen plasma, to prepare it for the SINIS junction fabrication. The junction fabrication starts with resist coating. A two layer resist system was chosen for the process, so that an undercut could be created. Our earlier tests had shown that without an undercut, the extra metal film was extremely hard to remove from the platform in the lift-off step [**PI**]. With this two layer system, the sample has to be first coated with a bottom resist (AR-BR 5460, Allresist GmbH). The coating was done by spinning. The bottom resist had to be diluted to a solids content of 9 % with PGMEA, so that a thin enough film (450 nm) was produced on a substrate surface. With thicker films, there were issues with resist residue around the PnC structure after developing the resist.

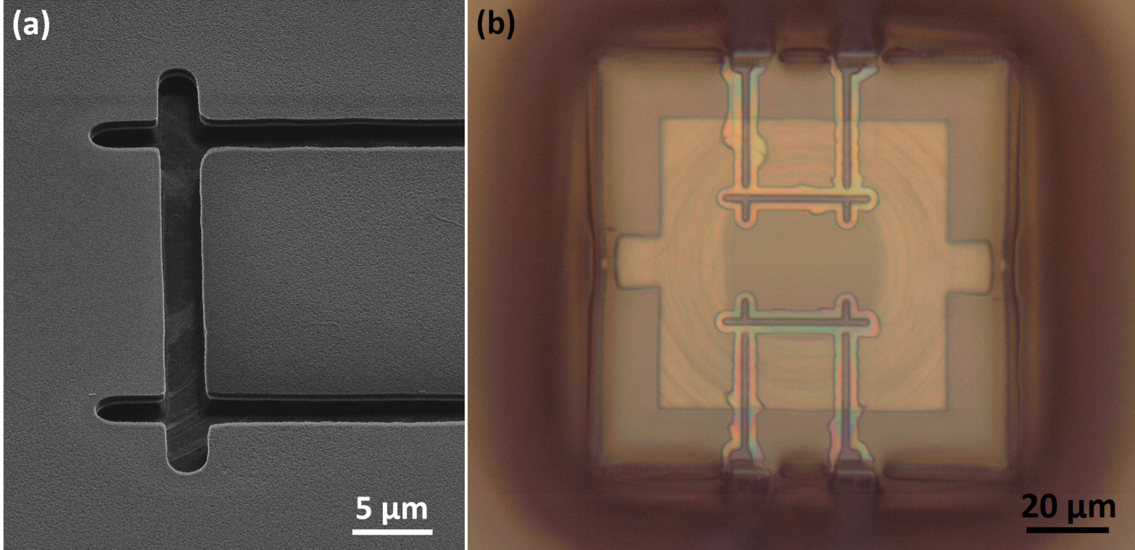

FIGURE 24 (a) A helium ion microscope micrograph of the developed patterns for the SINIS junctions with the baked bottom resist. (b) An optical microscope image of the developed SINIS junction patterns with the non-baked bottom resist. A micrometer scale undercut is visible, with bridge structures for shadow evaporation.

At the beginning of the project, the bottom resist was baked at 150 °C per the product information, but this allowed only for a very small undercut (Figure 24a). We then decided to start keeping the samples in vacuum overnight, instead of the baking, to remove the solvent without a glass transition. This not only allowed the fabrication of deeper undercuts and bridge structures for shadow evaporation (Figure 24b), but also reduced the cracking of the AlOx capping layer during the lift-off step. After removing the solvent from the bottom resist, the actual UV resist coating was added by spinning. We used a positive-tone UV resist (AR-P 3540, Allresist GmbH), which is meant to be used with the two-layer resist system. This resist was spun at 1200 RPM to reach a thickness of 2.8 µm and then the sample was baked at 100 °C for 140 s. The small vertical walls, fabricated earlier around the platform, allow the resist to stay on the structure during spinning. These walls would not be needed, if for example direct spray coating was used [103].

The pattern for the SINIS junctions is exposed using the same Nanoscribe Photonic Professional system that was used for the PnC structure fabrication. Since now a traditional solid UV resist was used, the same immersion objective could not be used. Instead, an air-gap objective (63x, NA = 0.75) was used with the mode presented in Section 4.1. The writing was done with the piezo scan mode as for the PnC structure, using the writing parameters shown in Table 3. These parameters produced a single-pass line width of 1 µm on the platform and 1.5 µm on the substrate. However, the actual line widths were larger, since the drawing was done using multiple passes with varying height to guarantee full exposure in z-direction. Multiple passes were used, even though the voxels aspect ratio is naturally high (height:width 5:1), because of possible imperfec-

TABLE 3 The writing parameters used for the SINIS junction patterning with the Photonic Professional system.

Parameter	Value (platform)	Value (ramps)	Value (substrate)
PowerScaling	1.0	1.1	1.0
LaserPower	20 % (4 mW)	100 % (22 mW)	100 % (20 mW)
SettlingTime	200 ms	200 ms	200 ms
ScanSpeed	25 μm/s	25 μm/s	25 μm/s

tions caused by the tilt of the sample and the variations in the height of the PnC structure. These problems remain even with the sample alignment, because the alignment has to be done using the integrated optical microscope with the Photonic Professional. Writing in multiple passes was especially required in areas around the base of the PnC structure, since there the resist is thickest. This thick resist layer around the structure is caused by the spin coating method used for the resist coating.

After the sample was exposed, it was developed using a 1:1 mixture of the developer (AR 300-47 Allresist GmbH) and deionized water. Then the sample was thoroughly rinsed in deionized water. With the two layer resist system used here for the lithography, the undercut depth is controlled simply by changing the development time. This is due to the fact that the laser does not actually expose the bottom resist and it is just slowly dissolved by the developer, giving a controllable undercut. For samples with the baked bottom resist, the development times were around 60 s and for the samples with non-baked bottom resist around 15 s. This development time produced a micron-scale undercut profile in the samples with the non-baked bottom resist (Figure 24b).

When the development was done, the samples were again oxygen cleaned with RIE to remove any possible resist residue in the pattern. Then the metal evaporations were done with an ultra-high vacuum electron-beam evaporator. A 40 nm thick aluminum film was evaporated first along the patterned leads climbing the slopes. The aluminum was evaporated from both sides of the surface normal, using four steps per side, as shown in Table 4. Using a sequence like this ensures better coverage over the roughness of the surface and the steep slopes of the phononic crystal structure. Then the AlOx tunnel barrier is created by thermally oxidizing the aluminum in 200 mbar of pure oxygen for 9 minutes. Then the sample is rotated 90° and 60 nm thick copper leads are evaporated perpendicular to the aluminum leads. This evaporation was done similarly to the aluminum, but using five steps per side as shown in Table 4. The copper was also evaporated from an angle, because no normal metal is wanted on the aluminum leads on top of the structure. The normal metal would provide a way for heat to escape off the platform even at low temperatures. After evaporating the metals, lift-off was done by suspending the sample in hot acetone. The lift-off needs to be done fast so a syringe was used to spray the sample with the acetone while suspended. The spraying has to be done carefully, since the acetone will eventually break the adhesion between the PnC structure and the substrate, removing the whole structure. A finished SINIS junction device on a PnC structure is shown in

Figure 25.

In the end, the biggest problem with the wire fabrication was the cracking of the capping layer mentioned in Section 4.2.3. This cracking was happening during the lift-off or when drying the sample after the lift-off. The deformation of the structures fabricated with 3D lithography during drying is a known issue. This deformation is due to capillary forces caused by the evaporating liquid, which in our case was isopropanol. This issue is often addressed with critical point drying (CPD), where the transition from liquid to gas is avoided by going around the critical point of the liquid. So, I decided to try CPD after the lift-off to possibly reduce the cracking. Since our CPD instrument was setup with CO_2 I could directly use the acetone, which was used in the lift-off, as the intermediate liquid as it is completely miscible in liquid CO_2. However, unexpectedly the CPD process made the cracking issue even worse and there were cracks all over the platform. This suggested that the cracking might get worse if the sample is kept for a longer time in acetone, since this was the case with CPD. Therefore, I decided to do the lift-off as fast as possible, so that the time spent in acetone was as short as possible ($\sim$3 min), and then I dried the sample normally with nitrogen gas. This fast lift-off worked, as I was able to produce samples with no cracks about 70 % of the time.

TABLE 4 The angles with respect to surface normal and the non-angle-corrected thicknesses d, used in the angle evaporation sequence of the SINIS junction devices. The aluminum is oxidized before the evaporation of the copper and the sample is turned 90° around the surface normal, so that the copper wires are evaporated perpendicular to the aluminum.

Angle (°)	***d* Al** (nm)	***d* Cu** (nm)
± 70	10	10
± 68		10
± 66.6	10	
± 65		15
± 63.3	12	
± 63		15
± 60	15	20

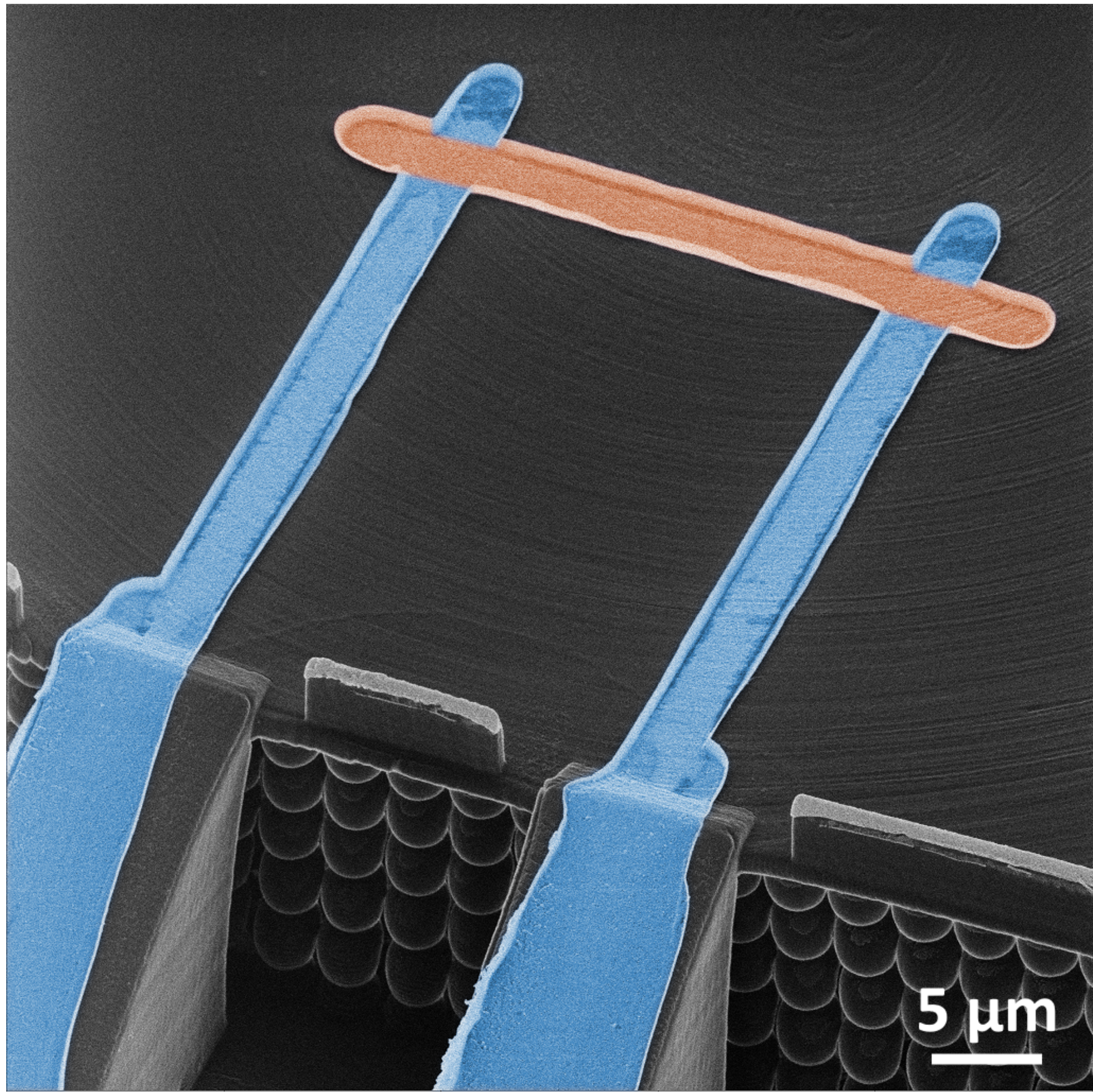

FIGURE 25 A false color helium ion micrograph showing a completed SINIS junction device on a PnC structure (red = Cu, blue = Al). This is a sample fabricated early in the project and thus there is no smoothing on the platform. Here, the line width is about 3 µm on the platform, which gives a 9 μm^2 area for the individual junctions. Reprinted from Reference [**PII**], with permission of AIP Publishing, copyright 2020.

5 MEASUREMENT SETUP

In this study all measurements were done at low temperatures, as all the samples include superconducting tunnel junctions. As the superconductor used in this study was aluminum with a T_C of 1.2 K, temperatures below 1 K are needed. To be able to reach these temperatures a ^{3}He/^{4}He dilution refrigerator was used for the measurements. In our group we use our own in-house built dilution refrigerators. The refrigerator used for most of the measurements in this study is shown in Figure 27. When used, the bottom part (Figure 27b) is covered with a vacuum jacket, and then inserted into a dewar filled with liquid ^{4}He, which works as a 4.2 K bath. The cryostat measurement lines have filtering at three different temperature stages, which are the bath (4.2 K), the pot ($\sim$ 1 K) and the mixing chamber, which is at the same temperature as the sample stage. In addition to these the cryostat also has on-stage RF filtering as shown in Figure 27d.

Every measurement was done with a four probe setup due to the large resistance of the wiring in the dilution refrigerator. The circuit used for the IV characteristic measurements in this study is shown in Figure 26. The same exact setup was used also for measuring the power of the heater when studying the thermal conductance. For measuring the thermometer junction a similar setup was used, but with a battery powered constant current source and no measurement of the current. The voltage preamplifier was an Ithaco 1201 low noise voltage preamplifier and the current preamplifier was an Ithaco model 1211. The voltage source used was a simple sweeping battery box powered by two 12 V car batteries and the voltage over the sample was controlled with different voltage dividers.

5.1 Measurement procedure

The I-V characteristic measurements of NIS tunnel junctions are straightforward, but for the thermal conductance measurements a certain procedure needed to be used. Five days were always reserved for these measurements, the fifth day being a precaution if there were any issues. The first day is used just for cooling the

cryostat down to the pot temperature which is around 1 K. On the next day, the circulation of the ^{3}He/^{4}He mixture is started and the sample is cooled to around 40 mK at the lowest. Then IV characteristic measurements are done for both the SINIS junction pairs on the sample at different bath (stage) temperatures. According to the results of these measurements, the junction with the lower leakage current and better temperature response is chosen to be the thermometer.

Then in the morning of the third day, the junction chosen to be the thermometer is calibrated while cooling the refrigerator down from the pot temperature. This is the first calibration, which we usually do with a low bias current leading to good temperature response at low temperatures while losing sensitivity at higher temperatures. Then the thermal conductance measurements are done by keeping the bath (stage) temperature constant and heating the sample with the other junction. While heating the sample, the current and voltage over the heater is measured to obtain the emitted power. The temperature of the sample is measured from the voltage over the calibrated junction. On the fourth day the same process is followed with a higher bias current, which gives better temperature response at the higher temperatures. At the end, the data measured with both calibrations is combined.

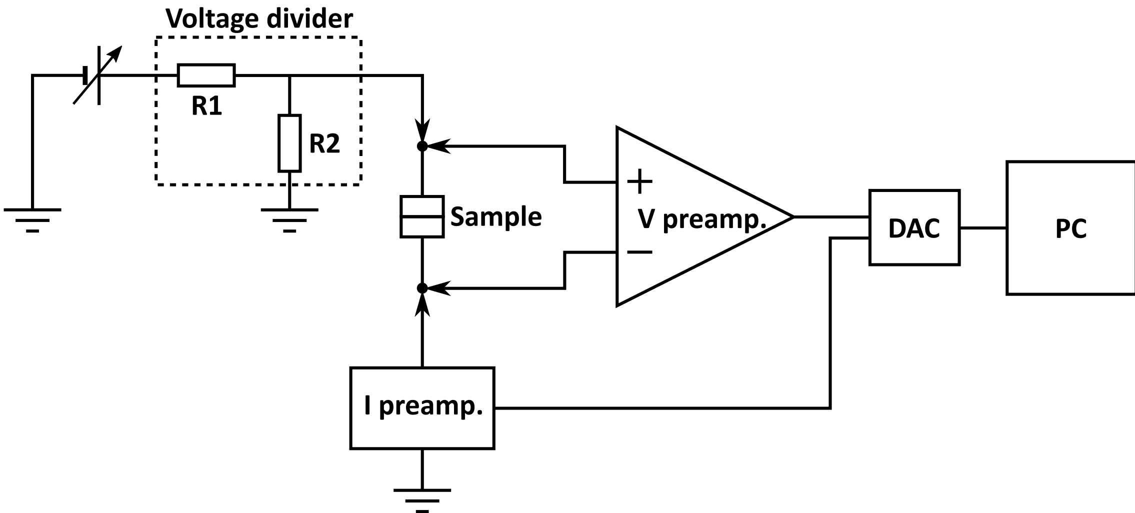

FIGURE 26 A diagram of the circuit used for the IV measurements of junctions. The same circuit was also used for measuring the heating power in the thermal conductance measurements. For the voltage divider, the resistor R1 was varied between 50 kΩ and 100 Ω while R2 was always below 50 Ω. The arrows in the diagram represent the positions of the probes in the measurements.

FIGURE 27 The in-house built $^3He/^4He$ dilution refrigerator. (a) The full cryostat with pump and measurement line connections on the top. (b) A zoomed-in picture of the bottom part, which contains the main functioning parts of the cryostat including the pot, the still and the mixing chamber. (c) A closer view of the mixing chamber and the stage holder. (d) Sample mounted onto the sample stage. The sample connections were made with indium bonding and thus large indium joints are visible

6 MEASUREMENT RESULTS

6.1 NIS junctions on a substrate

This section is based on article PII. After developing the new fabrication method for the junctions with two-photon lithography [**PI**, **PII**], the next step was to prove that this method can produce working NIS junctions. We started by fabricating SINIS junction pairs, because the junctions are simpler to fabricate as pairs and junction pairs are going to be used for the heat transfer measurements on the PnC structures. The samples were fabricated as described in Section 4.3 except on a flat nitridized Si substrate. At this point I was making as small junctions as possible with the new method, so the linewidths were between 1 and 2 μm (1 - 4 μm^2 junction area). Smaller area junctions are usually desired, because there is a smaller possibility of point contacts and the tunneling resistance is higher, which is desired for thermometry.

The I-V characteristics of the samples were measured at low temperatures, which are required for the aluminum to turn superconducting. The samples were cooled in a $^3He/^4He$ dilution refrigerator down to 40 mK at the lowest. The I-V measurements were done with simple DC voltage sweeps using a four probe setup. Low noise voltage and current preamplifiers (ITHACO model 1201 and 1211) were used to measure the voltage and the current as discussed in Section 5. The I-V characteristics were measured at many different bath temperatures, so that the temperature dependency can also be seen.

The results of an example of these kinds of measurements are shown in Figure 28. At first glance looking at the linear scale figures, the data indicates that the sample indeed is a SINIS junction. However, when studying the data more closely, the size of the superconducting gap Δ seems too high. The gap size is easiest to read from the location of the peaks in Figure 28b. The peaks are located at 2Δ for a SINIS junction, which means that the gap size for this sample is 30 μeV. This is 50 % larger than the normal gap size of aluminum, which is ∼20 μeV [109]. Another anomalous feature is the fact that the peaks start to move closer to zero with rising temperature after a certain threshold temperature ($T \sim 500$

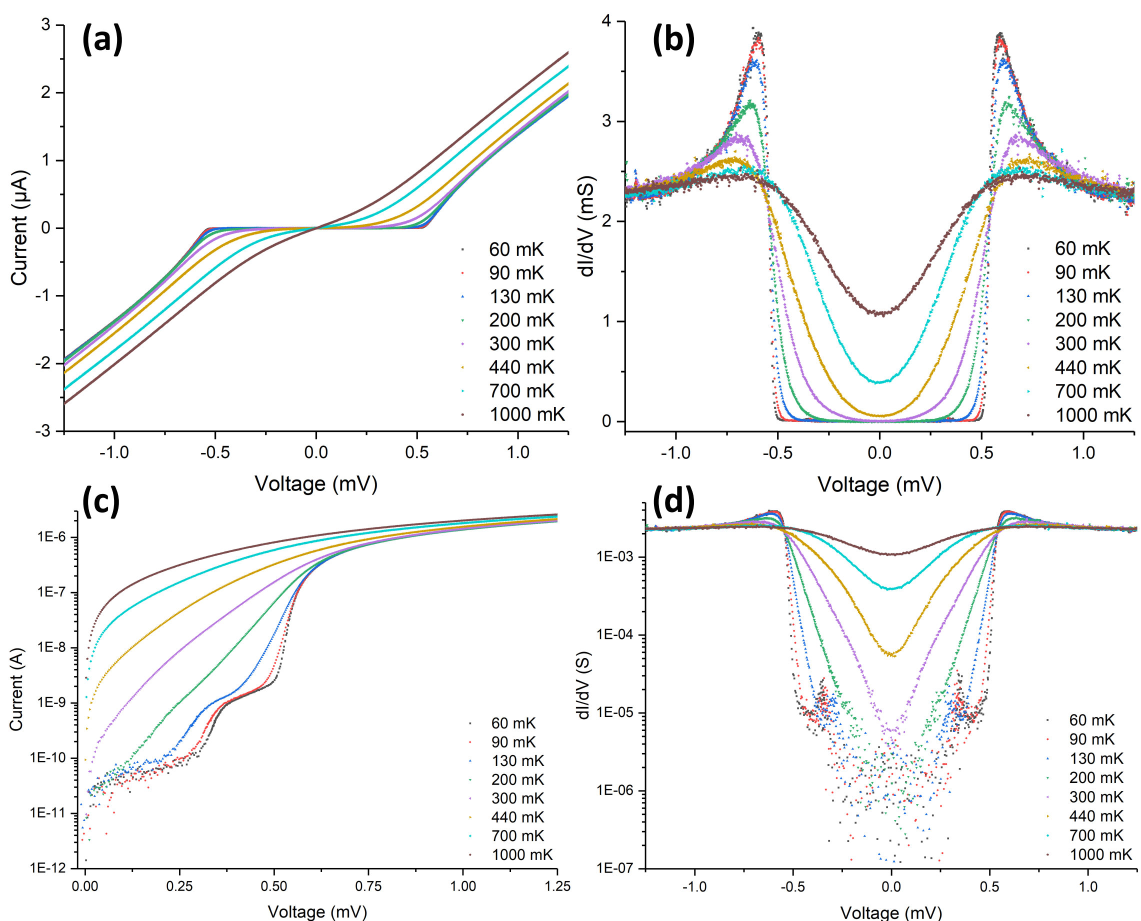

FIGURE 28 Measured low-temperature current-voltage characteristics for a SINIS junction with titanium (8 nm) and gold (60 nm) as the normal metal. (a) Measured IV curves in a linear scale. (b) Calculated differential curves for the SINIS junction. (c) The IV curves in a log scale. (d) The differential curves in a log scale. The measurements were done at different bath temperatures using DC voltage sweeps.

mK). Focusing on the log scale (Figure 28c,d), it is revealed that there actually is a second much smaller gap feature around $V \sim 0.3$ mV.

To further study this effect, we first made similar samples but changed the normal metal from copper to gold. With gold a very thin adhesion layer of titanium is used so the normal metal is actually a TiAu bi-layer (Ti, 8 nm; Au, 60 nm). Changing the normal metal did not change the behaviour. The data in Figure 28 is actually from a sample with gold as the normal metal. We also tried different substrates to see if the substrate surface was causing the double peak. However, the results were similar on sapphire, SiN and the IP-Dip resist.

Since changing the materials did not have an effect, we started making junctions with different junction areas. We also made single NIS junctions to simplify the data analysis and rule out the effects of asymmetry between the two junctions [41]. Another benefit of NIS junctions is that with them, making a large amount of junctions with different sizes is very simple. So I made a sample with a large number of different sized NIS junctions. The measurements showed that all the

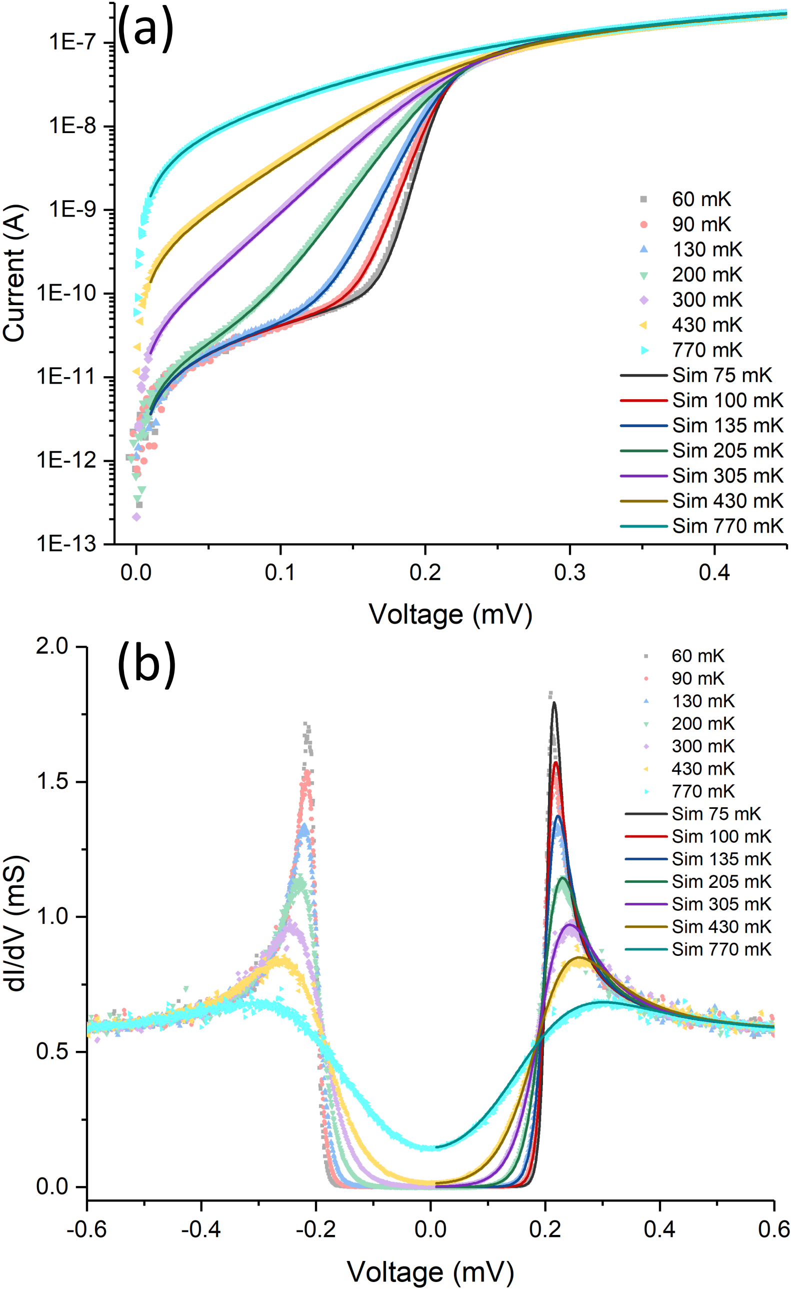

FIGURE 29 The I-V characteristics measured from the NIS junction with a large junction area ($\sim$9 μm^2). The figure also includes theoretical curves computed using the simple BCS theory (Equation 31). Reprinted from Reference **[PII]**, with permission of AIP Publishing, copyright 2020.

smaller junctions had the double peaks with differing resistance ratios. However, the largest junction on the sample (~9μm^2) had only one gap feature. The data from this largest junction is shown in Figure 29 together with theoretical curves.

The theoretical curves were calculated with the simple BCS theory, using Equation 31 at constant temperatures, and they fit the measured data well. The temperatures also match the measured ones almost exactly, except at the lowest temperature where the bath temperature is lower. This effect is well known and it happens due to spurious thermal radiation coming from the hotter parts of the refrigerator, combined with the fact that the electron system is thermally decoupled from the lattice [42, 45, 110]. Using the simulations we found a value of $\Delta(0) = 0.208$ meV for the zero temperature superconducting gap of the Al film, which agrees reasonably with literature [109] and previous results on similar Al films deposited using the same evaporator [42]. We also determined the Dynes parameter for this setup which was $\Gamma/\Delta(0) = 6.5 \times 10^{-4}$. It was determined using the amount of subgap leak current. The value of the Dynes is roughly consistent with earlier measurements in the same setup before [42], and it should be low enough even for NIS coolers [57, 111]. However, we did not observe electronic cooling, because the single junction geometry leads to a very large normal metal electrode, and because there are no normal metal quasiparticle traps on the aluminum electrodes [112].

6.2 What causes the double gap feature?

Some time was spent investigating the "double gap" effect of the NIS junctions, even though this effect was not really a problem for our application. Also it seems that by increasing the junction area produced a normal junction (see Figure 29). This effect was still interesting as it seems to effectively increase the gap size of the superconductor at least in a certain temperature range. The double gap could suggest that there are somehow two different junctions in parallel. Also somehow, the energy gap of one of the junctions would seem enhanced. This could be caused by the gap size of the aluminum actually being larger. A second option is spin splitting, which causes doubling of the $\mathrm{d}I/\mathrm{d}V$ peaks [113]. A third option is series resistance, but in this case somehow the series resistance would need to be different for each parallel junction.

The first thing to study was the T_C of the aluminum, since the gap size is directly proportional to it, as shown in Equation 23. It has been shown that by making a granular aluminum film, the T_C can be significantly increased [114]. So, we wanted to check if it is possible that in these samples the quality of the aluminum could be altered in some spots in the junction area, causing the larger secondary gap. To study the T_C in the junction area, I made samples which were just long aluminum lines (300 μm) covered with AlOx and copper to basically create a huge junction area. The fabrication was done the same way as for the normal NIS junctions in this study. We measured the T_C of two lines on the same

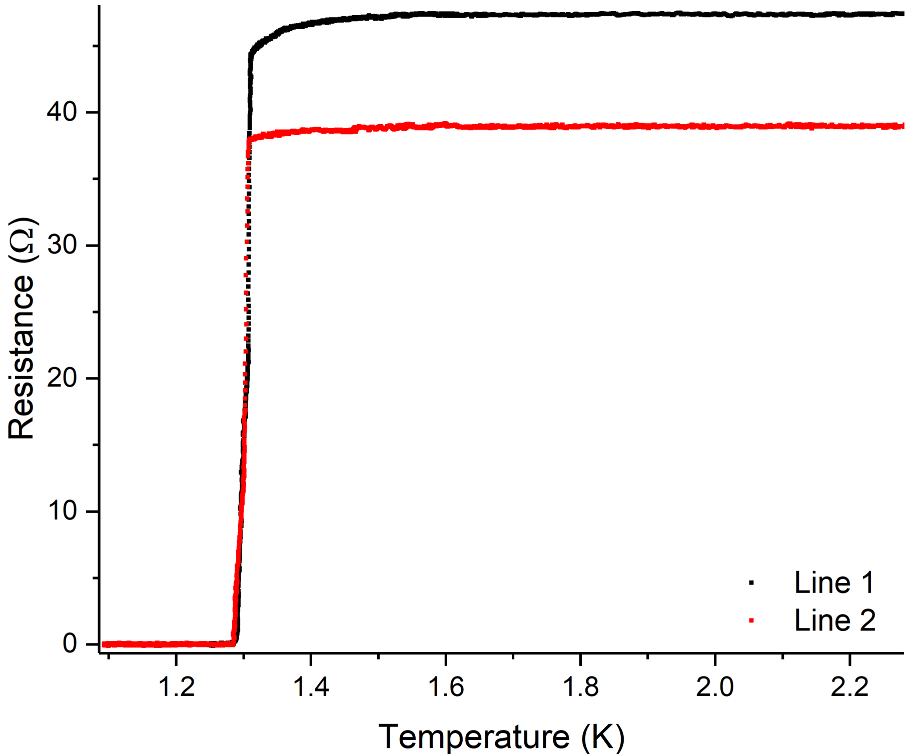

FIGURE 30 T_C measurements of two 300 μm long aluminum lines covered with a layer of AlOx and copper. The lithography for these lines was done with the same procedure as with the usual NIS junctions. The metal film thicknesses were the same 30 nm (Al) and 60 nm (Cu) as for the NIS junctions and similar evaporation sequences were used.

chip, with the results shown in Figure 30. As we see, the resistance drops to zero in a single step at 1.3 K and there are no drops at higher temperatures. So both lines have a very normal T_C of 1.3 K. If there were parts with higher T_C, there would be small drops in the resistance above the 1.3 K temperature. We used an AC setup with two lock-in amplifiers (Stanford Research systems model SR830) for this measurement, as this kind of setup had less noise compared to the DC setup used for the NIS junction measurements.

Since there was no high T_C aluminum on the samples, we also studied whether spin splitting could be the cause. For spin splitting, it is useful to do the measurements in an external magnetic field, because the splitting of the density of states between spin up (↑) and spin down (↓) states can be modified by a magnetic field. The summed density of states in this case is given by the expression

$$N_{\uparrow,\downarrow}(E) = \frac{1}{2}\left|\mathrm{Re}\left(\frac{\epsilon + i\Gamma \pm h_{\mathrm{exc}}}{\sqrt{(\epsilon + i\Gamma \pm h_{\mathrm{exc}})^2 - \Delta^2(T_S)}}\right)\right|, \tag{35}$$

where h_{exc} is the exchange field inside the superconductor [115]. This means that for this phenomenon to introduce the double gap, there needs to be some magnetic material in the junction which introduces this exchange field. This material could be for example some residue left by the new resists which we had not used

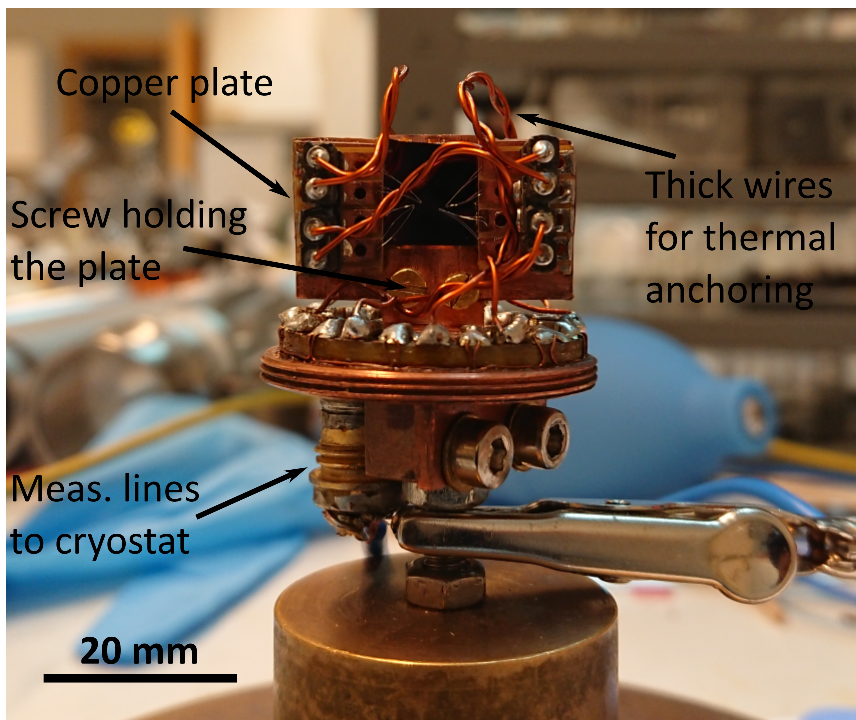

FIGURE 31 The modified stage for measurements with a magnetic field. The sample is first bonded onto the copper plate. Then the plate is connected to the stage with screws and the wiring is connected via pin connectors.

before for junction fabrication. By using an external magnetic field we should then be able to enhance or reduce the splitting by changing the direction and magnitude of the external magnetic field. If the external field is aligned with the internal h_{exc} the splitting is enhanced, and if the external field is opposite to the internal h_{exc} the splitting is reduced.

To do these measurements we needed a cryostat with a superconducting coil to introduce a magnetic field. The coil was wound around the vacuum jacket which covers the bottom part of the cryostat (Figure 27b). The magnetic field also needs to be aligned so that the field lines are parallel to the aluminum films on the sample, otherwise the magnetic field will destroy the superconductivity of the aluminum film. Since the coil will introduce a field aligned with the shaft of the cryostat, the sample needs to stand vertically on the stage. To achieve this, we altered the stage of the cryostat so that the sample can be attached to a vertical copper plate on the stage (Figure 31). Thick wiring was used to contact the pads of the attached plate to the pads on the stage, in order to thermalize the plate better.

For the measurements with the magnetic field we chose NIS samples where the peak heights of the gaps were close to being equal. With a sample like this the behaviour of the density of states is easiest to study, as both peaks can be easily seen. An example of these measurements is shown in Figure 32. The current of the magnet was first ramped in the positive direction, and measurements were done at certain points. Afterwards, the same was done for the negative direction. However, as the results show, at no point does the outer peak position get shifted

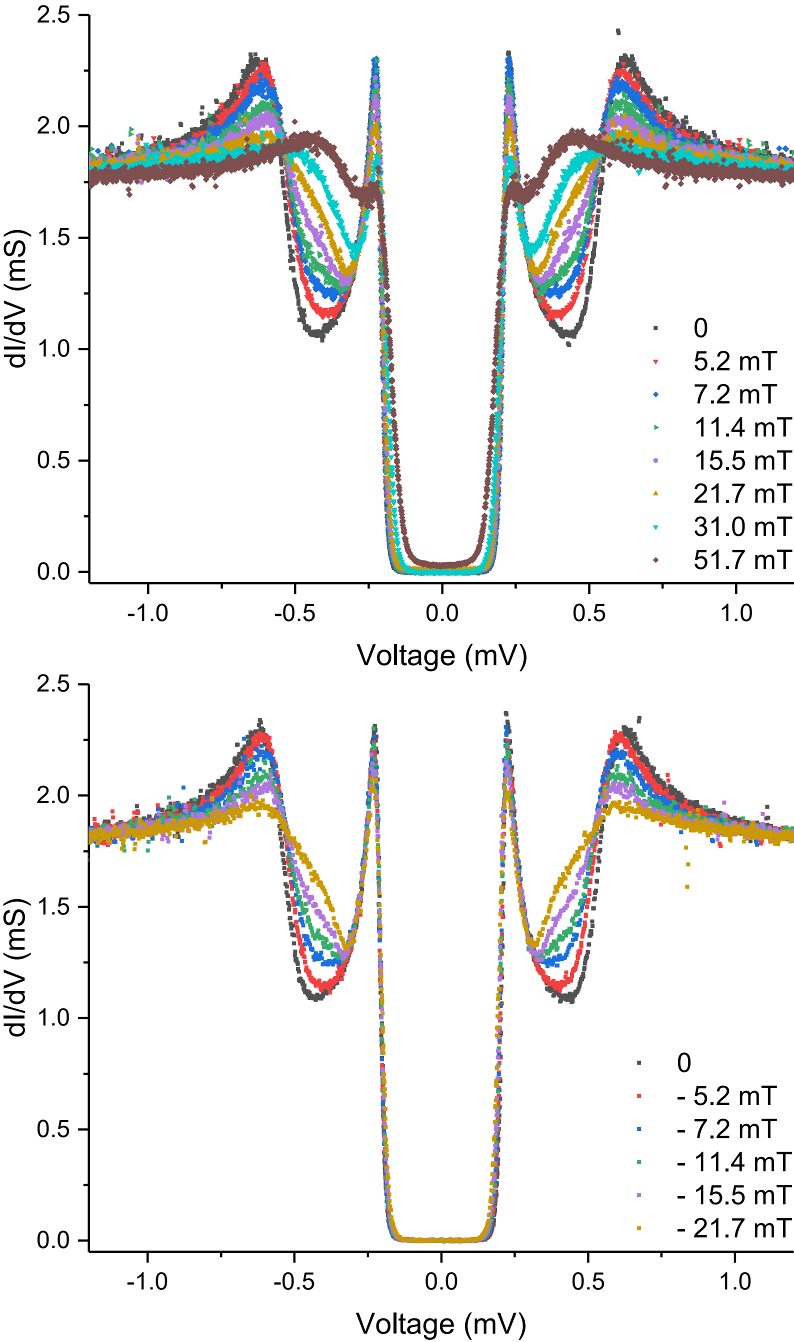

FIGURE 32 The results from the measurements with an external magnetic field for both polarizations. The dI/dV curves were calculated from the measured I-V data. The junction area for this sample was ~6 μm^2

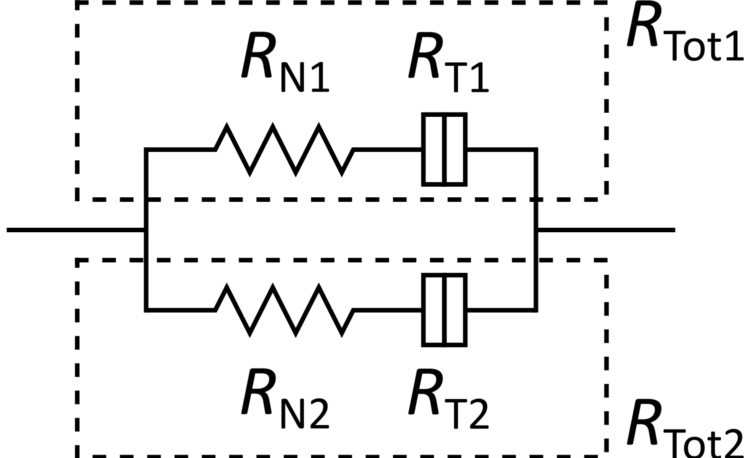

FIGURE 33 A circuit diagram of the parallel junction model with series resistance.

higher which should happen when the h_{exc} is enhanced. Moreover the curves are similar for both polarizations.

Since the spin splitting model did not fit the data, we also studied the third possibility, the series resistance. Because the leads are superconducting and four probe setups were used, the series resistance has to be caused by the normal metal island or lead in the case of NIS junctions. Thus from now on I will refer to this resistance as the normal metal resistance R_N. For this effect to produce the double peaks, there somehow needs to be two channels through the normal metal as the R_N has to be different for the two parallel junctions. The system is depicted in Figure 33. To study this, the same sample used in the magnetic field measurement was measured at different temperatures, and simulations with two parallel junctions were done. The simulations were done with the simple theory like for the data in Figure 29 (Equation 31), just with two parallel junctions having series resistance. The measured data with the simulated curves is shown in Figure 34.

The first thing that is clear from these simulations, is that the inner gap feature corresponds to a completely normal Al-AlOx-Cu junction. As can be seen from Figure 34b, the simulations for the inner peaks follow the data almost perfectly. The gap size was determined to be 0.195 meV and the R_{N1} had a reasonable value of $90\,\Omega$. The total resistance for this junction was determined to be $R_{\mathrm{Tot1}} = 1150\,\Omega$. There is a deviation at bath temperatures 60 mK and 90 mK at low currents in Figure 34a. At first glance it looks like self heating but since similar deviation is not present at 40 mK, this deviation is probably somehow caused by the second junction. The second junction also affects the apparent Dynes parameter, and thus a precise value cannot be given for the individual junctions.

When simulating the junction with the apparent larger gap the fits are not as good any more, as is visible from Figure 34b. With the simple model, there was no way to get the correct peak height just by adjusting the gap size and the R_N. From these simulations we arrived at a gap size of 0.23 meV, which is slightly higher than the other junction but still a completely possible value for aluminum. The correct shape for the peak could probably be produced with a thermal model, but with a model like that there would be too many fitting variables. However,

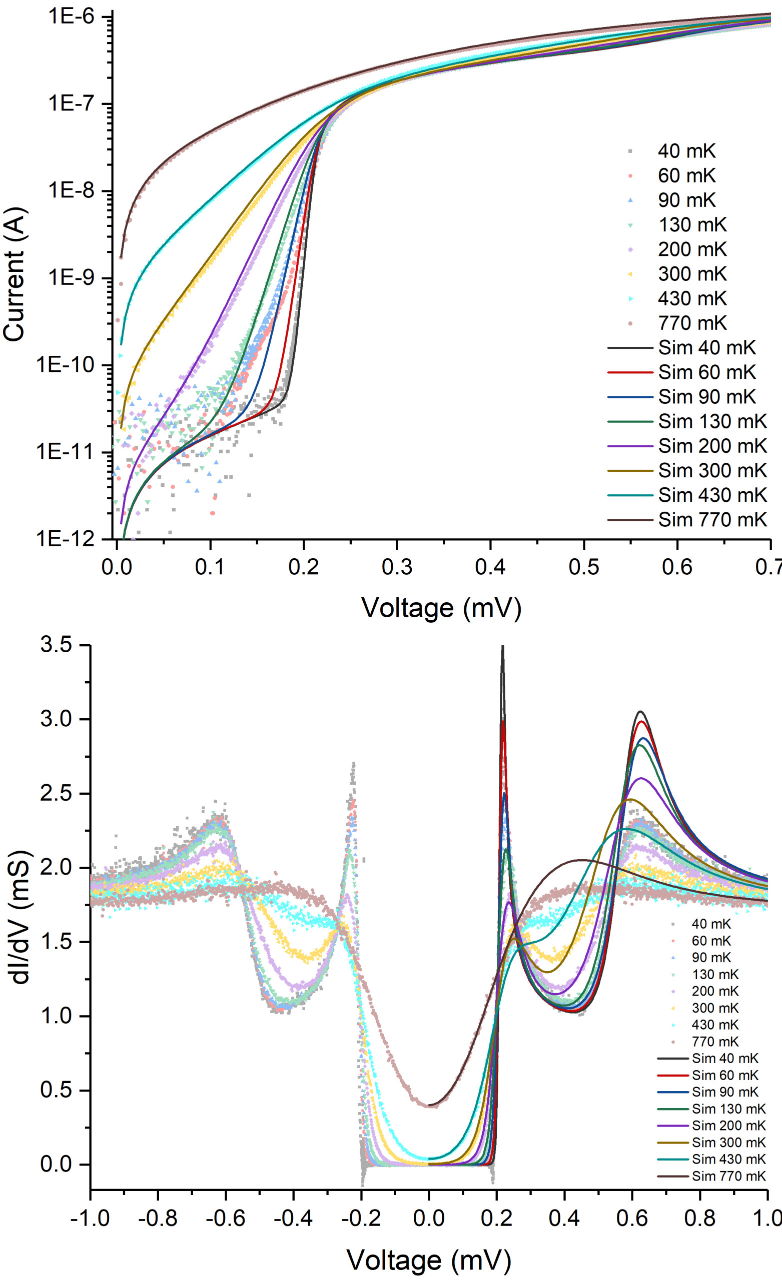

FIGURE 34 NIS junction data measured at different bath temeratures with simulated curves. The simulated curves were calculated with a parallel model using different normal metal resistances for the two junctions. These measurements were done for the same sample as Figure 32 (junction area ~6 μm^2).

this is not even the biggest issue. The biggest problem is the movement of the peak towards the smaller voltage peak as a function of temperature. None of the models used here can easily produce this behaviour. The only way to get the curves in Figure 34b was to assume that the normal metal resistance of the second junction (R_{N2}) is dependent on the temperature. For the simulated curves the R_{N2} changed from 730 Ω at 40 mK to 400 Ω at 770 mK. Already the resistance at 40 mK is too high as the total resistance is $R_{\mathrm{Tot2}} = 1200\,\Omega$, so it would constitute over half of the total resistance. It is possible for the resistance of a metal film to change at low temperatures, but here the resistance would have to almost drop in half when going from 40 mK to 770 mK. Another issue here is the fact that a higher normal metal temperature of 140 mK had to be used for the 40 mK data and the temperature seems to stay constant until the 200 mK bath temperature. At higher temperatures the simulation temperatures matched the bath temperature. In conclusion, this model can produce curves with pretty much the correct shape, but the parameters that had to be used don't seem realistic. From all this, we can say that the parallel model works perfectly for the inner junction, but the second junction with a larger apparent gap cannot be simulated well with such a simple model. At this point, however, we have most confidence on this parallel-series resistance model. The reason for the possible extra series resistance is, however, unclear.

6.3 SINIS junctions on a 3D structure

This section is based on article PII. After showing that NIS junction fabrication was possible with the new technique, the next step was to show that working junctions can also be fabricated on the 3D PnC structure. Because the PnC structures were designed with ramps only at the two opposing edges, only SINIS tunnel junction fabrication was possible. So only SINIS junction pairs were fabricated on the structures. This design choice was made because we want junction pairs for thermometry and heating of the sample, and we wanted as few ramps as possible to reduce heat flow through them. This is the reason why there is only data from SINIS junction pairs on the 3D structures.

The measurements were done exactly the same way as with the junctions on the substrate. The results of the measurements were also very similar. Many of the SINIS junction pairs had the double gap issue but also normal junctions were produced. Data measured from one of the normal looking samples is shown in Figure 35. Now, the fits done using the simple constant temperature model used before no longer produce such good results. However, by taking into account thermal effects such as junction self-heating or cooling and the normal metal island's thermal resistance caused by the electron-phonon interaction [40, 41], the simulated curves fit the data almost perfectly. The effect of this kind of self-heating is most easily detected as the broadening of the conductance peaks of the low temperature data in the differential graph (Figure 35).

For the simulations with the thermal model, one needs to take into account the heat flows through the junctions. The heat current $\dot{Q}_i$ through each junction $(i = L, R)$ is given by the following expressions [41]:

$$\begin{aligned}\dot{Q}_L(V_L, T_N, T_S) =& \frac{1}{e^2 R_L} \int_{-\infty}^{\infty} d\epsilon (\epsilon + eV_L) N_S(\epsilon, T_S) \\ & \times [f_S(\epsilon, T_S) - f_N(\epsilon + eV_L, T_N)],\end{aligned} \tag{36}$$

$$\begin{aligned}\dot{Q}_R(V_R, T_N, T_S) =& \frac{1}{e^2 R_R} \int_{-\infty}^{\infty} d\epsilon (\epsilon) N_S(\epsilon + eV_R, T_S) \\ & \times [f_N(\epsilon, T_N) - f_S(\epsilon + eV_R, T_S)].\end{aligned} \tag{37}$$

Knowing the heat currents, the total heat power extracted from the normal metal or cooling power P_T can be calculated from

$$P_T = -\dot{Q}_L + \dot{Q}_R. \tag{38}$$

The signs are set so in the above that positive values of P_T correspond to cooling. In dynamic equilibrium the cooling (heating) by the junction is balanced by the inflow (outflow) of heat from (to) the surroundings, which leads to the expression

$$P_T = B(T_{bath}^n - T_N^n) + \beta[P_T + I(V_L + V_R)] + I^2 R_N. \tag{39}$$

The first term gives the direct heating or cooling coming from the substrate (T_{bath}) and the exponent n in the term depends on the disorder level and phonon dimensionality of the sample [116], but is usually $n = 5$. The parameter B includes the normal metal volume V_N and also the electron-phonon coupling strength Σ as $B = \Sigma V_N$. The second term describes the heat flowing back from the superconducting electrodes and it contains the parameter β, which is the fraction of the dissipated power flowing back from the aluminum leads [117]. The third term describes the Joule heating of the normal metal.

In the thermal model we used the usual exponent $n = 5$ which should be the case for power flowing between phonons and electrons for a thick metal film on a bulky substrate [110]. For the parameter B we used a normal value of $\Sigma = 2 \times 10^9$ W/(K^{5}m^3) for the electron-phonon coupling strength in copper [40]. For the fraction of back-flow β we used the value 0.25 which is higher than the values that are usually observed ($\beta < 0.1$) for NIS junction devices optimized for cooling [42, 61]. However, this is expected as in these samples there is no quasiparticle trapping layer on the superconducting films.

The value of the Dynes parameter for this SINIS junction pair is pretty low $\Gamma/\Delta(0) = 9 \times 10^{-5}$. This value is a lot lower than what we found for the sample with a single NIS junction. This enhancement is probably caused by the higher value of the tunneling resistance R_T, which leads to less efficient absorption of environmental radiation power, and thus to a smaller photon-assisted tunneling current. Another possible explanation for the low Dynes parameter is Andreev reflection. However, we estimated the effect of second order Andreev tunneling

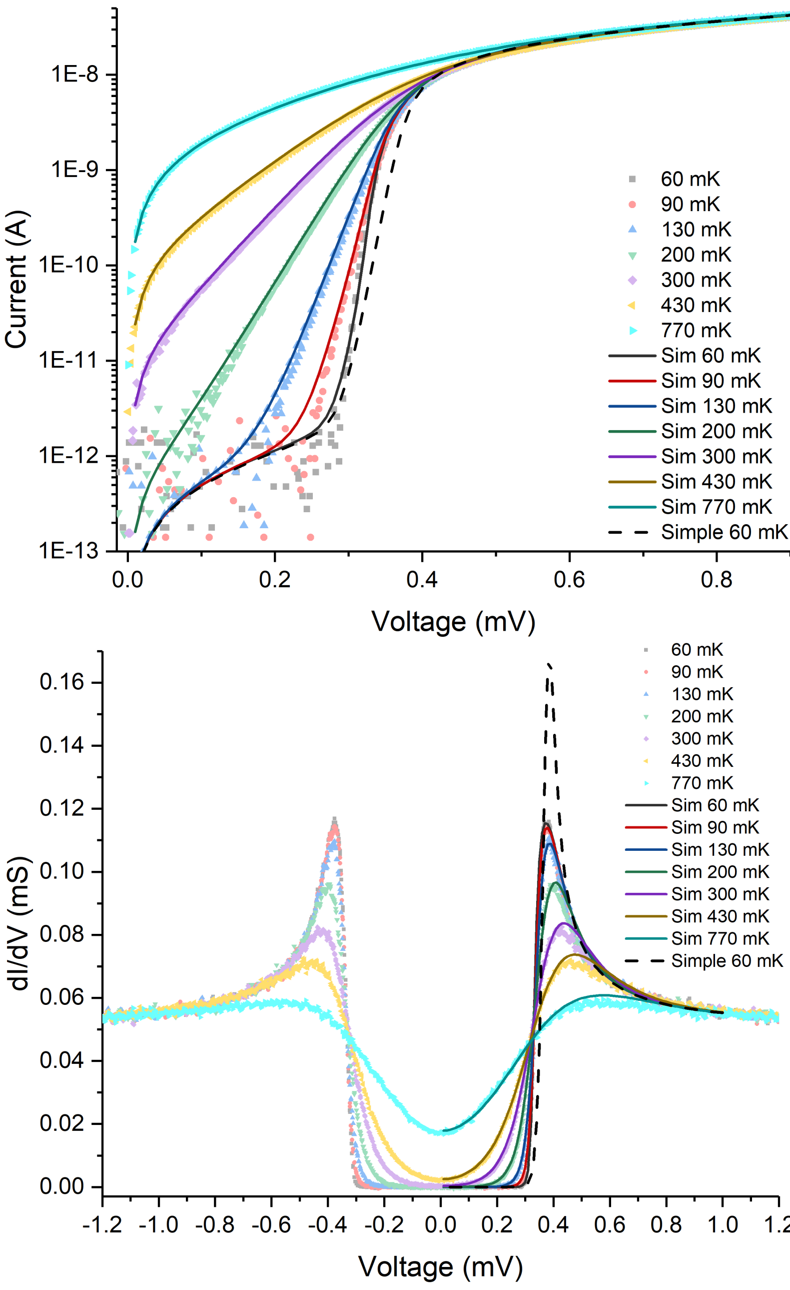

FIGURE 35 The measured I-V characteristics of a SINIS junction pair on a PnC structure. The figure also includes simulated curves made with the thermal model. The result from the simple model simulations is shown for the lowest temperature (dashed line). Reprinted from Reference **[PII]**, with permission of AIP Publishing, copyright 2020.

to not be large enough to cause the sub-gap leak current for these junctions and material parameters [118, 119]. Unexpectedly, even though we were using the same oxidation process, the tunneling resistance was consistently higher for the NIS junctions fabricated on the 3D structures. This might be due to the higher surface roughness or the different substrate material, but we are currently lacking a detailed understanding. The superconducting gap for this junction pair is $\Delta(0) = 0.181$ meV, which is smaller compared to the gap of the NIS junction in the previous section but still in decent agreement with the literature [109].

6.4 Thermal conductance of the PnC structures

This section is based on article PIII. Since we had shown that good quality SINIS junctions can be fabricated also on 3D structures, we were able to move forward to measuring the thermal conductance of the fabricated PnC structures. These measurements were made for the two optimized PnC structures with spheres of diameter 3.1 µm and 5.0 µm, and for a control bulk structure with the same geometry. The measurements were done using the same equipment as the earlier measurements using the procedure shown in Section 5.1. For these measurements at least one of the SINIS junction pairs needs to be working well, because only a working NIS junction has good temperature dependence at the temperatures used. The heater does not necessarily need to be a working tunnel junction as was the case for some of the measurements.

The results of the thermal conductance measurements are shown in Figure 37 together with simulations done with two different models. The data is presented as the heating power of the heater as a function of the temperature given by the SINIS thermometer. In this way the power law for each structure is directly visible in the log-log plot. In Figure 37a the measured data is compared to theoretical curves based on the ballistic simulations made with FEM as described in Section 2.2.4. Adding the suspended membrane to the PnC samples altered the system discussed in Section 2.2.3 a little. Now we had to take into account the thermal conductance of the film as shown in Figure 36. There is also Kapitza resistance between the film and the PnC but it was considered to be zero for the curves in Figure 37a. To find the thermal conductance of the PnC we first have to determine the temperature at the interface between the film and the PnC (T_x). Then we can consider the film to be a large area heater for the PnC

FIGURE 36 A circuit diagram of the thermal conductances in the PnC samples with a suspended membrane.

as its thermal conductance is higher than the thermal conductance of the PnC. The thermal conductance of the film is high because at the used thickness of 1.6 μm it shows bulk behaviour. This can be shown by finding the 2D-3D crossover thickness for the material $d_C = \hbar c_t/(2k_B T)$ [31]. The transverse speed of sound c_t can be calculated with the material parameters in Table 1 using the equation

$$c_t = \sqrt{\frac{\mu}{\rho}} = \sqrt{\frac{E}{2(1+\nu)\rho}} \text{ [32].} \tag{40}$$

This consideration gives us the value $d_C = 33.4$ nm for the 2D-3D crossover at 0.1 K which is substantially smaller than 1.6 μm.

By considering the film as a heater we can find the interface temperature T_x by equating the emitted power of the actual SINIS heater on the film to the emitted power of the film which goes into the PnC below. The emitted power of the film can be calculated as discussed in Section 2.2.3. The emitted power of the SINIS heater on the film can be calculated similarly but FEM simulations are not required. The dispersion relations for a film can be found easily using Lamb-mode theory [120, 121]. At this point we had the emitted power $P(T)$ curves per unit length (heater) and per unit area (film). We made two-parameter fits to these curves using equations of the form $a(T^n - T^n_{\text{bath}})$. Adding the real length of the heater L and the interface area A to the fits we can find values for T_x by setting

$$P_{\text{film}} = P_{\text{heater}} \Rightarrow Aa(T_x^n - T^n_{\text{bath}}) = 2Lb(T^m - T_x^m). \tag{41}$$

In the case of the bulk sample the interface area is considerably smaller as there is no large interface on top of the bulk, instead the film transitions to bulk at the edge of the suspended area. So for the bulk sample the interface area is the thickness of the film multiplied by the length of the edge of the suspended area. The values for T_x in the different cases are shown in Figure 38. The fact that the values for T_x are close to the temperature on the film further proves that the film is not the limiting part. Using the T_x values with either side of Equation 41 gives the theoretical curves in Figure 37a.

The simulations in Figure 37b were done with a simpler diffusive model using Fourier's law (Equation 2). For these simulations we used the thermal conductance (κ) of polymethyl methacrylate (PMMA) since, due to wider use, there is good data available for it. In this case we used the expression $\kappa(T) = 2.9 \times 10^{-2}[\text{W/mK}](T/\text{K})^{1.77}$ [122]. Due to the similarity of PMMA and the IP-Dip resist, this expression is good enough for the purposes of the diffusive model simulations as the point is to show that with this model there will be almost no difference in the thermal conductances of the structures.

The fact that the measurements show a difference between all three structures tells us that we are clearly controlling the thermal transport through the material. This control is strong, as thermal conductance varied for more than an order of magnitude between the PnC and the bulk. However, we were not expecting the thermal conductance of the PnC structures to be higher than the conductance of the bulk as observed in the data. This is very unexpected. We were

expecting that the PnC's would reduce the thermal conductance as is shown by the ballistic simulations in Figures 3 and 37a. It is certain that the transport is at the least partly ballistic as the diffusive simulations show almost no difference between the different structures (Figure 37b), and our measurements show a large difference even between the two PnC structures. The fact that the ballistic simulation for the bulk fits the data very well shows that the transport through the suspended film is entirely ballistic. However, except for their respective order, the PnC structures do not follow the magnitude of the ballistic model. Also the temperature dependence is very different as for the measured data $P \sim T^{4.46}$ and for the simulations $P \sim T^{2.76}$ and $P \sim T^{2.87}$. These differences could be caused by Kapitza resistance. There could be a large difference in the Kapitza resistances, as in the PnC samples there is a large interface between the crystal and the film, and in the bulk structure the film directly transitions into bulk at the edge of the suspended part of the film.

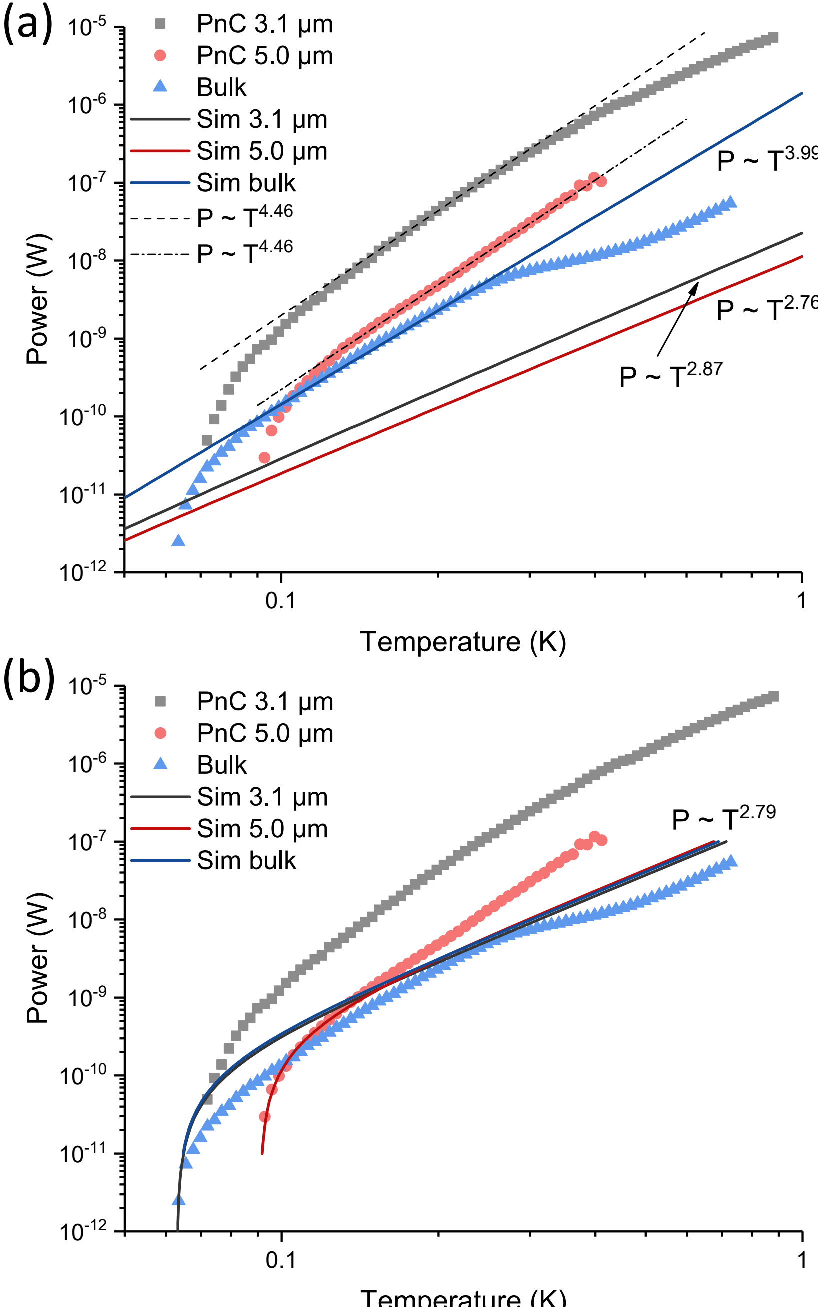

FIGURE 37 The measured heating power of the heater as a function of the temperature on the film. (a) The measured data compared to results from FEM simulations made with a ballistic model. (b) The measured data compared to results from simulations made with a diffusive model. The dip in the bulk data at high temperatures is caused by a non-ideality in the junction behaviour of the thermometer at high temperatures.[**PIII**]

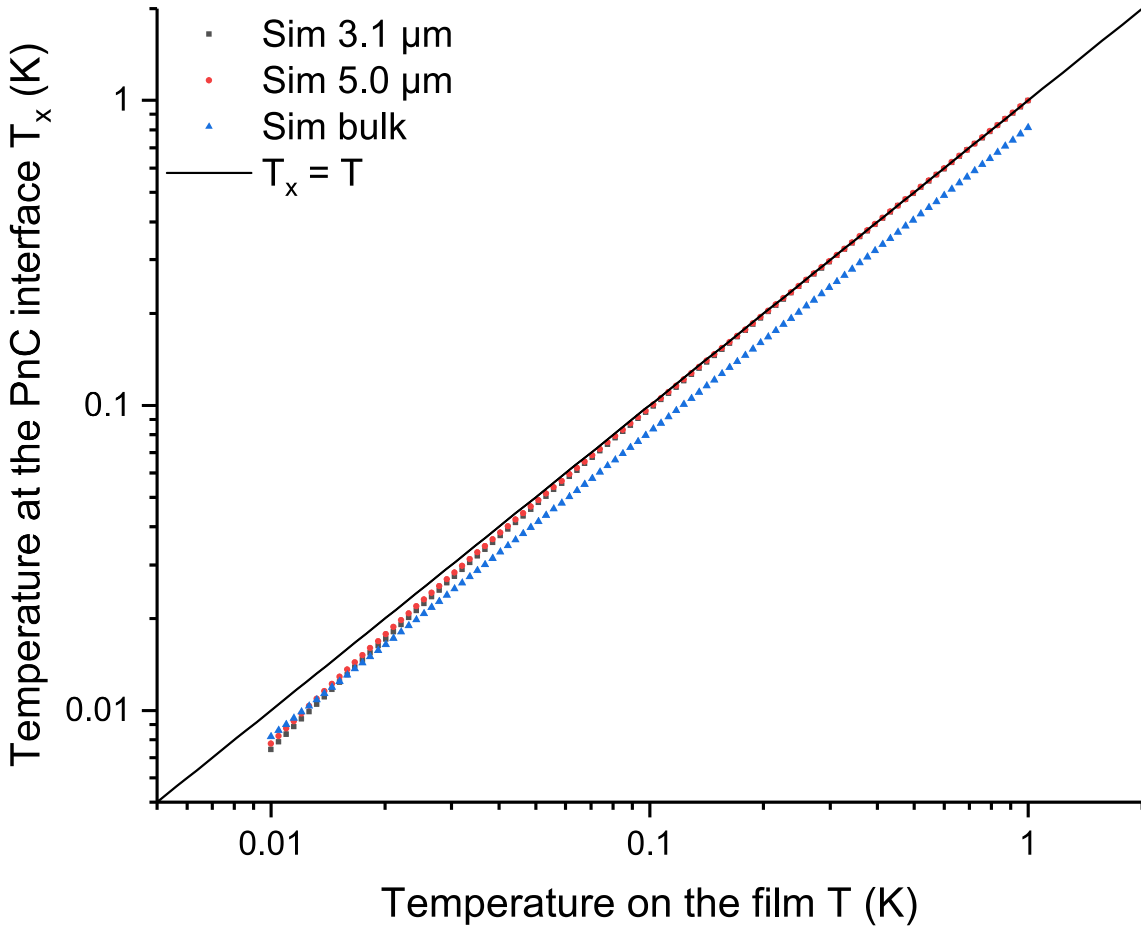

FIGURE 38 The calculated temperature at the interface between the film and the PnC as a function of the heater temperature.

7 CONCLUSIONS

As controlling thermal transport becomes more and more important, the need for better PnC structures will grow, and I am sure that the versatility provided by 3D PnC structures will increase interest in them. This thesis clearly shows that 3D lithography is a viable way to produce 3D PnC structures, without the limitations of the previous methods such as colloidal crystallization. Colloidal crystallization for example relies on self-assembly, and thus the lattice type can not be freely chosen. With 3D lithography the only limitations are the usable material and the $\sim$200 nm resolution of laser 3D lithography devices. Here we used lattices of spheres but with this method it is possible to fabricate a very wide variety of crystals.

In the second part of the thesis we developed a method for fabricating metallic and superconducting devices on large topographies, which utilizes the same 3D lithography system that was used for the PnC fabrication. We show that this method can produce good quality NIS junction devices on flat substrates and at least on our simple 3D structures. Due to the capabilities of 3D lithography, fabrication on even more complex structures should be possible. In this thesis only NIS junctions were fabricated, but due to the use of established lift-off techniques the fabrication of a wide variety of devices is possible. With this method we also found the interesting phenomenon, where the fabricated junctions were showing a "double gap" feature. We can't yet fully explain this phenomenon, but the parallel model with a series resistance seems most promising as it produced results similar to the measurements. More research into this phenomenon is required to fully understand it. One way to further study this effect is to fabricate similar junctions with electron beam and UV lithography and see if the results are similar.

The last part of the thesis focuses on the thermal conductivity measurements of the samples fabricated with the developed method. Even though the measurement results for the PnC structures don't match the ballistic FEM simulations, it is still most likely that we are controlling the thermal conductance via coherently modifying the phononic band structure of the material. First of all, the ballistic picture seems to be able to explain the bulk IP-Dip results really well. In addi-

tion, classically there should be no difference between the two PnC structures as they have the same filling factor. Moreover, according to our simulations if the transport was diffusive there wouldn't be a difference even between the bulk and the PnC structures as the suspended membrane would dominate. The crystals shown here can only enhance thermal conductivity at temperatures higher than 60 mK, but this is most likely due to the used geometry and different geometries should allow better control of thermal conductance in both directions. To find these geometries the interface effects between a membrane and a PnC have to be studied first as fabrication of NIS junctions directly on the spheres is not possible.

Even though the structures shown here don't follow the simplified theoretical calculations, this thesis clearly shows that the methods shown here can be used for the fabrication and study of 3D PnC structures. At the least this thesis can work as a good basis for further study into the matter, as these methods should allow the fabrication of a wide variety of PnC structures. Due to the versatility of 3D lithography, the crystal lattice could easily be changed from simple cubic to FCC. The FCC samples could then be directly compared to 3D PnC structures fabricated with colloidal crystallization as the polystyrene spheres used by our group form an FCC lattice.

BIBLIOGRAPHY

1. Kushwaha, M. S., Halevi, P., Dobrzynski, L. & Djafari-Rouhani, B. Acoustic band structure of periodic elastic composites. *Phys. Rev. Lett.* **71,** 2022–2025 (13 1993).
2. Sigalas, M. & Economou, E. Band structure of elastic waves in two dimensional systems. *Solid State Communications* **86,** 141 –143 (1993).
3. Pennec, Y., Vasseur, J. O., Djafari-Rouhani, B., Dobrzyński, L. & Deymier, P. A. Two-dimensional phononic crystals: Examples and applications. *Surface Science Reports* **65,** 229–291 (2010).
4. Sledzinska, M. *et al.* 2D Phononic Crystals: Progress and Prospects in Hypersound and Thermal Transport Engineering. *Advanced Functional Materials* **30,** 1904434 (2020).
5. Yang, S. *et al.* Focusing of Sound in a 3D Phononic Crystal. *Phys. Rev. Lett.* **93,** 024301 (2 2004).
6. Tol, S, Degertekin, F. & Erturk, A. 3D-printed phononic crystal lens for elastic wave focusing and energy harvesting. *Additive Manufacturing* **29,** 100780 (2019).
7. Gorishnyy, T., Ullal, C. K., Maldovan, M., Fytas, G. & Thomas, E. L. Hypersonic Phononic Crystals. *Phys. Rev. Lett.* **94,** 115501 (11 2005).
8. Cheng, W., Wang, J., Jonas, U., Fytas, G. & Stefanou, N. Observation and tuning of hypersonic bandgaps in colloidal crystals. *Nature materials* **5,** 830–836 (2006).
9. Olsson III, R. H. & El-Kady, I. Microfabricated phononic crystal devices and applications. *Measurement science and technology* **20,** 012002 (2008).
10. D'Alessandro, L., Belloni, E., Ardito, R., Corigliano, A. & Braghin, F. Modeling and experimental verification of an ultra-wide bandgap in 3D phononic crystal. *Applied Physics Letters* **109,** 221907 (2016).
11. Maldovan, M. Phonon wave interference and thermal bandgap materials. *Nature materials* **14,** 667–674 (2015).
12. Zen, N., Puurtinen, T. A., Isotalo, T. J., Chaudhuri, S. & Maasilta, I. J. Engineering thermal conductance using a two-dimensional phononic crystal. *Nature Communications* **5** (2014).
13. Tian, Y., Puurtinen, T. A., Geng, Z. & Maasilta, I. J. Minimizing Coherent Thermal Conductance by Controlling the Periodicity of Two-Dimensional Phononic Crystals. *Physical Review Applied* **12** (2019).
14. Chen, W. *et al.* Achieving minimal heat conductivity by ballistic confinement in phononic metalattices. *ACS nano* **14,** 4235–4243 (2020).
15. Wei, J. *et al.* Ultrasensitive hot-electron nanobolometers for terahertz astrophysics. *Nature nanotechnology* **3,** 496–500 (2008).

16. Bolgar, A. N. *et al.* A phononic crystal coupled to a transmission line via an artificial atom. *Communications Physics* **3,** 1–6 (2020).
17. Kim, W. *et al.* Thermal conductivity reduction and thermoelectric figure of merit increase by embedding nanoparticles in crystalline semiconductors. *Physical review letters* **96,** 045901 (2006).
18. Cahill, D. G. *et al.* Nanoscale thermal transport. II. 2003-2012. *Applied Physics Reviews* **1,** 011305 (2014).
19. Lee, B. S. & Lee, J. S. Thermal conductivity reduction in graphene with silicon impurity. *Applied Physics A* **121,** 1193–1202 (2015).
20. Yu, J.-K., Mitrovic, S., Tham, D., Varghese, J. & Heath, J. R. Reduction of thermal conductivity in phononic nanomesh structures. *Nature nanotechnology* **5,** 718–721 (2010).
21. Hopkins, P. E. *et al.* Reduction in the thermal conductivity of single crystalline silicon by phononic crystal patterning. *Nano letters* **11,** 107–112 (2011).
22. Anufriev, R., Maire, J. & Nomura, M. Reduction of thermal conductivity by surface scattering of phonons in periodic silicon nanostructures. *Physical Review B* **93,** 045411 (2016).
23. Jiang, P., Bertone, J. F., Hwang, K. S. & Colvin, V. L. Single-Crystal Colloidal Multilayers of Controlled Thickness. *Chem. Mater.* **11,** 2132 (1999).
24. Isotalo, T. J., Tian, Y. L. & Maasilta, I. J. Fabrication and Modelling of Three-Dimensional Sub-kelvin Phononic Crystals. *Journal of Physics: Conference Series* **400,** 052007 (2012).
25. Isotalo, T. J., Tian, Y., Konttinen, M. P. & Maasilta, I. J. Statistical characterization of self-assembled colloidal crystals by single-step vertical deposition. *Colloids and Surfaces A: Physicochemical and Engineering Aspects* **443** (2014).
26. Kittel, C. & Kroemer, H. *Thermal physics* (Wiley New York, 1970).
27. Wolfe, J. P. *Imaging Phonons: Acoustic Wave Propagation in Solids* (Cambridge University Press, 1998).
28. Puurtinen, T. A. & Maasilta, I. J. Low temperature heat capacity of phononic crystal membranes. *AIP Advances* **6,** 121902 (2016).
29. Maasilta, I. J., Puurtinen, T. A., Tian, Y. & Geng, Z. Phononic Thermal Conduction Engineering for Bolometers: From Phononic Crystals to Radial Casimir Limit. *Journal of Low Temperature Physics* **184,** 211–216 (2016).
30. Puurtinen, T. A. & Maasilta, I. J. Low-Temperature Coherent Thermal Conduction in Thin Phononic Crystal Membranes. *Crystals* **6,** 72 (2016).
31. Kühn, T & Maasilta, I. J. Maximizing phonon thermal conductance for ballistic membranes. *Journal of Physics: Conference Series* **92,** 012082 (2007).
32. Slaughter, W. S. *The linearized theory of elasticity* (Springer Science & Business Media, 2012).

33. Lemma, E. D. *et al.* Mechanical properties tunability of three-dimensional polymeric structures in two-photon lithography. *IEEE transactions on nanotechnology* **16,** 23–31 (2016).

34. de Bruyn Ouboter, R. Heike Kamerlingh Onnes's Discovery of Superconductivity. *Scientific American* **276,** 98–103 (1997).

35. Meissner, W. & Ochsenfeld, R. Ein neuer Effekt bei Eintritt der Supraleitfähigkeit. *Naturwissenschaften* **21,** 787–788 (1933).

36. Bardeen, J., Cooper, L. N. & Schrieffer, J. R. Theory of Superconductivity. *Phys. Rev.* **108,** 1175–1204 (5 1957).

37. Tinkham, M. *Introduction to Superconductivity* (Dover Publications, 2004).

38. Van Duzer, T. & Turner, C. *Principles of Superconductive Devices and Circuits* (Prentice Hall, 1999).

39. Fisher, J. C. & Giaever, I. Tunneling Through Thin Insulating Layers. *Journal of Applied Physics* **32,** 172–177 (1961).

40. Giazotto, F., Heikkilä, T. T., Luukanen, A., Savin, A. M. & Pekola, J. P. Opportunities for mesoscopics in thermometry and refrigeration: Physics and applications. *Rev. Mod. Phys.* **78,** 217–274 (1 2006).

41. Chaudhuri, S. & Maasilta, I. J. Cooling, conductance, and thermometric performance of non-ideal normal metal-superconductor tunnel junction pairs. *Phys. Rev. B* **85,** 014519 (1 2012).

42. Koppinen, P. J. & Maasilta, I. J. Phonon Cooling of Nanomechanical Beams with Tunnel Junctions. *Phys. Rev. Lett.* **102,** 165502 (16 2009).

43. Feshchenko, A. V. *et al.* Tunnel-Junction Thermometry Down to Millikelvin Temperatures. *Phys. Rev. Applied* **4,** 034001 (3 2015).

44. Meschke, M., Guichard, W. & Pekola, J. P. Single-mode heat conduction by photons. *Nature (London)* **444,** 187–190 (2006).

45. Karvonen, J. T. & Maasilta, I. J. Influence of Phonon Dimensionality on Electron Energy Relaxation. *Phys. Rev. Lett.* **99,** 145503 (14 2007).

46. Schmidt, D. R. *et al.* A superconductor-insulator-normal metal bolometer with microwave readout suitable for large-format arrays. *Applied Physics Letters* **86** (2005).

47. Gasparinetti, S. *et al.* Fast Electron Thermometry for Ultrasensitive Calorimetric Detection. *Phys. Rev. Applied* **3,** 014007 (1 2015).

48. Nahum, M. & Martinis, J. M. Ultrasensitive-hot-electron microbolometer. *Applied Physics Letters* **63,** 3075–3077 (1993).

49. Nahum, M. & Martinis, J. M. Hot-electron microcalorimeters as high-resolution x-ray detectors. *Applied Physics Letters* **66,** 3203–3205 (1995).

50. Heikkilä, T. T. *et al.* Thermoelectric Radiation Detector Based on Superconductor-Ferromagnet Systems. *Phys. Rev. Applied* **10,** 034053 (3 2018).

51. Kuzmin, L. *et al.* Photon-noise-limited cold-electron bolometer based on strong electron self-cooling for high-performance cosmology missions. *Communications Physics* **2,** 104 (2019).
52. Nevala, M. R., Chaudhuri, S., Halkosaari, J., Karvonen, J. T. & Maasilta, I. J. Sub-micron normal-metal/insulator/superconductor tunnel junction thermometer and cooler using Nb. *Applied Physics Letters"* **101** (2012).
53. Julin, J. K. & Maasilta, I. J. Applications and non-idealities of submicron Al-AlOx-Nb tunnel junctions. *Superconductor Science and Technology* **29,** 105003 (2016).
54. Chaudhuri, S., Nevala, M. R. & Maasilta, I. J. Niobium nitride-based normal metal-insulator-superconductor tunnel junction microthermometer. *Applied Physics Letters* **102** (2013).
55. Torgovkin, A., Chaudhuri, S., Malm, J., Sajavaara, T. & Maasilta, I. J. Normal-Metal-Insulator-Superconductor Tunnel Junction With Atomic-Layer-Deposited Titanium Nitride as Superconductor. *IEEE Trans. Appl. Supercond.* **25,** 1101604 (2015).
56. Torgovkin, A., Ruhtinas, A. & Maasilta, I. J. Normal Metal-Insulator-Superconductor Tunnel Junctions With Pulsed Laser Deposited Titanium Nitride as Superconductor. *IEEE Transactions on Applied Superconductivity* **31,** 1–4 (2021).
57. Chaudhuri, S. & Maasilta, I. J. Superconducting tantalum nitride-based normal metal-insulator-superconductor tunnel junctions. *Applied Physics Letters* **104** (2014).
58. Pekola, J. P. *et al.* Hybrid single-electron transistor as a source of quantized electric current. *Nat. Phys.* **4,** 120–124 (2008).
59. Pekola, J. P. *et al.* Single-electron current sources: Toward a refined definition of the ampere. *Rev. Mod. Phys.* **85,** 1421–1472 (4 2013).
60. Nahum, M., Eiles, T. M. & Martinis, J. M. Electronic microrefrigerator based on a normal-insulator-superconductor tunnel junction. *Applied Physics Letters* **65,** 3123–3125 (1994).
61. Muhonen, J. T., Meschke, M. & Pekola, J. P. Micrometre-scale refrigerators. *Reports on Progress in Physics* **75,** 046501 (2012).
62. Martinez-Perez, M., Fornieri, A. & Giazotto, F. Rectification of electronic heat current by a hybrid thermal diode. *Nature Nanotech.* **10,** 303–307 (2015).
63. Zhang, X., Lowell, P. J., Wilson, B. L., O'Neil, G. C. & Ullom, J. N. Macroscopic Subkelvin Refrigerator Employing Superconducting Tunnel Junctions. *Phys. Rev. Applied* **4,** 024006 (2 2015).
64. Nguyen, H. Q., Meschke, M. & Pekola, J. P. A robust platform cooled by superconducting electronic refrigerators. *Applied Physics Letters* **106,** 012601 (2015).

65. Mykkänen, E. *et al.* Thermionic junction devices utilizing phonon blocking. *Science Advances* **6** (2020).
66. Muhonen, J. T. *et al.* Electronic cooling of a submicron-sized metallic beam. *Applied Physics Letters* **94,** 073101 (2009).
67. Miller, N. A. *et al.* High resolution x-ray transition-edge sensor cooled by tunnel junction refrigerators. *Applied Physics Letters* **92,** 163501 (2008).
68. Timofeev, A. V., Helle, M., Meschke, M., Möttönen, M. & Pekola, J. P. Electronic Refrigeration at the Quantum Limit. *Phys. Rev. Lett.* **102,** 200801 (20 2009).
69. Partanen, M. *et al.* Quantum-limited heat conduction over macroscopic distances. *Nat. Phys.* **12,** 460–464 (2016).
70. Tan, K. Y. *et al.* Quantum-circuit refrigerator. *Nature Communications* **8,** 15189 (1 2017).
71. Ambegaokar, V. & Baratoff, A. Tunneling Between Superconductors. *Phys. Rev. Lett.* **10,** 486–489 (11 1963).
72. Dynes, R. C., Garno, J. P., Hertel, G. B. & Orlando, T. P. Tunneling Study of Superconductivity near the Metal-Insulator Transition. *Phys. Rev. Lett.* **53,** 2437–2440 (25 1984).
73. Pekola, J. P. *et al.* Environment-Assisted Tunneling as an Origin of the Dynes Density of States. *Physical Review Letters* **105,** 026803 (2010).
74. Koppinen, P. J., Kühn, T. & Maasilta, I. J. Effects of Charging Energy on SINIS Tunnel Junction Thermometry. *Journal of Low Temperature Physics* **154,** 179–189 (2009).
75. R.S., L. R. S. LVI. On the influence of obstacles arranged in rectangular order upon the properties of a medium. *The London, Edinburgh, and Dublin Philosophical Magazine and Journal of Science* **34,** 481–502 (1892).
76. Xia, Y., Gates, B., Yin, Y. & Lu, Y. Monodispersed Colloidal Spheres: Old Materials with New Applications. *Advanced Materials* **12,** 693–713 (2000).
77. Shen, Y. *The Principles of Nonlinear Optics* (Wiley, 1984).
78. Bass, M. *Handbook of Optics: Fundamentals, techniques, and design Handbook of Optics* **Vol. 1** (McGraw-Hill, 1994).
79. Sun, H. & Kawata, S. in *NMR - 3d Analysis - Photopolymerization* 169–273 (Springer Berlin Heidelberg, Berlin, Heidelberg, 2004).
80. Cumpston, B. H. *et al.* Two-photon polymerization initiators for 3D optical data storage and microfabrication. *Nature* **398,** 51–54 (1999).
81. Sun, H., Matsuo, S. & Misawa, H. Three-dimensional photonic crystal structures achieved with two-photon-absorption photopolymerization of resin. *Applied Physics Letters* **74,** 786–788 (1999).

82. Sun, H.-B. *et al.* Real three-dimensional microstructures fabricated by photopolymerization of resins through two-photon absorption. *Opt. Lett.* **25,** 1110–1112 (2000).

83. Kawata, S., Sun, H., Tanaka, T. & Takada, K. Finer features for functional microdevices. *Nature (London)* **412,** 697–698 (2001).

84. Deubel, M. *et al.* Direct laser writing of three-dimensional photonic-crystal templates for telecommunications. *Nature Materials* **3,** 444–447 (2004).

85. Ergin, T., Stenger, N., Brenner, P., Pendry, J. B. & Wegener, M. Three-Dimensional Invisibility Cloak at Optical Wavelengths. *Science* **328,** 337–339 (2010).

86. Reeves, J. B. *et al.* Tunable Infrared Metasurface on a Soft Polymer Scaffold. *Nano Letters* **18,** 2802–2806 (2018).

87. Thiele, S., Arzenbacher, K., Gissibl, T., Giessen, H. & Herkommer, A. M. 3D-printed eagle eye: Compound microlens system for foveated imaging. *Science Advances* **3** (2017).

88. Johlin, E., Mann, S. A., Kasture, S., Koenderink, A. F. & Garnett, E. C. Broadband highly directive 3D nanophotonic lenses. *Nature Communications* **9,** 4742 (2018).

89. Olsen, M. H. *et al.* In-chip fabrication of free-form 3D constructs for directed cell migration analysis. *Lab Chip* **13,** 4800–4809 (24 2013).

90. Lin, Y., Gao, C., Gritsenko, D., Zhou, R. & Xu, J. Soft lithography based on photolithography and two-photon polymerization. *Microfluidics and Nanofluidics* **22,** 97 (2018).

91. Bückmann, T., Thiel, M., Kadic, M., Schittny, R. & Wegener, M. An elastomechanical unfeelability cloak made of pentamode metamaterials. *Nature Communications* **5,** 4130 (2014).

92. Meza, L. R. *et al.* Resilient 3D hierarchical architected metamaterials. *Proceedings of the National Academy of Sciences* **112,** 11502–11507 (2015).

93. Röhrig, M., Thiel, M., Worgull, M. & Hölscher, H. 3D Direct Laser Writing of Nano- and Microstructured Hierarchical Gecko-Mimicking Surfaces. *Small* **8,** 3009–3015 (2012).

94. Liu, X. *et al.* 3D Printing of Bioinspired Liquid Superrepellent Structures. *Advanced Materials* **30,** 1800103 (2018).

95. Klein, F. *et al.* Elastic Fully Three-dimensional Microstructure Scaffolds for Cell Force Measurements. *Advanced Materials* **22,** 868–871 (2010).

96. Nishiguchi, D., Aranson, I. S., Snezhko, A. & Sokolov, A. Engineering bacterial vortex lattice via direct laser lithography. *Nature Communications* **9,** 4486 (2018).

97. Marino, A., Filippeschi, C., Mattoli, V., Mazzolai, B. & Ciofani, G. Biomimicry at the nanoscale: current research and perspectives of two-photon polymerization. *Nanoscale* **7,** 2841–2850 (7 2015).

98. Franssila, S. *Introduction to microfabrication* (John Wiley & Sons, 2010).
99. Gansel, J. K. *et al.* Gold Helix Photonic Metamaterial as Broadband Circular Polarizer. *Science* **325,** 1513–1515 (2009).
100. Zeeshan, M. A. *et al.* Hybrid Helical Magnetic Microrobots Obtained by 3D Template-Assisted Electrodeposition. *Small* **10,** 1284–1288 (2014).
101. Williams, G. *et al.* Two-photon lithography for 3D magnetic nanostructure fabrication. *Nano Research* **11,** 845–854 (2018).
102. Braun, A. & Maier, S. A. Versatile Direct Laser Writing Lithography Technique for Surface Enhanced Infrared Spectroscopy Sensors. *ACS Sensors* **1,** 1155–1162 (2016).
103. Cooper, K. A. *et al. Conformal photoresist coatings for high aspect ratio features* (SUSS MicroTec Waterbury Center, VT, USA, 2007).
104. Serbin, J. *et al.* Femtosecond laser-induced two-photon polymerization of inorganic–organic hybrid materials for applications in photonics. *Opt. Lett.* **28,** 301–303 (2003).
105. Zhou, X., Hou, Y. & Lin, J. A review on the processing accuracy of two-photon polymerization. *AIP Advances* **5,** 030701 (2015).
106. Oakdale, J. S., Ye, J., Smith, W. L. & Biener, J. Post-print UV curing method for improving the mechanical properties of prototypes derived from two-photon lithography. *Opt. Express* **24,** 27077–27086 (2016).
107. Lee, K.-S., Kim, R. H., Yang, D.-Y. & Park, S. H. Advances in 3D nano/micro-fabrication using two-photon initiated polymerization. *Progress in Polymer Science* **33,** 631–681 (2008).
108. Heiskanen, S. *Fabrication of a gap structure for near-field heat transfer* MA thesis (University of Jyväskylä, 2016).
109. Court, N. A., Ferguson, A. J. & Clark, R. G. Energy gap measurement of nanostructured aluminium thin films for single Cooper-pair devices. *Superconductor Science and Technology* **21,** 015013 (2007).
110. Wellstood, F. C., Urbina, C. & Clarke, J. Hot-electron effects in metals. *Phys. Rev. B* **49,** 5942–5955 (9 1994).
111. Pekola, J. P. *et al.* Limitations in Cooling Electrons using Normal-Metal-Superconductor Tunnel Junctions. *Phys. Rev. Lett.* **92,** 056804 (5 2004).
112. Pekola, J. P. *et al.* Trapping of quasiparticles of a nonequilibrium superconductor. *Applied Physics Letters* **76,** 2782–2784 (2000).
113. Meservey, R. & Tedrow, P. Spin-polarized electron tunneling. *Physics reports* **238,** 173–243 (1994).
114. Cohen, R. W. & Abeles, B. Superconductivity in Granular Aluminum Films. *Phys. Rev.* **168,** 444–450 (2 1968).

115. Giazotto, F, Solinas, P, Braggio, A & Bergeret, F. Ferromagnetic-insulator-based superconducting junctions as sensitive electron thermometers. *Physical Review Applied* **4,** 044016 (2015).

116. Karvonen, J. T. & Maasilta, I. J. Influence of Phonon Dimensionality on Electron Energy Relaxation. *Phys. Rev. Lett.* **99,** 145503 (14 2007).

117. Fisher, P. A., Ullom, J. N. & Nahum, M. High-power on-chip microrefrigerator based on a normal- metal/insulator/superconductor tunnel junction. *Applied Physics Letters* **74,** 2705–2707 (1999).

118. Hekking, F. & Nazarov, Y. V. Subgap conductivity of a superconductor–normal-metal tunnel interface. *Physical Review B* **49,** 6847 (1994).

119. Faivre, T, Golubev, D. & Pekola, J. Andreev current for low temperature thermometry. *Applied Physics Letters* **106,** 182602 (2015).

120. Graff, K. F. *Wave motion in elastic solids* (Oxford University Press, 1975).

121. Kühn, T., Anghel, D. V., Pekola, J. P., Manninen, M. & Galperin, Y. M. Heat transport in ultrathin dielectric membranes and bridges. *Phys. Rev. B* **70,** 125425 (12 2004).

122. Stephens, R., Cielospyk, G. & Salinger, G. Thermal conductivity and specific heat of non-crystalline solids: Polystyrene and polymethyl methacrylate. *Physics Letters A* **38,** 215–217 (Jan. 1972).

ORIGINAL PAPERS

PI

NANOFABRICATION ON 2D AND 3D TOPOGRAPHY VIA POSITIVE-TONE DIRECT-WRITE LASER LITHOGRAPHY

by

Heiskanen, S., Geng, Z., Mastomäki, J. & Maasilta, I.J.

Adv. Eng. Mater. **22**, 1901290 (2020).

Reproduced with kind permission of Wiley-VCH GmbH.

https://doi.org/10.1002/adem.201901290

ADVANCED ENGINEERING MATERIALS
www.aem-journal.com

Nanofabrication on 2D and 3D Topography via Positive-Tone Direct-Write Laser Lithography

*Samuli Heiskanen, Zhuoran Geng, Jaakko Mastomäki, and Ilari J. Maasilta**

Direct laser writing (DLW) lithography using two-photon absorption is a powerful technique mostly used for the fabrication of complex structures in micro- and nanoscale, by photopolymerizing a negative-tone resist. In contrast, herein, it is demonstrated that DLW is also well suited for fabricating nano- to microscale metallic structures using liftoff and a positive-tone photoresist. It is shown first that versatile, fast, and large-area fabrication is possible on flat 2D insulating substrates, and an expression for how the line width varies with the scanning speed is derived, with excellent agreement with the experiments. Even more interestingly, a unique application for the DLW lift-off process is demonstrated, by fabricating submicron scale metallic wiring on uneven substrates with sloping elevation changes as high as 20 µm. Such fabrication is practically impossible with more standard lithographic techniques.

1. Introduction

3D, direct laser writing (DLW) lithography based on two-photon absorption (TPA) is a fairly recent and powerful technique used for 3D writing of nano and microscale structures into photoresists.[1–3] Some of the main application areas demonstrated are photonics,[4,5] micro-optics,[6,7] mechanical metamaterials,[8,9] microfluidics,[10,11] biomimetics,[12,13] and micro and cell biology.[14–16] In most of these applications, the goal of the fabrication is the direct patterning of complex shapes, and as such, negative-tone photoresists, where exposed areas form the final structure, are often preferred and heavily used. Moreover, typically the highest-resolution resists are liquids, allowing only negative-tone operation.

In contrast, in traditional top-down nano- and microfabrication such as planar 2D UV photolithography and electron-beam lithography, positive-tone solid-state resists are very commonly used as a mask in nano- and microscale electrical device fabrication, where the exposed regions can be removed in a development step. This is highly useful where small features are deposited onto or etched into the substrate, as only the small feature areas (lines, dots, etc.) need to be exposed.

In contrast, in the field of direct-write TPA microfabrication, positive-tone solid-state resists have not been so widely used. For 3D structuring, combining positive-tone resists with electrodeposition of metallic structures without electrical contacts and liftoff was demonstrated for photonic[17] and mechanical metamaterials,[18] magnetic microrobots,[19] and magnetic nanostructures,[20] with the smallest feature size in the metal around 400–500 nm. In addition, 3D $4 \times 4\,\mu m^2$ microchannel structures[21] and micrometer scale molds[22] have also been demonstrated via positive-tone resists and TPA writing. In addition, a recent study[23] also pointed out the relevance of TPA direct writing in fabricating purely 2D, large-area metallic nanostructures (feature sizes above 400 nm) designed for plasmonic applications, using a positive-tone resist and liftoff.

In this article, our focus is twofold: first, we demonstrate the capabilities of the TPA writing for flat surfaces in the fabrication of long and narrow metal wiring and wire meshes using a positive-tone resist and liftoff and discuss its strengths in comparison with more traditional lithographic techniques. Second, and perhaps more importantly, we also demonstrate the fabrication and electrical measurement of submicron conducting wiring on uneven, 3D topography using a positive-tone photoresist and DLW TPA fabrication. Especially, this second application offers unique opportunities, as such fabrication is not available with traditional electron beam, ion beam, or photolithography. Inkjet printing could be used to pattern some materials onto uneven surfaces, but the resolution available with that technique is typically about an order of magnitude inferior, and it is limited by the available metal nanoparticle pastes.

It is also possible, alternatively, to use DLW to write metallic structures using photoreduction, even in 3D.[24,25] Although those techniques are promising, the method presented here has the benefit that it relies on the established photoresists and evaporation techniques, known to produce high-quality pure materials with low roughness, important for advanced devices such as tunnel junctions, for example. In addition, the whole palette of metals is available, whereas the range of materials (Ag, Au, and Cu) produced by the DLW photoreduction technique (often metal–polymer composites) and their quality are limited by the chemistry involved.[24,25]

The article is organized as follows: we first systematically investigate the quantitative characteristics of applying our DLW nanofabrication tool (Photonic Professional by Nanoscribe GmbH) to a positive-tone solid-state resist which has not been

S. Heiskanen, Z. Geng, J. Mastomäki, Prof. I. J. Maasilta
Department of Physics
Nanoscience Center
University of Jyvaskyla
P. O. Box 35, Jyväskylä FIN-40014, Finland
E-mail: maasilta@jyu.fi

The ORCID identification number(s) for the author(s) of this article can be found under https://doi.org/10.1002/adem.201901290.

DOI: 10.1002/adem.201901290

© 2019 WILEY-VCH Verlag GmbH & Co. KGaA, Weinheim

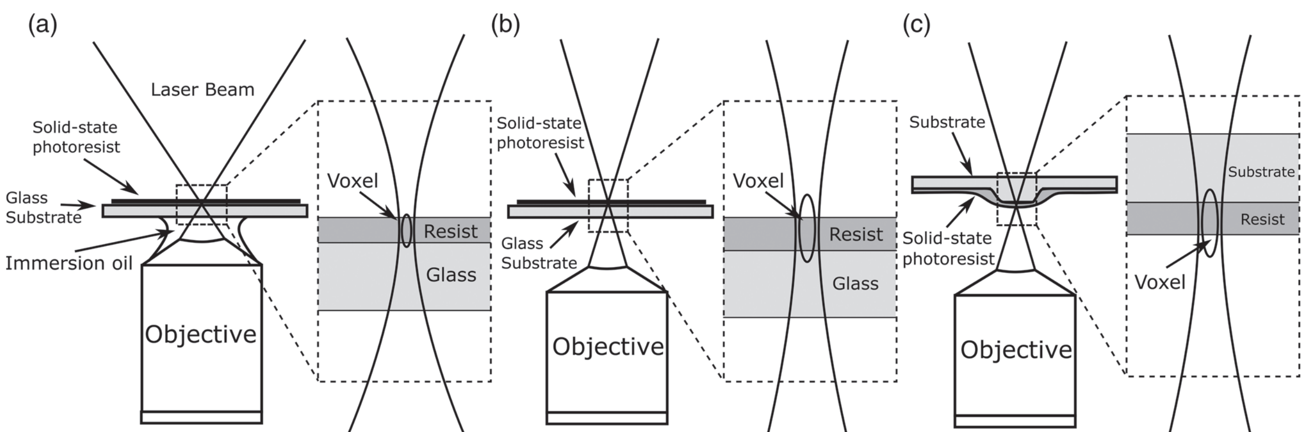

Figure 1. Different exposure methods used. a) Immersion objective method, widely used in TPA lithography process. An inverted high NA objective is dipped into immersion oil, with the refraction index matched to the glass substrate used. A laser beam is tightly focused around the interface between the photoresist and the front surface of the glass substrate, where the TPA process forms the voxel. b) Air-gap objective method through a glass substrate. An inverted objective is not in contact with the substrate, but has an air-gap. A laser beam is tightly focused as before. c) Air-gap objective method for writing on uneven topography. An inverted objective is not in contact with the substrate, but has an air-gap. The laser beam focus travels in *z*-direction, following the existing topography on the front surface, where the TPA process forms the voxel.

reported before for TPA lithography (AR-P 3120 photoresist by Allresist GmbH). We use both the common immersion objective method, **Figure 1**a, which can only be used with transparent substrates, and the air-gap objective method, Figure 1b,c, suitable also for opaque substrate materials. Section 2.1 first describes the writing tests on the resist using an immersion objective, whereas in Section 2.2, we compare similar results obtained with an air-gap objective. In Section 3, we demonstrate some examples of a full fabrication process of metallic wiring structures, using liftoff on flat surfaces, down to 330 nm wire width and 650 nm pitch. Finally, in Section 4, we demonstrate the fabrication of metallic wiring on complex, engineered 3D topography.

2. Resolution and Speed of 2D Patterning Using a Positive-Tone Resist

2.1. Resist Tests on Glass Substrates Using an Immersion Objective

The exposed volume in the positive-tone resist will be removed after the development, leaving openings to the resist, in contrast to negative-tone resists, where the exposed volume is polymerized and thus directly forms the corresponding voxel shape. This gives us a way to measure the lateral resolution of the voxel under scanning electron microscopy (SEM). First, we study the lateral resolution of both stationary spots and continuously scanned lines as a function of the laser output power, the spot exposure time, or the scan speed.

Using the immersion oil method (details in Section 6), we first systematically exposed our sample at single stationary locations, with varying laser power (ranging from 0.2 to 8 mW) and exposure time (ranging from 0.8 ms to 1 s), as shown in **Figure 2**d. The laser focus was kept at the resist to air interface. The lateral diameters of the exposed spots were measured with an SEM (eLiNE, Raith GmbH, manual fitting) and plotted as a function of exposure time t with different laser output powers, as shown in Figure 2a, and as a function of laser output power P with different exposure times, as shown in Figure 2b. In both figures, theoretical fits to a function $A\sqrt{\ln(BP^2t)}$ (with A and B as the fitting parameters) are also shown, with excellent agreement. This nonlinear dependence is based on known TPA theory[26,27] and agrees with studies on negative-tone[26,28,29] and positive-tone[30] resists reported by other groups. We stress that we only plot exposures that resulted in well-behaving round spots, as exemplified in Figure 2d. Odd-shaped spots were typically generated when the resist was underexposed and thus more susceptible to external interference such as vibrations and acoustic noise.

Moreover, we found that the voxel diameter dependence on the laser power P and the exposure time t can be combined into a collective exposure parameter P^2t, where the square of the laser power P^2 is multiplied by the exposure time t, as shown in Figure 2c. This dependence is in agreement with the nonlinear absorption rate of the second order photons in the TPA process, as seen before,[27] and indicates that it is this collective exposure parameter (proportional to an effective dose) that needs to be tuned, based on the requirements for the resolution in the AR-P 3120 positive-tone resist lithography. Note that for one-photon absorption, the effective dose would be proportional to Pt instead.

We performed another experiment by continuously exposing the sample with different stage scanning speeds, ranging from 10 to 400 $\mu m\,s^{-1}$ using different laser output powers (ranging from 2 mW to 6 mW). The line width was again measured with the SEM (**Figure 3**d), and in Figure 3a, we plot the measured width as a function of the stage scanning speed, with different laser output powers. From Figure 3a, we see that the line width has clearly a nonlinear dependence on the scanning speed, as can be seen from the fitting functions. These fits were obtained using a theory for the line width w, derived in the Supporting Information, assuming linear motion of the laser spot with speed v

© 2019 WILEY-VCH Verlag GmbH & Co. KGaA, Weinheim

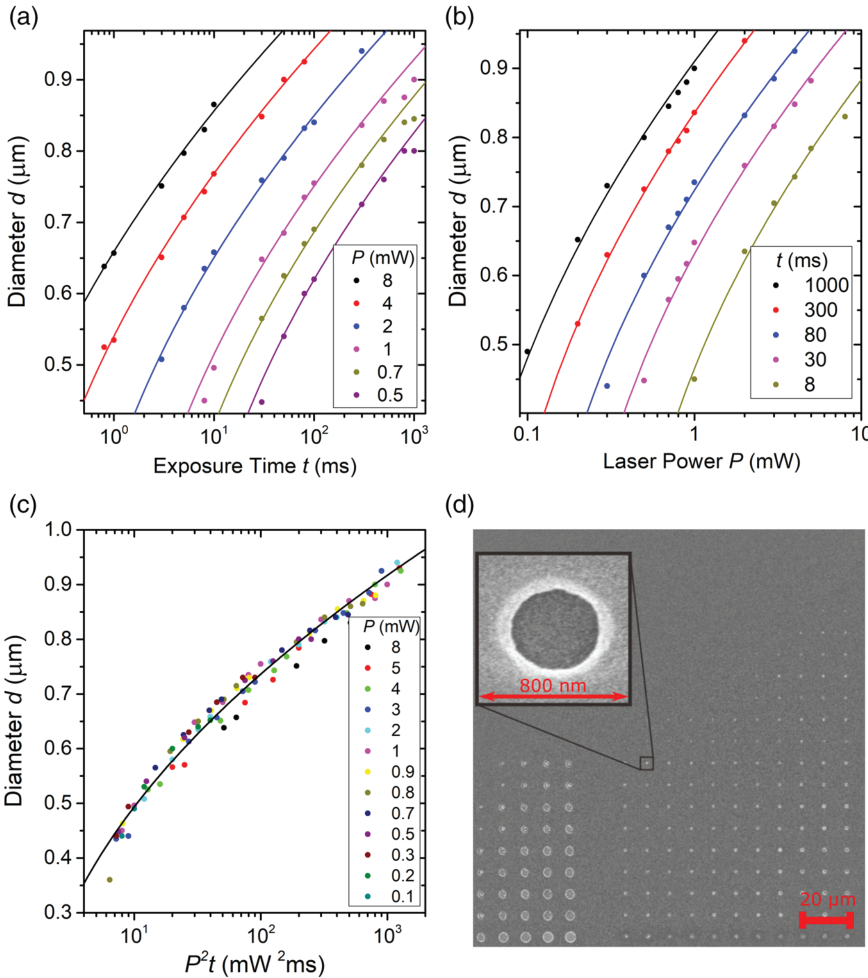

Figure 2. Point tests with the immersion oil method. a) Diameter of the exposed spots as a function of exposure time, with different laser output powers. The solid points are the SEM measured data; the solid lines are theoretical fits. b) Diameter of the exposed spot as a function of laser output power with different exposure times. The solid points are the SEM measured data; the solid lines are theoretical fits. c) Diameter of the exposed spot as a function of the collective exposure output P^2t. The solid points are the SEM measured data; the solid line is a theoretical fit. All the fits use a two-parameter function $A\sqrt{\ln(BP^2t)}$, with values $A = 360$ nm, $B = 6.55 \times 10^8$ W^{-2} s^{-1} for the fit to all data in (c). d) SEM image of a grid of point exposures with different exposure parameters, with the inset showing an example of an exposed spot after development.

$$w = \omega_0 \sqrt{\ln\left(\frac{\sigma_2 I_0^2}{C} \frac{\sqrt{\pi}}{2} \frac{\omega_0}{v}\right)} \quad (1)$$

where ω_0 is the beam waist at the focal plane, σ_2 is the effective two-photon cross section, I_0 is the time-averaged laser beam photon flux intensity at the beam center (photons/area/s), and $C = \ln[\rho_0/(\rho_0 - \rho_{th})]$ is a resist-dependent material parameter,[26,27] with ρ_0 the initiator density and ρ_{th} the threshold density for radicals to initiate reaction in the resist. In the experiment, the parameter controlling I_0 is the output power of the laser P, as there is a direct proportionality between the two.[26,27]

Comparing with the spot exposure experiment, Equation (1) predicts that the exposure parameter controlling the line width in scanning mode is P^2/v instead of P^2t. We can check this by plotting all line-width data as a function of P^2/v, as shown in Figure 3c. Again, we obtain great agreement between the experiment and the theory, except at the highest P^2/v values, where possibly the density of radicals saturates and diffusion rate starts increasing.

Based on Equation (1), we see that for a fixed target line width w, if one wants to increase the writing speed, the power does not need to be increased linearly, as would be the case for one-photon absorption, but only as a square root. Figure 3b shows this fact for our experimental conditions, where we plot the quadratic scanning speed increase with the increased laser output power, for three different line widths, based on the fits of Figure 3a. The possibility to increase the scanning speed quadratically with the laser output power enables ultrafast DLW for a large-scale 2D fabrication. As we see from Figure 3b, one could use writing speeds of $\approx$6 mm s^{-1} for a 400 nm line for this resist with a realistic output power of 10 mW. Unfortunately, in this study, we were limited by the accuracy of our motorized stage and could

© 2019 WILEY-VCH Verlag GmbH & Co. KGaA, Weinheim

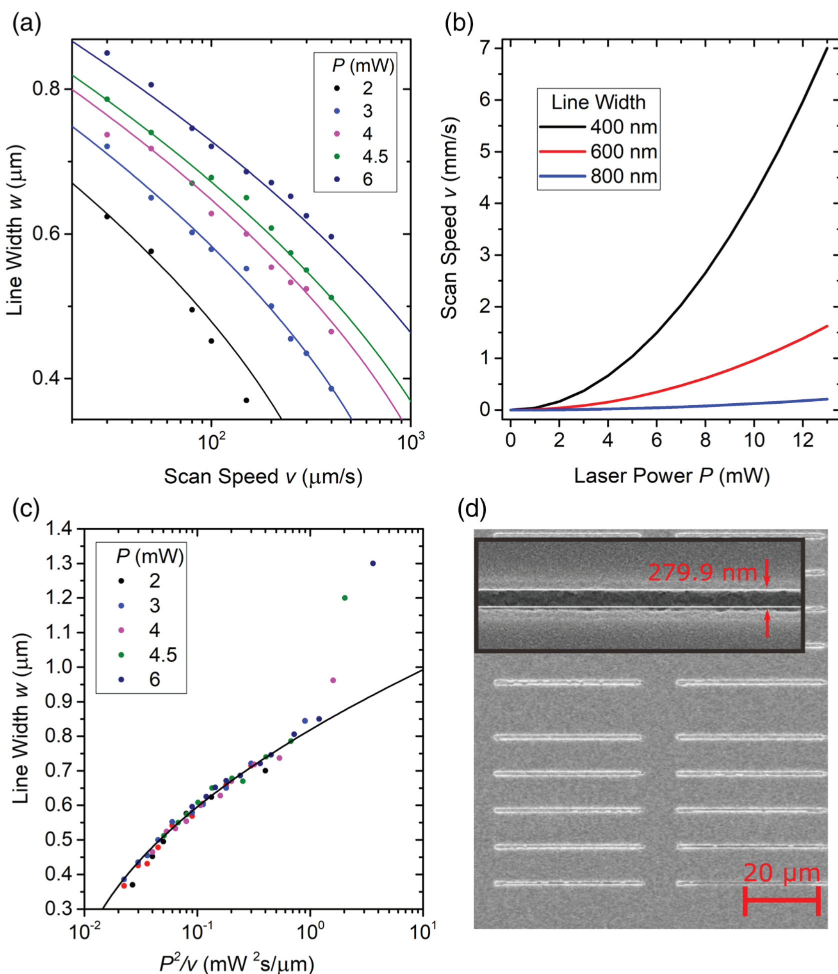

Figure 3. Line tests with the immersion oil method. a) Measured line width as a function of the stage scan speed, with different laser output powers. The solid points are the measured data, and the lines are two-parameter fits to the theory of Equation (1). b) Simulation of the stage scan speed as a function of laser output power for different desired line widths, based on the measured data. c) Measured line width as a function of the collective exposure parameter P^2/v. The solid points are the measured data; the solid line is a two-parameter fit based on the theory of Equation (1) $w = A\sqrt{\ln(BP^2/v)}$, with $A = 370$ nm, $B = 133.4$ m W^{-2} s^{-1}. d) SEM image of a grid of line exposures with varying exposure parameters. The inset is a zoomed-in SEM image of an exposed line after development.

not test the ultrafast DLW mode at speeds above a millimeter per second. Setups using galvo mirrors (commercially available) can reach up to 20 mm s^{-1} scanning speeds,[31] and fast TPA writing with such a setup and a different resist (AZ MiR 701) was demonstrated before.[23] Moreover, the nonlinear relation between the scan speed and the line width can also be utilized as a velocity-dependent “shutter mechanism” for DLW without using physical shutters, as reported before for the negative SU-8 resist.[29]

Note that smaller diameters and line widths of the order of 100 nm have been reported in the literature for DLW writing into a positive-tone resist,[30] using a much thinner resist layer of ≈150 nm. The thin resist allows one to shift the focus plane in such a way to use only the tip of the voxel, to gain in resolution. However, this type of tuning was not considered in this article, as the resist profile generated in such a manner[30] is not suitable for liftoff and transfer of the pattern to metallic structures.

2.2. Resist Tests on Glass Substrates Using an Air-Gap Objective

DLW can be also performed with an air-gap objective, which provides a more versatile alternative to an immersion oil objective, as it is not in contact with the substrate. This makes it possible, e.g., to expose features on the front side of opaque substrates, and particularly on an already existing larger surface topography, an option we will focus on in Section 4. However, for comparison with the results obtained earlier with the immersion oil objective, we first study the characteristics of exposing the same AR-P 3120 positive-tone resist through glass substrates with the air-gap objective (numerical aperture, NA = 0.75, magnification 63×, Zeiss GmbH), as shown in Figure 1b. An obvious drawback of such an air gap objective is its lower resolution. However, if 1–2 μm scale features are wanted, the writing speed can be faster compared with the immersion oil method.

© 2019 WILEY-VCH Verlag GmbH & Co. KGaA, Weinheim

As in Section 2.1, the resolution of the air-gap method was studied by measuring the diameter of single spots exposed by varying the laser power P and the exposure time t (**Figure 4**a) and by measuring the line widths by varying the laser power P and the stage scanning speed v (Figure 4b), with the laser focused at the surface of a 500 nm thick resist. The smallest spots and lines have dimensions ≈400 nm, but they do not go completely through the resist. The optimal points have a larger 600–800 nm diameter. As before for the immersion oil method, the theories for the spot diameter[26,27,30] and the line width, Equation (1), fit very well to most of the data, when plotted as a function of the correct combined effective dose parameters (P^2t for spots P^2/v for lines), as evident in Figure 4c,d. Only at the highest effective dose ranges do the diameters and widths increase beyond what is expected from the theory. This effect, which is an abrupt change in the case of stationary spots, was observed to be caused by the collapse of the overhanging edges, as the exposed resist profile has an undercut at high doses. From Figure 4b, we also see that we managed to use high speeds of 2 mm s^{-1} to write lines of width below 500 nm.

Another interesting aspect is the length of a voxel at different working parameters. This was studied by moving the laser focus vertically so that the length of a voxel can be determined from the end points where the very "tail" of a voxel still exposes the resist. The plot of the voxel length as a function of P^2t is shown in **Figure 5**. The results indicate that voxels are rather tall (≈2 μm) even with the lowest doses. However, an elongated voxel is a benefit for 2D patterning: a thicker resist can be exposed with

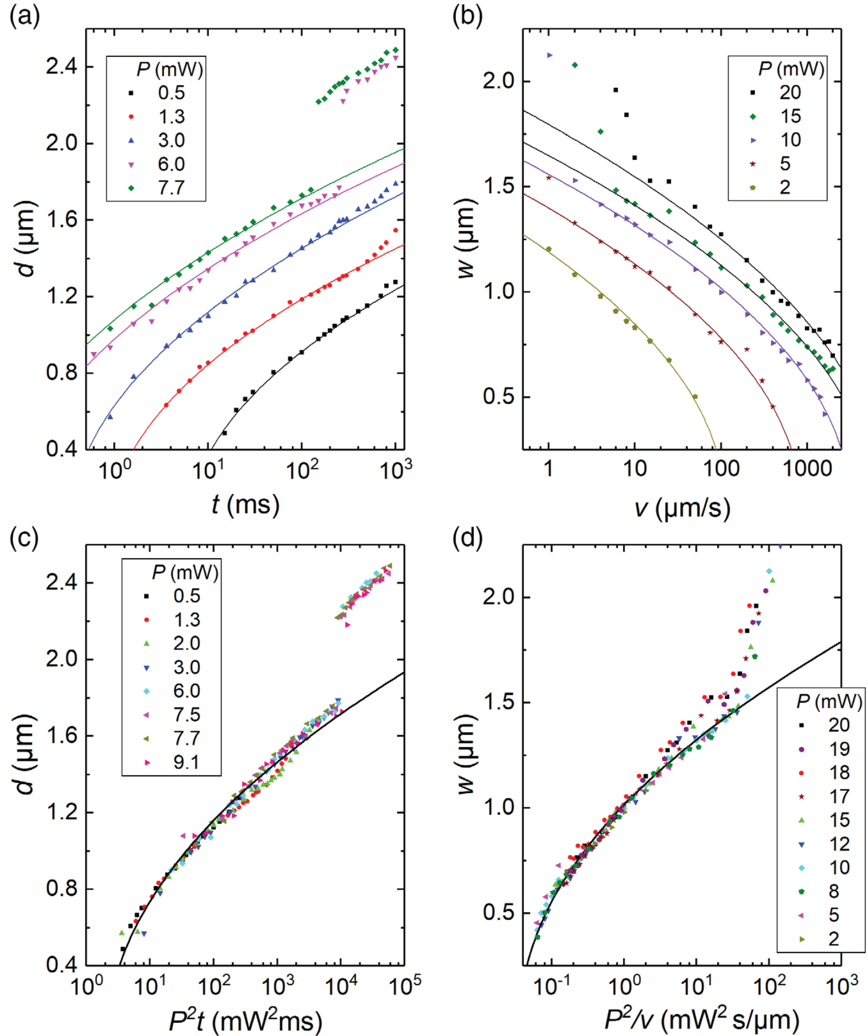

Figure 4. Point and line tests with the air-gap method. a) Diameter of single spots exposed with the air-gap objective, as a function of the exposure time t and the laser power P (points). The lines are the best fits to functions $A\sqrt{\ln(BP^2t)}$. b) Width of the exposed lines as a function of the stage scanning speed with different laser output powers. The lines are two-parameter fits to Equation (1). c) Diameter of the exposed spots as a function of the combined exposure parameter P^2t. The points are the SEM measured data; the solid line is a two-parameter fit to $A\sqrt{\ln(BP^2t)}$ with $A = 590$ nm, $B = 4.78 \times 10^8$ m W^{-2} s^{-1}. d) Measured line widths as a function of the combined exposure parameter P^2/v. The points are the measured data; the solid line is a two-parameter fit based on the theory of Equation (1), $w = A\sqrt{\ln(BP^2/v)}$, with $A = 560$ nm, $B = 26.9 \times 10^8$ m W^{-2} s^{-1}. The discrepancy between the theory and experiment at high effective doses is due to the collapse of the undercut profile of the resist, and those points were excluded from the fits.

© 2019 WILEY-VCH Verlag GmbH & Co. KGaA, Weinheim

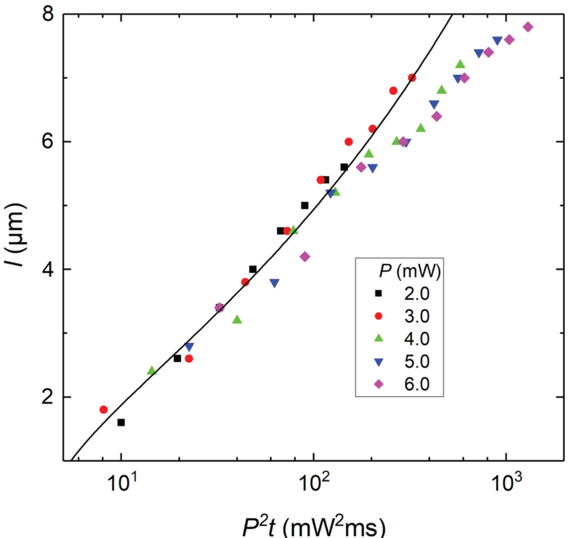

Figure 5. Voxel length l versus P^2t for a few laser powers, with a fitting function $l = A\sqrt{\sqrt{BP^2t} - 1}$ based on known TPA theory,[26,27] with $A = 2.48\,\mu m$, $B = 2.47 \times 10^8\ W^{-2}\ s^{-1}$. The voxel length is determined by exposing points at different laser focus heights with respect to the surface of the resist and calculating the distance between the first and the last exposed point. The discrepancy between the theory and experiment at high effective doses is due to the collapse of the undercut profile of the resist, and those points were excluded from the fits.

a single pass line, with an aspect ratio of roughly 5:1. To expose resists thicker than ≈1 μm, several passes at different vertical focal points can easily be used. Also, we point out that the undercut profile can likely be tuned by choosing an appropriate ratio between the resist thickness and the voxel length and by the placement of the focal plane. Undercut control is of course quite critical for successful lift-off processing, one of the major ways of using positive-tone resists.

3. Large-Scale Fabrication of Submicron Metallic Wiring on Flat Glass Substrates

With the aforementioned exposure knowledge, we have designed and fabricated metallized prototype samples, using the immersion oil DLW technique. It is quite important to demonstrate a complete fabrication sequence for devices, not just resist exposure tests, including metal evaporation and liftoff. We are aware of only one previous report[23] that studied TPA DLW writing with positive-tone resist in such a manner. One of the possible applications with this technique is the fabrication of submicron centimeter-long conducting wires and wire grids on transparent substrates, for electro-optical experiments. Such samples would be much harder, if not impossible, to fabricate with more standard techniques such as electron-beam lithography, due to difficulties with charging and stitching of the write fields.

The sample, shown schematically in **Figure 6**a, contains several sets of 2 cm long, continuous, and electrically conducting silver lines on a transparent glass substrate, with design line widths 450, 600, and 800 nm. For the narrowest line sets, we thus have an ultrahigh aspect ratio of width to length over 1:40 000. The sample also contains two $3 \times 3\ mm^2$ square mesh structures, which consist of hundreds of either 450 or 600 nm wide,

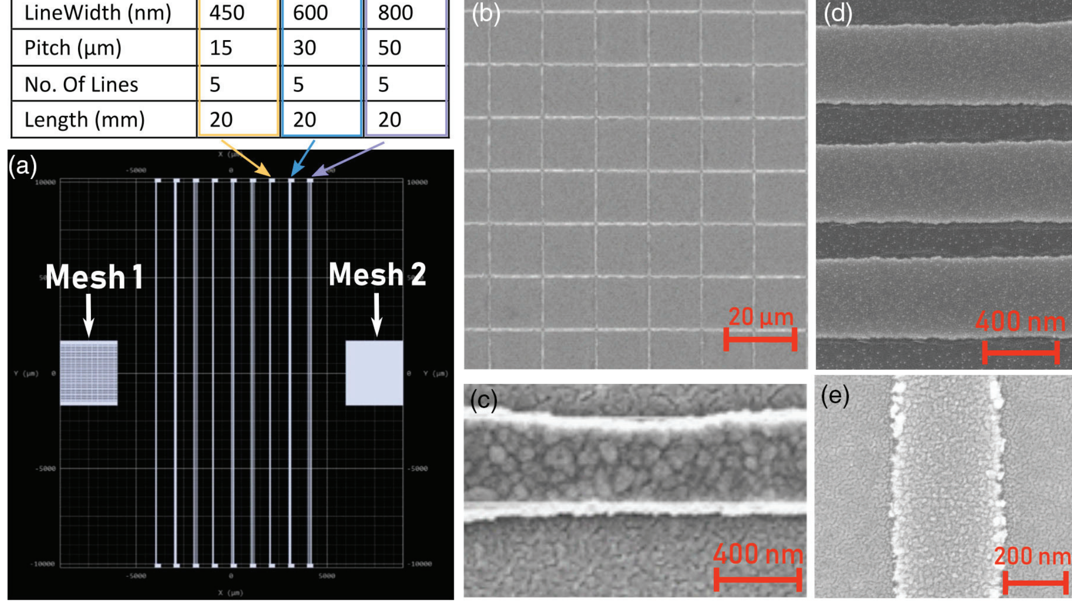

Figure 6. Large-scale wire fabrication on a flat substrate. a) Design of the 2D test sample. Groups of 20 mm long silver lines, with each group consisting of three sets of lines with three different line widths (450, 600, 800 nm), are located at the central region of the sample. In each line set, five identical lines are connected by a contact pad at each end. Two $3 \times 3\ mm^2$ square mesh structures are located to the left (Mesh 1) and right (Mesh 2) of the wires, with Mesh 1 (Mesh 2) consisting of 122 (402) 450 nm (600 nm) wide, 3 mm long sets of silver lines of pitch 50 μm (15 μm). b) SEM image of a part of the 450 nm meshed silver grid. c) Zoomed-in SEM image of a section of 450 nm wide, 20 mm long silver line. d) SEM image of 450 nm wide titanium lines with a 200 nm distance between them. e) SEM image of a 330 nm wide titanium line.

© 2019 WILEY-VCH Verlag GmbH & Co. KGaA, Weinheim

3 mm long crossing silver lines (Figure 6b). This sample thus demonstrates the advantages of TPA DLW for high-resolution, stitching-free, charging-free, fast-scanning-speed, large-scale, and versatile nanofabrication.

The sample is fabricated on a 170 μm thick glass substrate using a 500 nm thick layer of AR-P 3120 photoresist, spin coated, and developed as described in Section 6. The line width was controlled by a combination of the laser power and scanning speed used, with 2, 2.5, and 4 mW laser power, and 300, 180, and 50 $\mu m\ s^{-1}$ stage scanning speed used during the exposure for the 450, 600, and 800 nm line widths, respectively. Note that the scanning was performed with a motorized stage instead of the piezoelectric scanner, to allow for scanning lengths beyond the scan range of the piezostage, limited to 300 μm. After development, the exposed glass surfaces were cleaned by a 40 mTorr, 40 W, 50 sccm oxygen-plasma cleaning process in a reactive-ion etcher, followed by an ultrahigh vacuum (1×10^{-8} mbar) e-beam evaporation of a 200 nm-thick silver film. After the evaporation, liftoff was done with a hot AR 300-76 remover (Allresist GmbH) with a 2 s sonication.

Figure 6b shows a representative SEM image of a part of the 450 nm silver mesh, and Figure 6c presents an example of a higher-magnification SEM image of a long 450 nm silver line. As contact pads were also fabricated, we were also able to perform resistivity measurements on the structures, demonstrating the continuity of lines across such long lengths.

We also fabricated samples to find the resolution limits for this technique. For these samples, the same AR-P 3120 resist was used, but the thickness was lowered to 450 nm and the piezoelectric scanner was used for more accurate control of the scanning speed. Instead of silver, we used titanium for the metallization to improve adhesion. To find the highest possible pitch, we fabricated a sample with varying pitch, laser power, and focal height. The scanning speed was kept at 20 $\mu m\ s^{-1}$ based on the dose tests. With a 3 mW laser power and the laser focus at 400 nm below the resist surface, we achieved 450 nm lines with a 200 nm distance between them (Figure 6d). Similarly, we found the narrowest possible line, but now instead of the pitch, we also varied the scanning speed. The narrowest line was 330 nm wide (Figure 6e), drawn with a 2.5 mW laser power and a 50 $\mu m\ s^{-1}$ scanning speed.

4. Wire Fabrication on 3D Topography

Next, we demonstrate an even more promising application of 2D TPA DLW lithography: fabrication of metallic wiring on uneven surface topography. This application is very useful, as such a fabrication is extremely challenging with more standard photo- or e-beam lithographic techniques that operate on a flat focal plane. The uneven writing surface is not a problem with TPA DLW because the required height changes for the focal plane can easily be included in the wire design, as the sample stage can be moved in all coordinate directions. The technique also allows trivially the use of nonconducting substrate materials, in contrast to e-beam lithography. For this application, the air-gap objective is the only choice as the exposure needs to be done from the side of the 3D topographic structures and not through the substrate, schematically shown in Figure 1c. This is because of limitations of the working distance for through-substrate writing. Also, if the laser had to travel through multiple interfaces and the 3D structures, the laser intensity and resolution would be reduced. Writing through the substrate would also limit the usable substrate materials.

Wire fabrication on 3D topography was tested by first fabricating tall structures using the same DLW system. In this case, the structures were fairly simple cuboidal structures of height 20 μm, shown in **Figure 7**a,b, with ramps on the sides so that wiring from the substrate surface can be routed onto the cuboid. The cuboid structures were fabricated using the DiLL (Dip in Laser Lithography) method, in which an objective (NA = 1.3, 100×) is dipped in a liquid negative-tone photoresist (IP-Dip, Nanoscribe GmbH) for the exposure and photopolymerization. Transparent sapphire substrates were used to reduce reflections at the interface between the resist and the substrate.

After their fabrication, the cuboid structures need to be coated with the positive-tone AR-P resist for the wire fabrication (details in Section 6). Straightforward spin coating cannot be used due to the large 20 μm height of the structures; instead, direct spray coating[32] could be used. However, this method was not available to us, so we had to make modifications to the cuboid structure itself, to still allow for spin coating. First, walls had to be added to the outer rim of the cuboid, to create a sort of a bowl for the resist to stay in during spin coating (Figure 7b). Second, the structures

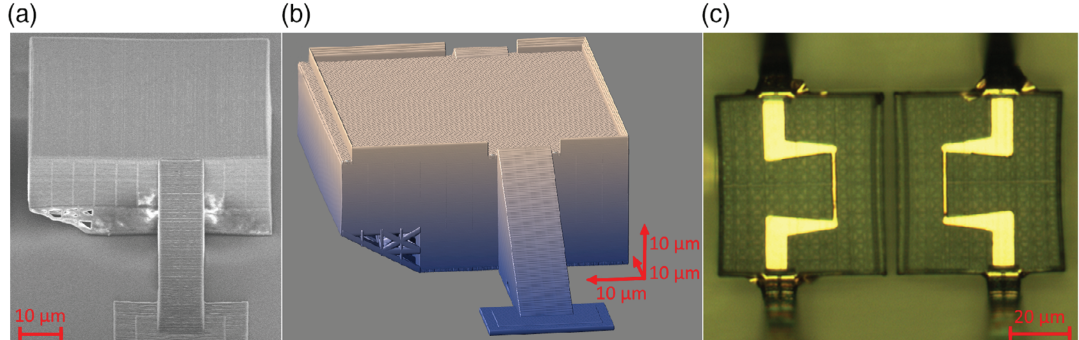

Figure 7. Wire fabrication on 3D topography. a) SEM micrograph of a 3D cuboid structure without side walls, also fabricated with DLW, from a side-angle view. The height of the structure is about 20 μm. b) Design of the modified 3D cuboid structure with walls surrounding the elevated platform. The width of the platform is 60 μm. c) Top-view optical micrograph of finished samples with deposited gold wiring traveling from the substrate to the platform. The width of the thinnest section of the wiring is about 1 μm.

© 2019 WILEY-VCH Verlag GmbH & Co. KGaA, Weinheim

were made much wider (≈$60 \times 60\,\mu m^2$); otherwise the proximity of the walls to the metal wiring would make the lift-off process unnecessarily hard. The walls are sloped on the inside to reduce their horizontal surface area. This smaller surface area reduced the amount of resist that adheres to the walls in the lift-off process.

Before doing the lithography for the wiring, most 3D structures were conformally coated with a 50 nm layer of aluminum oxide using atomic layer deposition (ALD).[33] This was done to make the structures mechanically stronger for the liftoff, although successful liftoff was also shown to be possible for non-coated, pure IP-Dip polymer structures. After the ALD coating, the structures were spin coated with four nominally 800 nm thick layers (1500 RPM and time 90 s) of the AR-P 3120 resist to get good coverage also on top of the structures. Then, the samples were exposed with DLW for the wiring with a line pattern that follows the ramp and platform topography of the underlying cuboid structure in 3D space, with alignment performed with the integrated optical microscope before the exposure. A writing speed $20\,\mu m\,s^{-1}$ was used, and the width of the lines was determined by changing the laser power between 10 and 20 mW, producing a smallest line width ≈800 nm. With faster speeds or lower power values, the resist was not fully exposed. At the base of the cuboid, several passes with varying focal points in z-direction were used to fully expose the somewhat thicker resist that accumulated in those regions.

After the development, the samples were coated with a ≈70 nm gold layer, with a thinner ≈20 nm titanium adhesion layer underneath, by electron beam evaporation in ultrahigh vacuum. The evaporation had to be done from multiple angles from the sides of the ramps, to get good film coverage also on the ramps (Section 6), as they contained small ≈100 nm vertical steps, as can be seen in Figure 7a. A finished sample with gold wiring routed from the substrate surface onto the cuboid platform using the ramps is shown in Figure 7c. As the figure shows, we have successfully demonstrated metal wire fabrication on 20 μm tall 3D structures, with the wiring climbing the structure from the substrate surface, using DLW and liftoff with a positive-tone resist. The continuity of the wiring was also demonstrated with electrical measurements, with the observed room-temperature resistance values typically around 35–40 Ω. For one sample, we also characterized the temperature dependence of the resistivity, showing a standard metallic behavior and an RRR of ≈2.8.

5. Conclusions

Our results clearly demonstrate the capabilities of DLW using TPA also for 2D lithography with liftoff, with metallic lines down to 450 nm width fabricated on very large areas, up to 2 cm. On smaller areas, 650 nm pitch and 330 nm line width were also demonstrated. As 2D lithography and liftoff are very common and established techniques in general, we should critically evaluate the strengths and weaknesses of using the TPA DLW technique for this purpose. The fact that the writing is maskless gives it versatility and suitability for research problems and prototyping, as opposed to standard photolithography that uses masks. DLW, in contrast, can be done in 2D with one-photon absorption, if UV lasers are used. A typical writing speed with the highest resolution (nominally around 300 nm) of such a laser lithography tool is of the order of millimeter per second; in other words, the resolution and speed are similar to what was demonstrated here. The main difference between one-photon absorption and TPA comes with how the line width scales with intensity, Equation (1). It means that if the intensity of the laser can be increased, the writing speed increase is quadratic in two-photon absorption as opposed to linear in one-photon absorption, favoring TPA eventually.

Even though the liftoff worked for the processing described here, one can also envision simple improvements that would enhance the undercut profile and thus help the liftoff. One could implement the well-known technique where two layers of different resists are used, with the more sensitive layer underneath. In addition, the TPA DLW technique uniquely allows for writing just one layer of resist at two different heights with different exposure parameters, which can be used to tune the undercut profile.

Even more promising, however, is the possibility we demonstrated here that 2D lithography is performed on uneven, nonflat topography. This seems to be the strong point of doing 2D lithography with an inherently 3D lithography system. We showed the feasibility of fabricating submicron scale metallic wires on a 3D structure with an elevation change as high as 20 μm, on a complex structure, using a positive-tone resist and liftoff. Such fabrication is extremely challenging, if not impossible, with more standard techniques that have to rely on the flatness of the substrate.

6. Experimental Section

Two-Photon Lithography Tool: The DLW nanofabrication tool used (Nanoscribe Photonic Professional) is based on a 80 MHz repetition rate pulsed fiber laser with a near-infrared wavelength (780 nm), with maximum laser power of 90 mW. A three-axis piezoelectrical stage is used for accurate motion of the substrate of distances below 300 μm, and a motorized stage is used for larger area movements.

Immersion Objective Method: In the immersion objective method, a transparent glass substrate with 170 μm thickness was mounted on the piezoelectrical stage with the resist side facing up, and an inverted microscope objective with 100× magnification and 1.4 NA was dipped into the immersion oil on the backside of the substrate as shown in Figure 1a. Instead of using the conventional liquid negative-tone resist, a spin coated, solid, positive-tone UV photoresist AR-P 3120 consisting of novolac resin and naphthoquinone diazide was used. The thickness of the resist was controlled by the spin speed and a short pre-exposure baking immediately followed after the spin. In our case, a 500 nm-thick resist was spun with 5000 RPM for 60 s, followed by a bake for 1 min at 100. After the laser exposure, the sample was first developed in a 1:1 mixture of AR 300-47 and deionized water for 1 min, then rinsed for 2 min in pure deionized water, and finally blow-dried with nitrogen gas.

Air-Gap Objective Method, Writing through Glass: In the air-gap objective method, an objective (Zeiss GmbH) with NA = 0.75 and magnification 63× was used, not in contact with the substrate. A transparent glass substrate with 170 μm thickness was mounted on the piezoelectrical stage with the resist side facing up. The same spin-coated, solid, positive-tone UV photoresist AR-P 3120 was used (500 nm thickness), spun with 5000 RPM for 60 s, followed by a bake for 1 min at 100, and developed in a 1:1 mixture of AR 300-47 and deionized water for 1 min, then rinsed for 2 min in pure deionized water, and blow-dried with nitrogen gas.

Air-Gap Objective Method, Wire Deposition on the 3D Topography: The 3D structures were spin coated with four 800 nm thick layers (1500 RPM

© 2019 WILEY-VCH Verlag GmbH & Co. KGaA, Weinheim

Table 1. Angles with respect to surface normal and thicknesses *d* used in the multiple angle evaporation sequence.

Angle [°]	*d* Ti [nm]	*d* Au [nm]
±75	1	3
±60	2	5
±45	3	10
±30	3	10
±15	4	15
0	6	30

and time 90 s) of the AR-P 3120 resist, which was baked at 100 C for 30 s between layers and for 1 min after the last layer. After the exposure and development (1:1 solution of AR 300-47 and deionized water for 1 min), the samples were coated with a ≈70 nm gold layer, with a thinner ≈20 nm titanium adhesion layer underneath, by electron beam evaporation in ultra-high vacuum. The evaporation was done from six different angles from both sides of the structure, first Ti, then Au, in a sequence shown in **Table 1**. The liftoff was done with heated and sprayed AR 300-76 remover.

Electrical Characterization of the Samples: The metalized wire samples of Section 3 were electrically characterized by measuring their resistance with a Keithley 2450 SourceMeter at room temperature. The resistance of the wiring on the 3D topography in Section 4 was measured with a multimeter, and in the case of the temperature dependence, with a Stanford SR830 lock-in amplifier at a frequency of ≈15 Hz.

Supporting Information

Supporting Information is available from the Wiley Online Library or from the author.

Acknowledgements

This study was supported by the Academy of Finland project number 298667.

Conflict of Interest

The authors declare no conflict of interest.

Keywords

direct laser writing, liftoff, nanofabrication, positive-tone resist, two-photon absorption

Received: October 24, 2019
Published online:

[1] H.-B. Sun, S. Matsuo, H. Misawa, *Appl. Phys. Lett.* **1999**, *74*, 786.
[2] S. Kawata, H.-B. Sun, T. Tanaka, K. Takada, *Nature* **2001**, *412*, 697.
[3] M. Deubel, G. von Freymann, M. Wegener, S. Pereira, K. Busch, C. M. Soukoulis, *Nat. Mater.* **2004**, *3*, 444.
[4] T. Ergin, N. Stenger, P. Brenner, J. B. Pendry, M. Wegener, *Science* **2010**, *328*, 337.
[5] J. B. Reeves, R. K. Jayne, T. J. Stark, L. K. Barrett, A. E. White, D. J. Bishop, *Nano Lett.* **2018**, *18*, 2802.
[6] S. Thiele, K. Arzenbacher, T. Gissibl, H. Giessen, A. M. Herkommer, *Sci. Adv.* **2017**, *3*, e1602655.
[7] E. Johlin, S. A. Mann, S. Kasture, A. F. Koenderink, E. C. Garnett, *Nat. Commun.* **2018**, *9*, 4742.
[8] T. Bückmann, M. Thiel, M. Kadic, R. Schittny, M. Wegener, *Nat. Commun.* **2014**, *5*, 4130.
[9] L. R. Meza, A. J. Zelhofer, N. Clarke, A. J. Mateos, D. M. Kochmann, J. R. Greer, *Proc. Natl. Acad. Sci.* **2015**, *112*, 11502.
[10] M. H. Olsen, G. M. Hjortø, M. Hansen, Ö. Met, I. M. Svane, N. B. Larsen, *Lab Chip* **2013**, *13*, 4800.
[11] Y. Lin, C. Gao, D. Gritsenko, R. Zhou, J. Xu, *Microfluid. Nanofluid.* **2018**, *22*, 97.
[12] M. Röhrig, M. Thiel, M. Worgull, H. Hölscher, *Small* **2012**, *8*, 3009.
[13] X. Liu, H. Gu, M. Wang, X. Du, B. Gao, A. Elbaz, L. Sun, J. Liao, P. Xiao, Z. Gu, *Adv. Mater.* **2018**, *30*, 1800103.
[14] F. Klein, T. Striebel, J. Fischer, Z. Jiang, C. M. Franz, G. von Freymann, M. Wegener, M. Bastmeyer, *Adv. Mater.* **2010**, *22*, 868.
[15] D. Nishiguchi, I. S. Aranson, A. Snezhko, A. Sokolov, *Nat. Commun.* **2018**, *9*, 4486.
[16] A. Marino, C. Filippeschi, V. Mattoli, B. Mazzolai, G. Ciofani, *Nanoscale* **2015**, *7*, 2841.
[17] J. K. Gansel, M. Thiel, M. S. Rill, M. Decker, K. Bade, V. Saile, G. von Freymann, S. Linden, M. Wegener, *Science* **2009**, *325*, 1513.
[18] X. W. Gu, J. R. Greer, *Extreme Mech. Lett.* **2015**, *2*, 7.
[19] M. A. Zeeshan, R. Grisch, E. Pellicer, K. M. Sivaraman, K. E. Peyer, J. Sort, B. Özkale, M. S. Sakar, B. J. Nelson, S. Pané, *Small* **2014**, *10*, 1284.
[20] G. Williams, M. Hunt, B. Boehm, A. May, M. Taverne, D. Ho, S. Giblin, D. Read, J. Rarity, R. Allenspach, S. Ladak, *Nano Res.* **2018**, *11*, 845.
[21] W. Zhou, S. M. Kuebler, K. L. Braun, T. Yu, J. K. Cammack, C. K. Ober, J. W. Perry, S. R. Marder, *Science* **2002**, *296*, 1106.
[22] I. Bernardeschi, O. Tricinci, V. Mattoli, C. Filippeschi, B. Mazzolai, L. Beccai, *ACS Appl. Mater. Interfaces* **2016**, *8*, 25019.
[23] A. Braun, S. A. Maier, *ACS Sens.* **2016**, *1*, 1155.
[24] E. H. Waller, G. von Freymann, *Nanophotonics* **2018**, *7*, 1259.
[25] L. Hirt, A. Reiser, R. Spolenak, T. Zambelli, *Adv. Mater.* **2017**, *29*, 1604211.
[26] J. Serbin, A. Egbert, A. Ostendorf, B. N. Chichkov, R. Houbertz, G. Domann, J. Schulz, C. Cronauer, L. Fröhlich, M. Popall, *Opt. Lett.* **2003**, *28*, 301.
[27] X. Zhou, Y. Hou, J. Lin, *AIP Adv.* **2015**, *5*, 030701.
[28] T. Tanaka, H.-B. Sun, S. Kawata, *Appl. Phys. Lett.* **2002**, *80*, 312.
[29] W. H. Teh, U. Dürig, U. Drechsler, C. G. Smith, H.-J. Güntherodt, *J. Appl. Phys.* **2005**, *97*, 054907.
[30] H.-Z. Cao, M.-L. Zheng, X.-Z. Dong, F. Jin, Z.-S. Zhao, X.-M. Duan, *Appl. Phys. Lett.* **2013**, *102*, 201108.
[31] T. Bückmann, R. Schittny, M. Thiel, M. Kadic, G. W. Milton, M. Wegener, *New J. Phys.* **2014**, *16*, 033032.
[32] K. A. Cooper, C. Hamel, B. Whitney, K. Weilermann, K. J. Kramer, Y. Zhao, H. Gentile, *Conformal Photoresist Coatings for High Aspect Ratio Features*, SUSS MicroTec Waterbury Center, Williston, VT **2007**.
[33] S. M. George, *Chem. Rev.* **2010**, *110*, 111.

© 2019 WILEY-VCH Verlag GmbH & Co. KGaA, Weinheim

PII

SUPERCONDUCTING TUNNEL JUNCTION FABRICATION ON THREE-DIMENSIONAL TOPOGRAPHY BASED ON DIRECT LASER WRITING

by

Heiskanen, S. & Maasilta, I.J.

Applied Physics Letters **117**, 232601 (2020).

Reproduced with kind permission of AIP Publishing.

https://doi.org/10.1063/5.0029273

Applied Physics Letters ARTICLE scitation.org/journal/apl

Superconducting tunnel junction fabrication on three-dimensional topography based on direct laser writing

Cite as: Appl. Phys. Lett. **117**, 232601 (2020); doi: 10.1063/5.0029273
Submitted: 11 September 2020 · Accepted: 27 November 2020 ·
Published Online: 8 December 2020

View Online Export Citation CrossMark

Samuli Heiskanen and Ilari J. Maasilta[a)]

AFFILIATIONS

Nanoscience Center, Department of Physics, University of Jyvaskyla, P. O. Box 35, FIN-40014 Jyväskylä, Finland

[a)]Author to whom correspondence should be addressed: maasilta@jyu.fi

ABSTRACT

Superconducting junctions are widely used in a multitude of applications ranging from quantum information science and sensing to solid-state cooling. Traditionally, such devices must be fabricated on flat substrates using standard lithographic techniques. In this study, we demonstrate a highly versatile method that allows for superconducting junctions to be fabricated on a more complex topography. It is based on maskless direct laser writing and two-photon lithography, which allows writing in 3D space. We show that high-quality normal metal–insulator–superconductor tunnel junctions can be fabricated on top of a 20-μm-tall three-dimensional topography. Combined with conformal resist coating methods, this technique could allow sub-micron device fabrication on almost any type of topography in the future.

Published under license by AIP Publishing. https://doi.org/10.1063/5.0029273

Superconducting tunnel junctions have many applications, for example, in sensing,[1] quantum information,[2,3] and nanoscale thermal sciences.[4] Their fabrication is done using the well-established techniques of ultraviolet photolithography or electron-beam lithography, which produce good results except for one major flaw: those methods are designed for patterning on flat 2D substrates. This is a limitation for more complex device designs, which may, in some cases, require or benefit from the junctions sitting on uneven or sloped surfaces, at the bottom of a trench, or on elevated platforms, for example, on top of a three-dimensional (3D) phononic crystal for strong thermal isolation. It is the purpose of this study to demonstrate a simple technique that facilitates such more difficult, yet high quality superconducting junction fabrication on substrates of varying topography.

As the first proof-of-principle demonstration, in this study we fabricate and characterize normal metal–insulator–superconductor (NIS) tunnel junctions[5] on complex topography. This choice is based on two reasons: (i) the electrical response of a NIS junction is a sensitive probe of the quality of the superconducting material and the insulating barrier, as it allows a direct measurement of the density of states of the superconductor, and (ii) our own immediate application is in sensitive local thermometry of complex nanoscale 3D structures. The fabrication technique is, however, perfectly suited for the fabrication of superconductor-insulator-superconductor (SIS) or superconductor-normal metal-superconductor (SNS) Josephson junctions, as well.

NIS junctions are particularly suited for low-temperature thermometry, because the current through an NIS junction has a strong temperature dependence at energies close to the superconducting gap,[4,6,7] and they can even be considered, in some cases, as primary electron thermometers.[8] Due to their sensitivity and the possibility to fabricate them in sub-micron scales, they are excellent local sensors for heat transfer measurements,[9–12] can be operated fast in microsecond time scales with a microwave readout,[13,14] and could work as the sensor element in bolometric radiation detection[15–18] or in direct measurement of temperature fluctuations.[19] Typically, the superconducting material used is Al, limiting the use of NIS devices to below 1 K. However, by using higher transition temperature superconductors, the temperature range of NIS thermometers has been extended with Nb,[20,21] NbN,[22] TaN,[23] and TiN.[24]

Other possible applications of NIS junctions are in metrology,[25,26] thermal rectification,[27] and electronic cooling,[28,29] with demonstrations of cooling of macroscopic and mesoscopic platforms,[30–32] nanoscale beams,[33,34] radiation detectors,[35] remote devices via photons,[36,37] and quantum information circuit components.[38]

In this Letter, we demonstrate high quality microscale Cu–AlO_x–Al NIS junction fabrication both on flat surfaces and on three-dimensional (3D) topography, using direct laser writing (DLW), which is a recently developed fabrication technique based on two-photon absorption (TPA), originally developed for writing arbitrary

Published under license by AIP Publishing

3D polymer structures from negative photoresists.[39–41] In contrast, here we use DLW to develop a positive photoresist without a photomask in combination with metal deposition and liftoff, as introduced in Refs. 42 and 43. Here, we show that well-behaving junction devices can be made using a two-layer nonstandard photoresist with an undercut structure, without degradation due to the used resists and processes. The junctions were fabricated both on flat substrates and, in particular, on top of a 20-μm-tall 3D platform. Such devices have not been made before, as they are difficult to make with standard lithographic techniques. Electrical characterization of the junctions demonstrates that the junction quality is high, as the standard junction theory fits the data extremely well, with a low level of excess sub-gap current. The temperature sensitivity extends to the lowest refrigerator temperatures used, demonstrating the application potential for thermometry and cooling of complex 3D device platforms.

The complex topography used is a 3D cuboid structure with an area of 100 μm × 100 μm and a height of 20 μm with sloped ramps (Fig. 1), fabricated from a negative photoresist (IP-Dip, Nanoscribe GmbH) on a nitridized Si substrate using DLW (Nanoscribe Photonic Professional), similar to the cuboid structure in Ref. 43. An additional 200 nm AlO_x capping layer was evaporated on the whole cuboid structure to strengthen it and to obtain more homogeneous and flat surfaces to increase the yield. AlO_x was chosen out of convenience, but other materials could also have been used.

The actual junction fabrication proceeds as follows: the sample is spin coated first with a bottom resist (AR-BR 5460, Allresist GmbH),

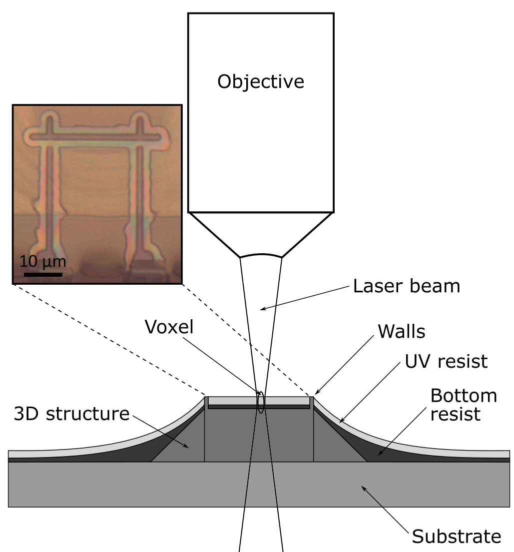

FIG. 1. Schematic of the two-photon laser exposure method used for patterning the junctions. An air-gap objective is used in order to expose from the top side of the 3D structure without being in contact with the substrate. The focus spot of the laser beam travels in 3D space, following the existing topography on the front surface, where the TPA process forms the voxel. Inset: optical micrograph of the exposed pattern on the 3D structure after development. The linewidth here is around 2.5 μm giving a junction area of 6.25 μm^2. A large ($\sim$2 μm) undercut and a bridge structure are visible.

which was diluted with propylene glycol methyl ether acetate (PGMEA) to a solid content of 9% to get a 450 nm thick film on a flat surface. This layer will allow for an undercut in the resist structure. We do not bake the bottom resist but, instead, keep it in vacuum overnight to remove the solvent. This allows for deeper undercuts and makes it possible to fabricate bridge structures for the subsequent shadow evaporation step. Then, the sample is spin coated with the UV sensitive positive-tone resist (AR-P 3540, Allresist GmbH) to a nominal thickness of 2.8 μm and baked at 100 °C for 140 s. To allow for the resists to remain on top of the cuboid structure during spinning, small vertical walls of height 3.5 μm were incorporated at the edges of the 3D platform, as shown in Figs. 1 and 2. Such walls could be left out if direct spray coating were used.[44]

The lithographic exposure of the junction geometry is done with the same Nanoscribe Photonic Professional tool (pulse rate: 80 MHz and wavelength: 780 nm) that was used for the fabrication of the topography. Because now solid resists are used (as opposed to liquid), the objective (63x, NA = 0.75) cannot be in contact with the resist, and an air gap to the sample remains, as shown in Fig. 1. A writing speed of $v = 25$ μm/s and a laser power of $P = 4$ mW were used for the exposure on top of the platform, producing a single-pass linewidth $\approx$1 μm through the whole top resist layer. The size of the voxel (line resolution) can easily be controlled with the power and speed, scaling as[43] P^2/v, with possible speeds up to a few mm/s. As the aspect ratio of the voxel is naturally high (height:width 5:1), it is straightforward to expose micrometers thick resist layers on one pass. Moreover, a large voxel height allows for significant, even micrometer scale variations of the actual resist thickness, which invariably exist when spin coating such tall topographical features. Even thicker resists can be exposed by layering the writing pattern, and this technique was used in areas near the base of the platform structure where the resist was the thickest.

In our setup, the focus of the laser cannot automatically follow the topography and thus the height changes need to be included in the

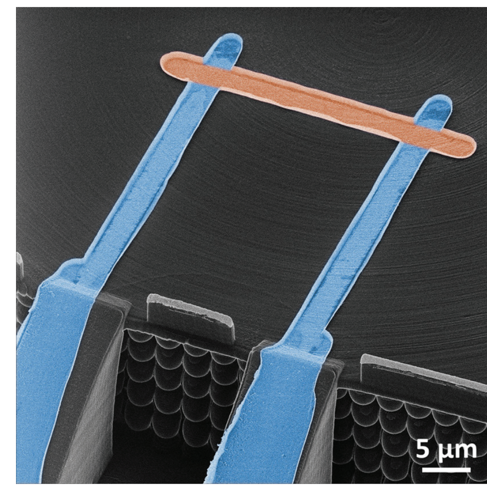

FIG. 2. False color helium ion micrograph of a finished SINIS junction on the 3D structure (blue = Al, red = Cu). For this sample, the linewidth is around 3 μm, giving a junction area of 9 μm^2.

Published under license by AIP Publishing

pattern of the laser writing path. This means that the dimensions of the topography need to be known in advance for this method. Fortunately, this information does not need to be very precise due to the size of the voxel. The alignment of the sample was done with the integrated optical microscope of the Photonic Professional tool.

After the exposure, the sample is developed in a 1:1 mixture of an AR 300–47 developer (Allresist GmbH) and de-ionized water and rinsed with de-ionized water. With the two layers of resists used, the depth of the undercut can be controlled simply with the development time. This is because the bottom resist is not exposed at all and just slowly dissolves into the developer. The development times used for our samples were around 15 s, producing a micrometer-scale undercut profile (inset, Fig. 1).

After the patterning and development, the metals are evaporated using an ultra-high vacuum electron-beam evaporator. First, a 30 nm layer of aluminum is evaporated along the patterned leads that climb the ramps. This was done from two opposing directions, in four different steps from an angle decreasing from 70° to 60° with respect to the surface normal, with the rotation axis being along the patterned line for the copper (Fig. 2). This sequence ensured better coverage over the roughness of the underlying structure. The aluminum is then thermally oxidized in 200 mbar of pure oxygen for 9 min, producing an AlO_x tunnel barrier. Finally, the sample is rotated 90° around the surface normal, and a 60 nm copper layer is evaporated similar to the aluminum, with the rotation axis for the angle evaporation now being along the Al leads (Fig. 2). Angle evaporation is also used for the copper so that no copper will land on the aluminum leads on top of the platform. After the evaporation, liftoff is done with hot acetone. A helium ion micrograph of a finished double junction SINIS device is shown in Fig. 2.

The current through a high-quality NIS junction is given by the expression

$$I = \frac{1}{2eR_T}\int_{-\infty}^{\infty} d\varepsilon N_S(\varepsilon)[f_N(\varepsilon - eV) - f_N(\varepsilon + eV)], \quad (1)$$

where R_T is the tunneling resistance of the junction, $N_S(\varepsilon)$ is the density of states of the superconductor, and f_N is the Fermi–Dirac distribution in the normal metal.[4,6] For the density of states, we use the expression taking into account non-idealities,

$$N_S(\varepsilon, T_S) = \left|\mathrm{Re}\left(\frac{\varepsilon + i\Gamma}{\sqrt{(\varepsilon + i\Gamma)^2 - \Delta^2(T_S)}}\right)\right|, \quad (2)$$

where Γ is the so-called Dynes parameter and $\Delta(T_S)$ the temperature dependent superconducting energy gap. Γ describes, in general, the non-ideal broadening of the density of states[45] due to barrier and material non-idealities. For the case of high-quality Al junctions, it was shown to result from environmentally photon-assisted tunneling events.[46]

To study the properties of NIS junctions fabricated with the DLW method, we first fabricated junctions on flat nitridized Si substrates and measured them using a ^{3}He/^{4}He dilution refrigerator with a base temperature of 60 mK. Examples of sets of I–V and dI/dV–V measurements on such a single NIS junction device with $R_T = 2$ kΩ, as a function of the bath temperature, are shown in Figs. 3(a) and 3(b). They are plotted together with theory fits based on Eqs. (1) and (2), with the electron temperature fitted but constant for each curve and Δ and R_T fitted but kept constant for the whole set. We can see that the fits are extremely good for both the I–V and the dI/dV data, demonstrating that the DLW method can produce junctions of equal quality to standard lithography.

The fitted temperatures match almost exactly the measured bath temperatures, except at the lowest temperatures, where the fitted electron temperatures are slightly higher. This is a well-known effect, caused by absorbed spurious thermal radiation from the higher temperature stages of the cryostat, in combination with the strong thermal decoupling of the electron system from the lattice at the lowest temperatures.[10,33,47] From the fits, we determined the zero temperature superconducting gap of the aluminum to be $\Delta(0) = 0.208$ meV, agreeing with previous results on a thin film Al of similar thickness deposited in the same evaporator.[33] The Dynes parameter for this device was $\Gamma/\Delta(0) = 6.5 \times 10^{-4}$, fitted using the level of the subgap current at the lowest temperature. It is roughly consistent with what has been measured in the same setup before,[33] and low enough to allow for efficient NIS cooling.[23,48] However, for this particular device, electronic cooling was not observed due to the large size of the normal metal electrode in the single junction geometry and due to the lack of normal metal quasiparticle traps contacting the Al electrode.[49]

After demonstrating that NIS junctions can be fabricated, we wanted to produce samples for our intended application, where SINIS junction pairs are needed on top of the 3D topography. Therefore, in Figs. 3(c) and 3(d), similar measurements are shown for a double junction SINIS device on top of the 3D topography (Fig. 2). This time, the fits with the simplest constant temperature model do not produce good results anymore. However, by incorporating the thermal resistance of the small normal metal island due to the electron–phonon interaction and the effect of Joule self-heating,[4,7] the fits become nearly perfect. The impact of the self-heating is particularly noticeable as the rounding of the differential conductance peaks of the lowest bath temperature data [Fig. 3(d)].

In the thermal model, described in more detail in Ref. 7, we used the usual relation[47] $P = \Sigma V(T_e^5 - T_p^5)$ for the power flow between electrons and phonons for thick metal films on bulky substrates, where V is the normal metal volume, and a typical value $\Sigma = 2 \times 10^9$ W/(K^5 m^3) for the electron–phonon coupling strength in Cu was used.[4] In addition, the modeling included the parameter $\beta = 0.25$, giving the fraction of dissipated power that back-flows from the superconducting electrodes into the normal metal.[50] This value is higher than what is typically observed ($\beta < 0.1$) for NIS junctions that are optimized for cooling,[29,33] which is expected, as we have a thin superconducting film without quasiparticle trapping.

For this SINIS junction, the Dynes parameter has a quite low value $\Gamma/\Delta(0) = 9 \times 10^{-5}$, which is much lower than for the single NIS junction sample. This improvement is most likely due to the higher value of R_T, leading to less efficient absorption of environmental radiation power and thus smaller current due to photon-assisted tunneling, as second order Andreev tunneling was estimated to be much too small to be able to explain the sub-gap current for our junction and material parameters.[51,52] Surprisingly, even with an identical oxidation recipe, R_T was always much higher for junctions on top of the structure. Possible causes are the different substrate material or the higher surface roughness, but detailed understanding is currently lacking. The superconducting gap is now $\Delta(0) = 0.181$ meV, smaller than for the simpler NIS junction but still in agreement with the literature.[53]

Published under license by AIP Publishing

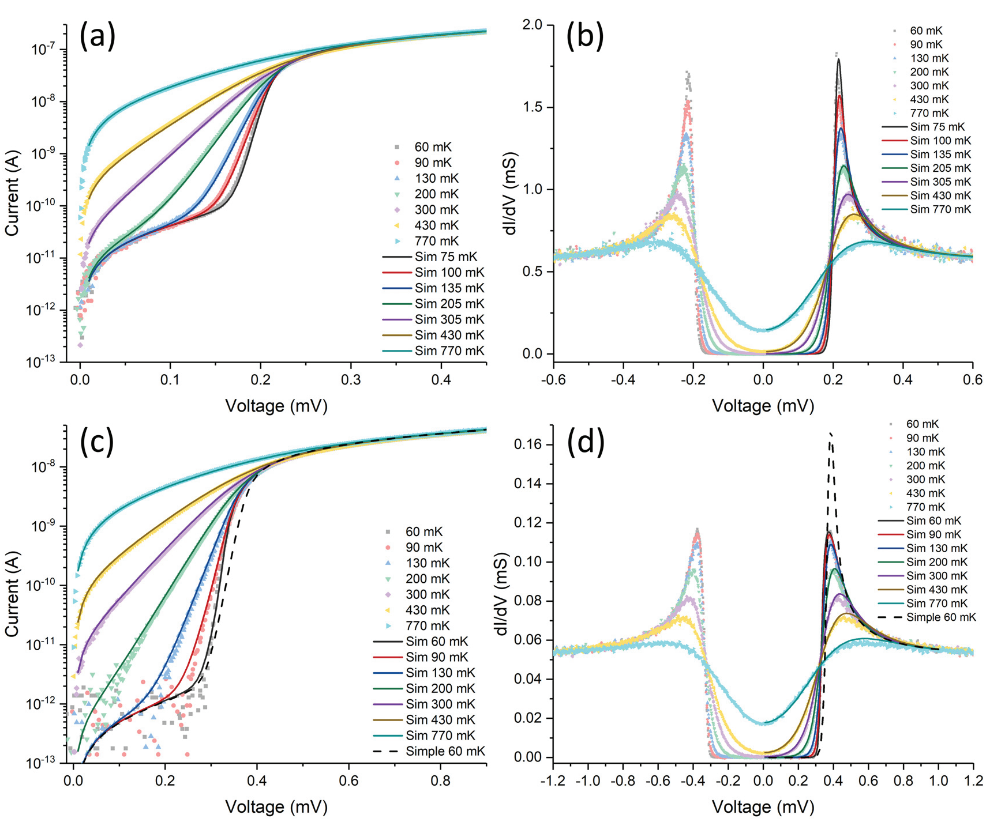

FIG. 3. The measured low-temperature (a) *I–V* and (b) *dI*/*dV–V* characteristics for the DLW fabricated NIS junctions on a flat substrate (symbols) (junction area 5 μm^2, R_T $\sim$ 2 kΩ). Theory fits to Eq. (1) and its voltage derivative are shown as lines, with the electron temperature as a fitting parameter. The experimental *dI*/*dV* data were produced by numerical differentiation of the *I–V* curve. [(c) and (d)] The same for a SINIS junction pair on top of the fabricated topography (junction area 4 μm^2, $R_{T,\mathrm{tot}}$ $\sim$ 20 kΩ). The solid lines are the theoretical results based on Eq. (1) with the thermal modeling described in the text. The dashed line shows the simple theory result of Eq. (1) with fixed *T* (no thermal model) for the data at a bath temperature of 60 m K.

In this study, the most challenging step of the process was, in fact, the resist coating. With the simple spin coating used here, we had to fabricate ramps for the wiring and additional walls to contain the resist on top of the platform topography. However, we anticipate that by using more conformal resist coating methods, such as spray coating, the fabrication could be done over almost any type of topography, with much steeper vertical gradients.

In conclusion, we have shown that direct laser writing based on two-photon lithography can be used for the fabrication of high-quality superconducting tunnel junction devices, with our case study concentrating on normal metal–insulator–superconductor (NIS) tunnel junctions. This method can be used for fast maskless fabrication over large areas down to sub-micron scales, and it is very versatile since it uses established positive photoresists and the well-known angle evaporation and liftoff techniques. Even more importantly, we have demonstrated that the method can be used for superconducting tunnel junction fabrication on highly varying 20-μm-tall 3D topography, something that has not been demonstrated with standard lithography techniques. Such fabrication opens up a multitude of possibilities to integrate superconducting devices with 3D geometries for applications in SQUID sensors, ultrasensitive radiation detectors, and quantum information processing, for example. We aim to use this method first to fabricate samples, which allow direct measurements of the thermal conductance of 3D nanostructures, which could provide better thermal isolation or thermalization for such applications.

This study was supported by the Academy of Finland Project No. 298667. We thank Mr. Zhuoran Geng for enlightening discussions and technical assistance.

DATA AVAILABILITY

The data that support the findings of this study are available from the corresponding author upon reasonable request.

REFERENCES

[1] J. Clarke and A. I. Braginski, eds., *The SQUID Handbook* (Wiley-VCH, Weinheim, 2004).

Published under license by AIP Publishing

[2] J. Clarke and F. K. Wilhelm, "Superconducting quantum bits," Nature **453**, 1031 (2008).
[3] G. Wendin, "Quantum information processing with superconducting circuits: A review," Rep. Prog. Phys. **80**, 106001 (2017).
[4] F. Giazotto, T. T. Heikkilä, A. Luukanen, A. M. Savin, and J. P. Pekola, "Opportunities for mesoscopics in thermometry and refrigeration: Physics and applications," Rev. Mod. Phys. **78**, 217–274 (2006).
[5] I. Giaever, "Energy gap in superconductors measured by electron tunneling," Phys. Rev. Lett. **5**, 147–148 (1960).
[6] P. J. Koppinen, T. Kühn, and I. J. Maasilta, "Effects of charging energy on SINIS tunnel junction thermometry," J. Low Temp. Phys. **154**, 179–189 (2009).
[7] S. Chaudhuri and I. J. Maasilta, "Cooling, conductance, and thermometric performance of nonideal normal metal-superconductor tunnel junction pairs," Phys. Rev. B **85**, 014519 (2012).
[8] A. V. Feshchenko, L. Casparis, I. M. Khaymovich, D. Maradan, O.-P. Saira, M. Palma, M. Meschke, J. P. Pekola, and D. M. Zumbühl, "Tunnel-junction thermometry down to millikelvin temperatures," Phys. Rev. Appl. **4**, 034001 (2015).
[9] M. Meschke, W. Guichard, and J. P. Pekola, "Single-mode heat conduction by photons," Nature **444**, 187–190 (2006).
[10] J. T. Karvonen and I. J. Maasilta, "Influence of phonon dimensionality on electron energy relaxation," Phys. Rev. Lett. **99**, 145503 (2007).
[11] N. Zen, T. A. Puurtinen, T. J. Isotalo, S. Chaudhuri, and I. J. Maasilta, "Engineering thermal conductance using a two-dimensional phononic crystal," Nat. Commun. **5**, 3435 (2014).
[12] Y. Tian, T. A. Puurtinen, Z. Geng, and I. J. Maasilta, "Minimizing coherent thermal conductance by controlling the periodicity of two-dimensional phononic crystals," Phys. Rev. Appl. **12**, 014008 (2019).
[13] D. R. Schmidt, K. W. Lehnert, A. M. Clark, W. D. Duncan, K. D. Irwin, N. Miller, and J. N. Ullom, "A superconductor-insulator-normal metal bolometer with microwave readout suitable for large-format arrays," Appl. Phys. Lett. **86**, 053505 (2005).
[14] S. Gasparinetti, K. L. Viisanen, O.-P. Saira, T. Faivre, M. Arzeo, M. Meschke, and J. P. Pekola, "Fast electron thermometry for ultrasensitive calorimetric detection," Phys. Rev. Appl. **3**, 014007 (2015).
[15] M. Nahum and J. M. Martinis, "Ultrasensitive-hot-electron microbolometer," Appl. Phys. Lett. **63**, 3075–3077 (1993).
[16] M. Nahum and J. M. Martinis, "Hot-electron microcalorimeters as high-resolution x-ray detectors," Appl. Phys. Lett. **66**, 3203–3205 (1995).
[17] T. T. Heikkilä, R. Ojajärvi, I. J. Maasilta, E. Strambini, F. Giazotto, and F. S. Bergeret, "Thermoelectric radiation detector based on superconductor-ferromagnet systems," Phys. Rev. Appl. **10**, 034053 (2018).
[18] L. Kuzmin, A. L. Pankratov, A. V. Gordeeva, V. O. Zbrozhek, V. A. Shamporov, L. S. Revin, A. V. Blagodatkin, S. Mas, and P. de Bernardis, "Photon-noise-limited cold-electron bolometer based on strong electron self-cooling for high-performance cosmology missions," Commun. Phys. **2**, 104 (2019).
[19] B. Karimi, F. Brange, P. Samuelsson, and J. P. Pekola, "Reaching the ultimate energy resolution of a quantum detector," Nat. Commun. **11**, 367 (2020).
[20] M. R. Nevala, S. Chaudhuri, J. Halkosaari, J. T. Karvonen, and I. J. Maasilta, "Sub-micron normal-metal/insulator/superconductor tunnel junction thermometer and cooler using Nb," Appl. Phys. Lett. **101**, 112601 (2012).
[21] J. K. Julin and I. J. Maasilta, "Applications and non-idealities of submicron Al–AlO_x–Nb tunnel junctions," Supercond. Sci. Technol. **29**, 105003 (2016).
[22] S. Chaudhuri, M. R. Nevala, and I. J. Maasilta, "Niobium nitride-based normal metal-insulator-superconductor tunnel junction microthermometer," Appl. Phys. Lett. **102**, 132601 (2013).
[23] S. Chaudhuri and I. J. Maasilta, "Superconducting tantalum nitride-based normal metal-insulator-superconductor tunnel junctions," Appl. Phys. Lett. **104**, 122601 (2014).
[24] A. Torgovkin, S. Chaudhuri, J. Malm, T. Sajavaara, and I. J. Maasilta, "Normal-metal-insulator-superconductor tunnel junction with atomic-layer-deposited titanium nitride as superconductor," IEEE Trans. Appl. Supercond. **25**, 1 (2015).
[25] J. P. Pekola, J. J. Vartiainen, M. Möttönen, O.-P. Saira, M. Meschke, and D. V. Averin, "Hybrid single-electron transistor as a source of quantized electric current," Nat. Phys. **4**, 120–124 (2008).
[26] J. P. Pekola, O.-P. Saira, V. F. Maisi, A. Kemppinen, M. Möttönen, Y. A. Pashkin, and D. V. Averin, "Single-electron current sources: Toward a refined definition of the ampere," Rev. Mod. Phys. **85**, 1421–1472 (2013).
[27] M. Martinez-Perez, A. Fornieri, and F. Giazotto, "Rectification of electronic heat current by a hybrid thermal diode," Nat. Nanotechnol. **10**, 303–307 (2015).
[28] M. Nahum, T. M. Eiles, and J. M. Martinis, "Electronic microrefrigerator based on a normal-insulator-superconductor tunnel junction," Appl. Phys. Lett. **65**, 3123–3125 (1994).
[29] J. T. Muhonen, M. Meschke, and J. P. Pekola, "Micrometre-scale refrigerators," Rep. Prog. Phys. **75**, 046501 (2012).
[30] X. Zhang, P. J. Lowell, B. L. Wilson, G. C. O'Neil, and J. N. Ullom, "Macroscopic subkelvin refrigerator employing superconducting tunnel junctions," Phys. Rev. Appl. **4**, 024006 (2015).
[31] H. Q. Nguyen, M. Meschke, and J. P. Pekola, "A robust platform cooled by superconducting electronic refrigerators," Appl. Phys. Lett. **106**, 012601 (2015).
[32] E. Mykkänen, J. S. Lehtinen, L. Grönberg, A. Shchepetov, A. V. Timofeev, D. Gunnarsson, A. Kemppinen, A. J. Manninen, and M. Prunnila, "Thermionic junction devices utilizing phonon blocking," Sci. Adv. **6**, eaax9191 (2020).
[33] P. J. Koppinen and I. J. Maasilta, "Phonon cooling of nanomechanical beams with tunnel junctions," Phys. Rev. Lett. **102**, 165502 (2009).
[34] J. T. Muhonen, A. O. Niskanen, M. Meschke, Y. A. Pashkin, J. S. Tsai, L. Sainiemi, S. Franssila, and J. P. Pekola, "Electronic cooling of a submicron-sized metallic beam," Appl. Phys. Lett. **94**, 073101 (2009).
[35] N. A. Miller, G. C. O'Neil, J. A. Beall, G. C. Hilton, K. D. Irwin, D. R. Schmidt, L. R. Vale, and J. N. Ullom, "High resolution x-ray transition-edge sensor cooled by tunnel junction refrigerators," Appl. Phys. Lett. **92**, 163501 (2008).
[36] A. V. Timofeev, M. Helle, M. Meschke, M. Möttönen, and J. P. Pekola, "Electronic refrigeration at the quantum limit," Phys. Rev. Lett. **102**, 200801 (2009).
[37] M. Partanen, K. Y. Tan, J. Govenius, R. E. Lake, M. K. Mäkelä, T. Tanttu, and M. Möttönen, "Quantum-limited heat conduction over macroscopic distances," Nat. Phys. **12**, 460–464 (2016).
[38] K. Y. Tan, M. Partanen, R. E. Lake, J. Govenius, S. Masuda, and M. Möttönen, "Quantum-circuit refrigerator," Nat. Commun. **8**, 15189 (2017).
[39] H.-B. Sun, S. Matsuo, and H. Misawa, "Three-dimensional photonic crystal structures achieved with two-photon-absorption photopolymerization of resin," Appl. Phys. Lett. **74**, 786–788 (1999).
[40] S. Kawata, H.-B. Sun, T. Tanaka, and K. Takada, "Finer features for functional microdevices," Nature **412**, 697–698 (2001).
[41] M. Deubel, G. von Freymann, M. Wegener, S. Pereira, K. Busch, and C. M. Soukoulis, "Direct laser writing of three-dimensional photonic-crystal templates for telecommunications," Nat. Mater. **3**, 444–447 (2004).
[42] A. Braun and S. A. Maier, "Versatile direct laser writing lithography technique for surface enhanced infrared spectroscopy sensors," ACS Sens. **1**, 1155–1162 (2016).
[43] S. Heiskanen, Z. Geng, J. Mastomäki, and I. J. Maasilta, "Nanofabrication on 2D and 3D topography via positive-tone direct-write laser lithography," Adv. Eng. Mater. **22**, 1901290 (2020).
[44] K. A. Cooper, C. Hamel, B. Whitney, K. Weilermann, K. J. Kramer, Y. Zhao, and H. Gentile, *Conformal Photoresist Coatings for High Aspect Ratio Features* (SUSS MicroTec Waterbury Center, Vermont, 2007).
[45] R. C. Dynes, J. P. Garno, G. B. Hertel, and T. P. Orlando, "Tunneling study of superconductivity near the metal-insulator transition," Phys. Rev. Lett. **53**, 2437–2440 (1984).
[46] J. P. Pekola, V. F. Maisi, S. Kafanov, N. Chekurov, A. Kemppinen, Y. A. Pashkin, O.-P. Saira, M. Möttönen, and J. S. Tsai, "Environment-assisted tunneling as an origin of the dynes density of states," Phys. Rev. Lett. **105**, 026803 (2010).
[47] F. C. Wellstood, C. Urbina, and J. Clarke, "Hot-electron effects in metals," Phys. Rev. B **49**, 5942–5955 (1994).
[48] J. P. Pekola, T. T. Heikkilä, A. M. Savin, J. T. Flyktman, F. Giazotto, and F. W. J. Hekking, "Limitations in cooling electrons using normal-metal-superconductor tunnel junctions," Phys. Rev. Lett. **92**, 056804 (2004).

Published under license by AIP Publishing

[49]J. P. Pekola, D. V. Anghel, T. I. Suppula, J. K. Suoknuuti, A. J. Manninen, and M. Manninen, "Trapping of quasiparticles of a nonequilibrium superconductor," Appl. Phys. Lett. **76**, 2782–2784 (2000).
[50]P. A. Fisher, J. N. Ullom, and M. Nahum, "High-power on-chip microrefrigerator based on a normal-metal/insulator/superconductor tunnel junction," Appl. Phys. Lett. **74**, 2705–2707 (1999).
[51]F. W. J. Hekking and Y. V. Nazarov, "Subgap conductivity of a superconductor–normal-metal tunnel interface," Phys. Rev. B **49**, 6847–6852 (1994).
[52]T. Faivre, D. S. Golubev, and J. P. Pekola, "Andreev current for low temperature thermometry," Appl. Phys. Lett. **106**, 182602 (2015).
[53]B. T. Matthias, T. H. Geballe, and V. B. Compton, "Superconductivity," Rev. Mod. Phys. **35**, 1–22 (1963).

Published under license by AIP Publishing

PIII

CONTROLLING THERMAL CONDUCTANCE USING THREE-DIMENSIONAL PHONONIC CRYSTALS

by

Heiskanen, S., Puurtinen, T. & Maasilta, I.J.

Submitted manuscript.

Controlling thermal conductance using three-dimensional phononic crystals

Samuli Heiskanen,[1] Tuomas Puurtinen,[1] and Ilari J. Maasilta[1, a)]
Nanoscience Center, Department of Physics, University of Jyvaskyla, P. O. Box 35, FIN-40014 Jyväskylä, Finland

(Dated: May 20, 2021)

Controlling thermal transport at the nanoscale is vital for many applications. Previously, it has been shown that this control can be achieved with periodically nanostructured two-dimensional phononic crystals, for the case of suspended devices. Here we show that thermal conductance can also be controlled with three-dimensional phononic crystals, allowing the engineering of the thermal contact of more varied devices without the need of suspension in the future. We show experimental results measured at sub-Kelvin temperatures for two different period three-dimensional crystals, as well as for a bulk control structure. The results show that the conductance can be enhanced with the phononic crystal structures in our geometry. This result cannot be fully explained by the simplest theory taking into account the coherent modification of the phonon band structure, calculated with finite element method simulations.

I. INTRODUCTION

Phononic crystals (PnC) are periodic structures which are elastic analogues of the more widely known photonic crystals[1]. Instead of a periodic dielectric constant, they have a periodic density and elasticity. This means that they can be used to manipulate how vibrational energy (sound and/or heat) flows through a material. The flow of energy can be altered due to changes introduced to the material's phononic band structure. PnC's can even produce full band gaps at specific frequencies due to Bragg interference[2,3], or due to local resonances[4,5]. Due to the ease of fabrication, early experiments focused on macroscopic structures with periods in the millimeter-scale[6]. Structures like this are typically applied in acoustic filtering, focusing or wave-guiding[4,6,7], because their dominant frequency is in the range of sonic or ultrasonic waves. Advancements in fabrication methods, like colloidal crystallization and interference lithography, allowed the fabrication of structures with micro- and nano-scale periods which have hypersonic dominant frequencies[8,9]. Such structures can be applied for example in RF communication devices[10], but also for thermal transport, as hypersonic ~ 10 GHz frequencies are dominant for thermal phonons at low temperatures.

However, not much work has been done on thermal properties of micro- and nano-scale PnC structures (for reviews, see[5,11]). This is especially the case with low temperatures studies, where coherent modification of band-structure is still operational and not destroyed by disorder[12,13]. There has been low temperature experimental studies on 2D holey PnC structures fabricated into a thin SiN film[14,15], but no such studies have been done on 3D PnCs before. Due to the difficulty of the fabrication of nano-scale 3D crystals, even some recent experiments on wave propagation have focused on macro-scale structures[16].

The control of thermal transport has become vital for several applications. There is a need to improve the heat dissipation out of semiconductor devices and better thermal isolation is needed for example in ultrasensitive bolometric radiation detectors[17]. Similarly there are plans to use PnC structures to control thermal transport in quantum bits[18]. Previously this kind of control was achieved by introducing scattering centers, such as nanoparticles or impurities, into the material[19–21]. However, it has been shown that thermal transport can also be controlled with periodic PnC structures[22–24]. It has been theoretically and experimentally demonstrated[14], that at low temperatures PnCs alter the thermal conductance of the material by the coherent modification of its phononic band structure. This was shown for 2D crystals but similar ideas can be pursued also for 3D crystals, as discussed in this study. Considering different applications, the benefit of 3D crystals is that they make the isolation of any type of device possible, while 2D crystals only allow the isolation using more fragile suspended structures.

It has been shown that self-assembly can be used for the fabrication of 3D PnCs with colloidal crystallization of mono-disperse spherical particles[9,25–27]. However, there is no easy way to integrate any measurement devices and circuitry with such crystals. There have been efforts to allow fabrication of metallic wires on these crystals by hardening the spheres with an electron beam[28], but issues still exist with the continuity of the wiring due to the cracking of the crystals and separation at the substrate interface during drying.

In this study, in contrast, 3D laser lithography is used for the crystal fabrication. The measurement devices and wiring were fabricated using a method developed for general device fabrication on high topographies, which utilizes the same 3D lithography tool, but in combination with lift-off[29]. The 3D lithography technique is based on two photon absorption, which allows fabrication of arbitrary 3D structures from negative resists[30–32], with a resolution of about 200 nm. Compared to colloidal crystallization, 3D lithography is the more versatile fab-

a) Electronic mail: maasilta@jyu.fi

rication method, which also means that devices can be integrated more easily with the 3D structures. However, we are limited to micron-scale crystal periods due to the resolution limit of the technique.

Here, we show with measurements and theoretical simulations that 3D PnC's fabricated with 3D lithography can be used to control sub-Kelvin thermal transport by orders of magnitude. We fabricated 3D simple cubic lattices of spheres to obtain 3D PnCs that support a heated platform (Fig. 1). This geometry was chosen for simplicity of fabrication and modeling. Crystals with two different lattice constants were fabricated: One with a smaller lattice constant (3.1 μm) that still resulted in a good spherical shape, and another larger period one (5.0 μm), which could still be feasibly simulated using the finite element method (FEM). The size of the crystal and the filling factor of the lattice were the same for both PnCs, which means that classical diffusive bulk scattering would give identical thermal conductances for both structures. However, our experiments show an order of magnitude difference between the two. Coherent simulations indeed predict a difference, but also a strong suppression compared to a bulk structure. Unexpectedly, for both structures, the conductance was enhanced compared to a bulk control device. The reason for this is not fully clear, but is tentatively ascribed to an improved effective boundary conductance between the heated platform and the underlying structure.

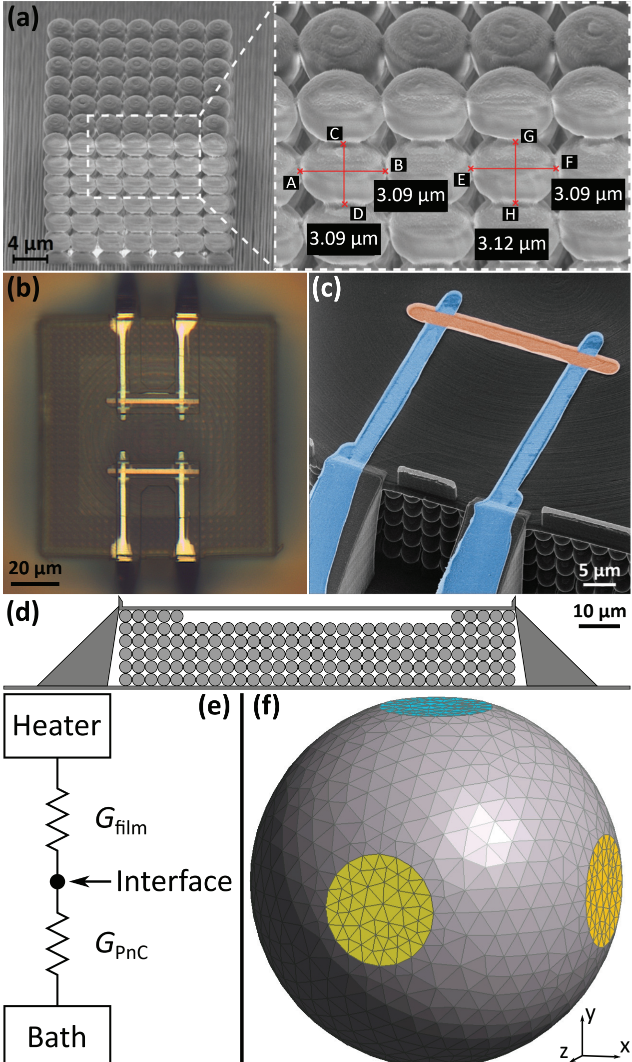

Figure 1. (a) An SEM image of the 3.1 μm PnC lattice with halved spheres at the front face. The image was taken at a 45°angle so the half spheres appear to be elliptical. (b) An optical microscope image of the finished structure from the top, including the heater and thermometer devices. (c) A false color helium ion micrograph of a finished SINIS junction pair on a PnC structure (blue=Al, red=Cu). The line width is around 3 μm on the platform, giving a 9 μm^2 junction area. (d) A schematic cross-section of the 3.1 μm PnC structure.(e) The thermal model used in the analysis. (f)The FEM mesh used in the PnC simulations. For clarity, only the surface of the unit cell is shown, the mesh extends into the sphere volume. Contact areas between neighboring spheres are shown in yellow and blue.

II. FABRICATION METHODS

The PnC structures are fabricated with a Nanoscribe Photonic Professional 3D lithography system. The 3D exposure was done with the dip-in mode where an objective is brought in direct contact with a liquid resist. For the structures in this study we used the Ip-Dip resist by Nanoscribe GmbH. After the pattern of the structure is exposed into the liquid resist, development is done in propylene glycol methyl ether acetate (PGMEA) for 20 minutes and the sample is rinsed in isopropanol (IPA). Then a post-print UV curing is done for the samples[33], which strengthens the structure and minimizes the shrinkage of the resist, as follows: Keeping the sample in solution, it is directly transferred to an IPA bath containing 0.5 wt% 2,2-dimethoxy-2-phenylacetophenone (DMPA) and then exposed to a 366 nm UV light for 20 minutes. The added DMPA acts as a photoinitiator, and thus this process increases crosslinking in the structure. Then the sample is rinsed again with IPA and dried with N_2 gas. The PnC structures are finalized by adding a 200 nm AlOx capping layer using a high vacuum electron-beam evaporator, in order to make the samples more durable for the following steps. This increased the yield considerably. The samples are baked on a hotplate at 150 °C for 20 minutes before and after the AlOx evaporation in order to relieve internal stresses and reduce cracking.

To facilitate the fabrication of a heater and a thermometer, the PnC structures have a smooth platform for them on top and ramps for measurement leads. The top layer of spheres is left out except at the edges of the platform so that it is suspended in the middle (Fig. 1d). The platform has a thickness 1.6 μm, which is well

within the 3D limit for the thermally dominant phonon modes. This geometry was chosen to reduce the direct ballistic flow of heat from the heater to the crystal, which would not create a signal at the thermometer, thus the chosen geometry makes sure that the thermometer signal is measurable. The heater and the thermometer are superconductor-insulator-normal metal-insulator-superconductor (SINIS) junction pairs fabricated opposing each other (Fig. 1b). The junction pairs are fabricated onto the middle of the platform using a fabrication method developed by us for device fabrication on 3D topographies[29]. For these samples aluminum was used as the superconductor and copper as the normal metal. The junction pairs can be used to measure the thermal conductance, by biasing one of them to work as a thermometer and then heating the film with the other junction pair[14].

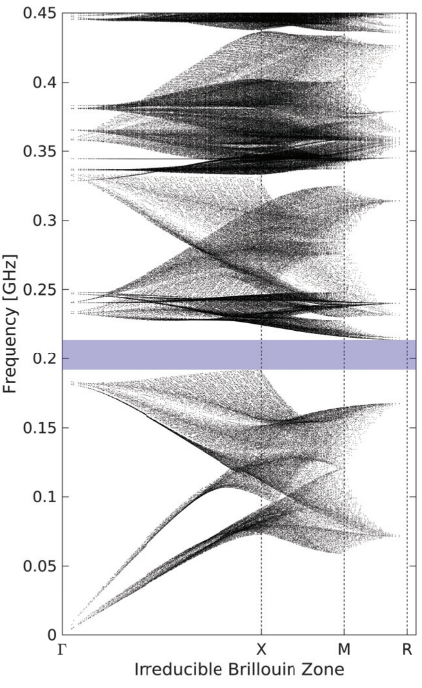

Figure 2. The lowest spectral branches $\omega(\mathbf{k})$ given by the FEM simulations for the 3.1 μm PnC. x-axis is the magnitude of the wave vector, with the distances to X,M, and R high symmetry points in the Brillouin zone marked by the vertical lines. A complete energy gap is marked in blue.

III. SIMULATION METHODS

The sample geometry for the simulations was approximated as a 3D sphere array covered by a platform [partly suspended, see Fig. (Fig.1d)] with a long rectangular heater on top of it. With the low temperatures (<1 K) used in the experiments, the flow of phonons is typically ballistic[14,34]. This means that the phonon emission is radiative and not diffusive. In the ballistic limit, the thermal conductance of the system can be calculated from the phonon emission power of the heater. The phonons emitted by the heater travel outwards in all directions inside the suspended platform. In turn, the area of the platform the overlaps with the PnC can be considered to be a large area phonon source ("secondary heater") for the underlying PnC. In principle these two parts of the sample give two contributions in series for the thermal conductance (Fig.1e). However, with the used dimensions of the samples, we calculated using Rayleigh-Lamb theory[35,36]that the thermal conductance of the platform is much higher than that of the PnC at the temperature range of the experiment 0.1 - 1 K, and does not limit the heat flow. The conductance of the platform is high, as it has essentially bulk behavior due to the softness of the material and the thickness of the platform (1.6 μm), with the 2D-3D cross-over thickness[37] $d_C = \hbar c_t/(2k_B T)$ calculated to be as low as $\sim$ 30 nm at 0.1 K for the IP-dip resist material.

With this information we can calculate the phonon emission power of the platform flowing through the underlying 3D PnC structure. Only the outward propagating phonon modes with energies $\hbar\omega_j(\mathbf{k})$ are carrying the energy, so the phonon emission power is given by the 3D version of the expression in Ref.[38]:

$$\begin{aligned} P(T) =& \frac{1}{8\pi^3}\sum_j \int_\gamma d\gamma \int_K d\mathbf{k}\hbar\omega_j(\mathbf{k})n(\omega_j,T) \\ &\times \frac{\partial\omega_j(\mathbf{k})}{\partial\mathbf{k}}\cdot\hat{\mathbf{n}}_\gamma\Theta\left(\frac{\partial\omega_j}{\partial\mathbf{k}}\cdot\hat{\mathbf{n}}_\gamma\right), \end{aligned} \tag{1}$$

where γ represents a planar rectangular phonon source surface ("secondary heater") with area A, Θ is the Heaviside step function, $\hat{\mathbf{n}}_\gamma$ is the unit normal on the heater, and the $\mathbf{k}$-integral is performed over the first 3D Brillouin zone K. Here $n(\omega,T)$ is the Bose-Einstein distribution describing the thermal occupation of the phonons and the term $\partial\omega_j/\partial\mathbf{k}$ describes the group velocity of the modes j. The only unknown in the expression is the set of dispersion relations $\omega_j = \omega_j(\mathbf{k})$, which can be calculated numerically using finite element modeling (FEM) of continuous linear elasticity theory[14]. Here we used the mesh shown in Fig. 1f to find these relations. The material parameters used for the Ip-Dip resist were[39] $\rho = 1100$ kg/m^3, $E = 2.5$ GPa and $\nu = 0.49$. A set of simulated lowest frequency relations for the shorter period PnC is shown in Fig. 2, as a function of the absolute value of the phonon wavevector.

The final simulated curves in Fig. 3 for the phonon emission power were calculated from the FEM simulated data for the platform and the PnC using the real physi-

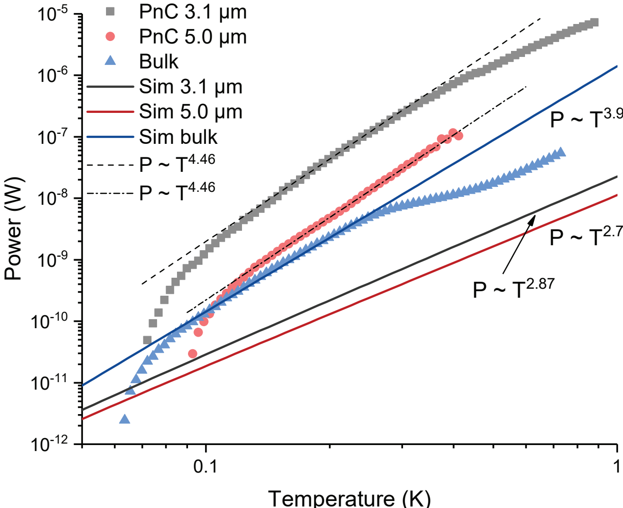

Figure 3. The results of the thermal conductance measurements presented as the measured heating power of the SINIS heater (emitted phonon power) as a function of the measured temperature on the platform (colored circles). The colored lines represent the results given by the FEM simulations for each sample, without any fitting parameters, assuming zero bath temperature for clarity. The dip at the high temperature end of the bulk data is likely caused by a non-ideality in the behaviour of the thermometer junction.

cal dimensions of the metallic heater and the horizontal contact area between the platform and the PnC, or in the case of the bulk reference sample, the vertical contact area between then platform and the bulk support (smaller). A series thermal resistance model was used (platform + PnC or bulk support, Fig.1e), with the temperature at the interface calculated by setting the power flowing through the platform and the PnC (bulk) to be equal. For simplicity, zero bath temperature was assumed. This modeling confirmed our earlier assertion that for the PnC samples, the coherent ballistic thermal conductance is expected fully limited by the PnC itself, as the platform-PnC interface and SINIS heater temperatures were very close to equal.

IV. THERMAL CONDUCTANCE MEASUREMENT AND SIMULATION RESULTS

The thermal conductance of the fabricated structures was measured at sub-Kelvin temperatures utilizing a ^{3}He/^{4}He dilution refrigerator. These measurements were made for the two different simple cubic PnC structures with lattice constants 3.1 μm and 5.0 μm, and also for a bulk sample with otherwise identical geometry, except that the PnC structure was substituted by bulk resist. The measurements were done by first calibrating one of the SINIS junction pairs to work as a thermometer, by measuring the response as a function of varying refrigerator (bath) temperature. The thermal conductance experiment was then performed by Joule heating the second SINIS device, and simultaneously measuring the temperature of the platform and the dissipated power from $P = IV$. The heating was done with a very slowly sweeping power to maintain quasi-equilibrium. The results of these measurements are shown in Fig. 3 together with the results from the FEM simulations.

From the measurements it is clear that the PnC structures did alter the thermal conductance of the material very strongly, as there is a large difference to the bulk result, and even between the two PnC structures. This also proves that the transport is mostly ballistic, as diffusive FEM calculations based on Fourier theory showed identical results with all three geometries (limited by the platform). Also, it is noticeable that the ballistic modeling explains the bulk results surprisingly well, without any fitting parameters. The observed temperature exponent of the bulk device is the expected $P \sim T^4$ for 3D ballistic conduction.

However, the data for the PnC devices deviated very strongly from the modeling. As can be seen in Fig. 3 the coherent modeling predicts that the PnCs should decrease the thermal conductance, by about an order of magnitude, whereas the measurement shows a puzzling *increase*, up to an order of magnitude for the smaller period. In addition, the observed temperature exponent for the PnC devices, $P \sim T^{4.5}$ does not agree with the coherent modeling result, where a much weaker power law is expected. Very little is currently understood of this surprising enhancement. We speculate that it may have to do with thermal boundary resistance physics between a PnC and a solid structure, which has not been studied at all, and is therefore not understood yet.

V. CONCLUSIONS

We have shown that 3D direct-laser-write two-photon lithography is a viable method for the fabrication of 3D phononic crystal structures for the hypersonic frequency range, which allows applications in thermal sciences. The strength of the method is not only in the fact that it can be used to produce complex 3D crystal structures; the same techniques can also be used for the fabrication of measurement devices on the crystals. The reported sub-Kelvin temperature range thermal conductance experiments showed large, up to an order of magnitude differences between the phononic crystal results and an otherwise identical bulk sample, demonstrating the potential for controlling thermal transport using 3D structures. However, the simplest FEM simulations based on the picture of fully coherent modification of the phononic band structure did not capture the essential features of the data. In particular, the used modeling predicts a reduction, whereas the experiments demonstrated a large enhancement of thermal conductance. This surprising enhancement is not understood yet.

ACKNOWLEDGMENTS

This study was supported by the Academy of Finland project number 298667. Technical support by Zhuoran Geng is acknowledged.

DATA AVAILABILITY

The data that support the findings of this study are available from the corresponding author upon reasonable request.

REFERENCES

[1] J. D. Joannopoulos, S. G. Johnson, J. N. Winn, and R. D. Meade, *Photonic crystals, molding the flow of light* (Princeton University Press, 2008).
[2] M. S. Kushwaha, P. Halevi, L. Dobrzynski, and B. Djafari-Rouhani, "Acoustic band structure of periodic elastic composites," Phys. Rev. Lett. **71**, 2022–2025 (1993).
[3] M. Sigalas and E. Economou, "Band structure of elastic waves in two dimensional systems," Solid State Communications **86**, 141 – 143 (1993).
[4] Y. Pennec, J. O. Vasseur, B. Djafari-Rouhani, L. Dobrzyński, and P. A. Deymier, "Two-dimensional phononic crystals: Examples and applications," Surface Science Reports **65**, 229–291 (2010).
[5] M. Sledzinska, B. Graczykowski, J. Maire, E. Chavez-Angel, C. M. Sotomayor-Torres, and F. Alzina, "2d phononic crystals: Progress and prospects in hypersound and thermal transport engineering," Advanced Functional Materials **30**, 1904434 (2020).
[6] S. Yang, J. H. Page, Z. Liu, M. L. Cowan, C. T. Chan, and P. Sheng, "Focusing of sound in a 3d phononic crystal," Phys. Rev. Lett. **93**, 024301 (2004).
[7] S. Tol, F. Degertekin, and A. Erturk, "3d-printed phononic crystal lens for elastic wave focusing and energy harvesting," Additive Manufacturing **29**, 100780 (2019).
[8] T. Gorishnyy, C. K. Ullal, M. Maldovan, G. Fytas, and E. L. Thomas, "Hypersonic phononic crystals," Phys. Rev. Lett. **94**, 115501 (2005).
[9] W. Cheng, J. Wang, U. Jonas, G. Fytas, and N. Stefanou, "Observation and tuning of hypersonic bandgaps in colloidal crystals," Nature materials **5**, 830–836 (2006).
[10] R. H. Olsson III and I. El-Kady, "Microfabricated phononic crystal devices and applications," Measurement science and technology **20**, 012002 (2008).
[11] M. Maldovan, "Phonon wave interference and thermal bandgap materials," Nature materials **14**, 667–674 (2015).
[12] M. R. Wagner, B. Graczykowski, J. S. Reparaz, A. E. Sachat, M. Sledzinska, F. Alzina, and C. M. S. Torres, "2d phononic crystals: Disorder matters," Nano Lett. **16**, 5661 (2016).
[13] J. Maire, R. Anufriev, R. Yanagisawa, A. Ramiere, S. Volz, and M. Nomura, "Heat conduction tuning by wave nature of phonons," Science Advances **3**, e1700027 (2017).
[14] N. Zen, T. A. Puurtinen, T. J. Isotalo, S. Chaudhuri, and I. J. Maasilta, "Engineering thermal conductance using a two-dimensional phononic crystal," Nature Communications **5**, 3435 (2014).
[15] Y. Tian, T. A. Puurtinen, Z. Geng, and I. J. Maasilta, "Minimizing coherent thermal conductance by controlling the periodicity of two-dimensional phononic crystals," Physical Review Applied **12**, 014008 (2019).
[16] L. D'Alessandro, E. Belloni, R. Ardito, A. Corigliano, and F. Braghin, "Modeling and experimental verification of an ultra-wide bandgap in 3d phononic crystal," Applied Physics Letters **109**, 221907 (2016).
[17] E. Ch. Enss, *Cryogenic particle detection* (Springer, Berlin, 2005).
[18] A. N. Bolgar, D. D. Kirichenko, R. S. Shaikhaidarov, S. V. Sanduleanu, A. V. Semenov, A. Y. Dmitriev, and O. V. Astafiev, "A phononic crystal coupled to a transmission line via an artificial atom," Communications Physics **3**, 1–6 (2020).
[19] W. Kim, J. Zide, A. Gossard, D. Klenov, S. Stemmer, A. Shakouri, and A. Majumdar, "Thermal conductivity reduction and thermoelectric figure of merit increase by embedding nanoparticles in crystalline semiconductors," Physical review letters **96**, 045901 (2006).
[20] D. G. Cahill, P. V. Braun, G. Chen, D. R. Clarke, S. Fan, K. E. Goodson, P. Keblinski, W. P. King, G. D. Mahan, A. Majumdar, H. J. Maris, S. R. Phillpot, E. Pop, and L. Shi, "Nanoscale thermal transport. ii. 2003-2012," Applied Physics Reviews **1**, 011305 (2014).
[21] B. S. Lee and J. S. Lee, "Thermal conductivity reduction in graphene with silicon impurity," Applied Physics A **121**, 1193–1202 (2015).
[22] J.-K. Yu, S. Mitrovic, D. Tham, J. Varghese, and J. R. Heath, "Reduction of thermal conductivity in phononic nanomesh structures," Nature nanotechnology **5**, 718–721 (2010).
[23] P. E. Hopkins, C. M. Reinke, M. F. Su, R. H. Olsson III, E. A. Shaner, Z. C. Leseman, J. R. Serrano, L. M. Phinney, and I. El-Kady, "Reduction in the thermal conductivity of single crystalline silicon by phononic crystal patterning," Nano letters **11**, 107–112 (2011).
[24] R. Anufriev, J. Maire, and M. Nomura, "Reduction of thermal conductivity by surface scattering of phonons in periodic silicon nanostructures," Physical Review B **93**, 045411 (2016).
[25] P. Jiang, J. F. Bertone, K. S. Hwang, and V. L. Colvin, "Single-crystal colloidal multilayers of controlled thickness," Chem. Mater. **11**, 2132 (1999).
[26] T. J. Isotalo, Y. L. Tian, and I. J. Maasilta, "Fabrication and modelling of three-dimensional sub-kelvin phononic crystals," Journal of Physics: Conference Series **400**, 052007 (2012).
[27] T. J. Isotalo, Y. Tian, M. P. Konttinen, and I. J. Maasilta, "Statistical characterization of self-assembled colloidal crystals by single-step vertical deposition," Colloids and Surfaces A: Physicochemical and Engineering Aspects **443**, 164–170 (2014).
[28] Y. Tian, T. J. Isotalo, M. P. Konttinen, J. Li, S. Heiskanen, Z. Geng, and I. J. Maasilta, "Integrating metallic wiring with three-dimensional polystyrene colloidal crystals using electron-beam lithography and three-dimensional laser lithography," Journal of Physics D: Applied Physics **50**, 055302 (2017).
[29] S. Heiskanen and I. J. Maasilta, "Superconducting tunnel junction fabrication on three-dimensional topography based on direct laser writing," Applied Physics Letters **117**, 232601 (2020).
[30] H. Sun, S. Matsuo, and H. Misawa, "Three-dimensional photonic crystal structures achieved with two-photon-absorption photopolymerization of resin," Applied Physics Letters **74**, 786–788 (1999).
[31] M. Deubel, G. von Freymann, M. Wegener, S. Pereira, K. Busch, and C. M. Soukoulis, "Direct laser writing of three-dimensional photonic-crystal templates for telecommunications," Nature Materials **3**, 444–447 (2004).
[32] S. Kawata, H. Sun, T. Tanaka, and K. Takada, "Finer features for functional microdevices," Nature (London) **412**, 697–698 (2001).
[33] J. S. Oakdale, J. Ye, W. L. Smith, and J. Biener, "Post-print uv curing method for improving the mechanical properties of prototypes derived from two-photon lithography," Opt. Express **24**, 27077–27086 (2016).
[34] I. J. Maasilta, T. A. Puurtinen, Y. Tian, and Z. Geng, "Phononic thermal conduction engineering for bolometers: From phononic crystals to radial casimir limit," Journal of Low Temperature Physics **184**, 211 (2016).

[35]K. F. Graff, *Wave motion in elastic solids* (Oxford University Press, 1975).
[36]T. Kühn, D. V. Anghel, J. P. Pekola, M. Manninen, and Y. M. Galperin, "Heat transport in ultrathin dielectric membranes and bridges," Phys. Rev. B **70**, 125425 (2004).
[37]T. Kühn and I. J. Maasilta, "Maximizing phonon thermal conductance for ballistic membranes," Journal of Physics: Conference Series **92**, 012082 (2007).
[38]T. A. Puurtinen and I. J. Maasilta, "Low-temperature coherent thermal conduction in thin phononic crystal membranes," Crystals **6**, 72 (2016).
[39]E. D. Lemma, F. Rizzi, T. Dattoma, B. Spagnolo, L. Sileo, A. Qualtieri, M. De Vittorio, and F. Pisanello, "Mechanical properties tunability of three-dimensional polymeric structures in two-photon lithography," IEEE transactions on nanotechnology **16**, 23–31 (2016).

PIV

INTEGRATING METALLIC WIRING WITH THREE-DIMENSIONAL POLYSTYRENE COLLOIDAL CRYSTALS USING ELECTRON-BEAM LITHOGRAPHY AND THREE-DIMENSIONAL LASER LITHOGRAPHY

by

Tian, Y., Isotalo, T.J., Konttinen, M.P., Li, J., Heiskanen, S., Geng, Z. & Maasilta, I.J.

J. Phys. D: Appl. Phys. **50**, 055302 (2017).

Reproduced with kind permission of IOP Publishing.

https://doi.org/10.1088/1361-6463/aa5004

Intregrating metallic wiring with three-dimensional polystyrene colloidal crystals using electron-beam lithography and three-dimensional laser lithography

Yaolan Tian, Tero J. Isotalo†, Mikko P. Konttinen, Jiawei Li, Samuli Heiskanen, Zhuoran Geng and Ilari J. Maasilta

E-mail: maasilta@jyu.fi
Nanoscience Center, Department of Physics, University of Jyvaskyla, P.O. Box 35, FI-40014 Jyväskylä, Finland

Abstract. We demonstrate a method to fabricate narrow, down to a few micron wide metallic leads on top of a three-dimensional colloidal crystal self-assembled from polystyrene (PS) nanospheres of diameter 260 nm, using electron-beam lithography. This fabrication is not straightforward due to the fact that PS nanospheres cannot usually survive the harsh chemical treatments required in the development and lift-off steps of electron-beam lithography. We solve this problem by increasing the chemical resistance of the PS nanospheres using an additional electron-beam irradiation step, which allows the spheres to retain their shape and their self-assembled structure, even after baking to a temperature of 160 degrees C, the exposure to the resist developer and the exposure to acetone, all of which are required for the electron-beam lithography step. Moreover, we show that by depositing an aluminum oxide capping layer on top of the colloidal crystal after the e-beam irradiation, the surface is smooth enough so that continuous metal wiring can be deposited by the electron-beam lithography. Finally, we also demonstrate a way to self-assemble PS colloidal crystals into a microscale container, which was fabricated using direct-write three-dimensional laser-lithography. Metallic wiring was also successfully integrated with the combination of a container structure and a PS colloidal crystal. Our goal is to make a device for studies of thermal transport in 3D phononic crystals, but other phononic or photonic crystal applications could also be envisioned. *Keywords*: self-assembly, colloidal crystal, cross-linking, electron-beam lithography, three-dimensional lithography, phononic crystal, photonic crystal

PACS numbers: 81.16.Dn, 81.16.Nd, 82.70.Dd, 65.80.-g

† Present address: Murata Electronics Oy

1. Introduction

Colloidal crystallization of mono-disperse sub-micron spherical particles has been used successfully for years in the fabrication of three-dimensional (3D) photonic crystals [1, 2] for a wide variety of applications [3, 4, 5, 6]. Another emerging application for 3D colloidal crystals is the engineering of phonon band-structures in phononic crystals (PnC), which have potential applications for example in engineering thermal conductance[7, 8] and controlling hypersonic elastic waves [6, 9]. So far, however, most of the work of the thermal conductance engineering has only been performed in lower dimensionalities, focusing mostly on the 2D hole array geometry either at room temperature [10, 11, 12] or at low-temperatures [13, 14, 15, 16]. One reason for this is that to perform thermal conductance experiments, metallic heater and thermometer structures are typically needed, and these structures need to be integrated with the actual phononic crystal structure. This wiring fabrication is typically done by lithographic means, and it is much easier to do this extra lithography step for 2D phononic crystal structures.

Integrating the metallic heaters and thermometers onto a 3D colloidal crystal surface poses several fabrication challenges, some of which we address in this study. Specifically, in this study we solve the following three problems: (i) Degradation and destruction of polymer colloidal particles due to harsh chemicals and heat, (ii) Deposition of continuous wires on the rough colloidal crystal surfaces, and (iii) Routing of the wiring onto a single crystalline domain of the colloidal crystal film. The first problem is especially severe for polymer colloids, such as polystyrene (PS), which are chemically close to the resists used in photo- and electron-beam lithography.

The first problem is solved by a highly controllable and simple method for protecting the PS spheres from chemical attack and melting, by cross-linking the PS spheres using high doses of electron-beam irradiation [17, 18]. As this irradiation is performed in an electron-beam lithography system, the irradiation area can be controlled to be an arbitrary shape, with minimum lateral dimensions limited by the typical e-beam lithography resolution limits to below 100 nm resolution. Combined with the deposition of an aluminum oxide (AlOx) capping layer to smooth the rough colloidal crystal surface, we successfully fabricated lithographically patterned micron-scale narrow metallic wires on top of polystyrene colloidal crystals with a particle diameter 260 nm. Finally, we demonstrate a novel way to fabricate a template for the colloidal crystal in the shape of a box from a photosensitive polymer, which was patterned directly using 3D laser writing and two-photon polymerization [19]. PS colloidal crystals were deposited inside this template box in such a way that metal leads for thermometry and heaters can be routed onto a thick ($\sim 10-20\mu$m) colloidal crystal domain from the surface of the substrate, without having to cross any cracks in the crystals that typically are generated in the vertical deposition self-assembly process of the colloidal crystal [20, 1, 21, 22, 23].

2. Self-assembly of polystyrene colloidal crystals

We have produced self-assembled colloidal crystals from polystyrene (PS) nanospheres of diameter 260 nm on silicon substrates.We used the vertical deposition method [1, 21, 22, 23], where the substrate was dipped into a 1-10 % aqueous solution of PS spheres, and was withdrawn slowly with speed typically ranging between 0.01 - 0.04 mm/min [20]. The colloidal crystal film thickness and domain size could be controlled with the dipping speed and solution concentration, reaching values up to 20 μm for the thickness and $\sim 300\mu$m for both the vertical and horizontal directions of the domain size [20]. By domains we mean regions of the crystal surrounded by cracks that form in the drying process. These cracks are of course a serious issue for further lithographic patterning of wires on top, as they can be several micrometers wide.

The substrates used in most of the experiments were single crystal silicon chips, with a silicon nitride (SiN_x) insulator layer, and a thin layer of titanium oxide (TiO_x) approximately 10 nm thick on top of the SiN_x, deposited by electron beam evaporation of Ti and room temperature oxidization in a vacuum chamber at 100 mbar of oxygen pressure for 2 minutes. The TiO_x layer provided a hydrophilic surface for improved wetting by the nano-sphere solution [24]. In the experiments with fabricated polymer template boxes, glass slides were used as the substrate, because the laser writing was performed through the substrate.

3. Controlling the chemical resistance of a polystyrene colloidal crystal by electron-beam irradiation

Many of the processes used in standard lithographic techniques involved are known to partially damage or completely destroy PS spheres. Specifically, the baking of electron-beam resists occurs at temperatures above the normal glass transition of polystyrene, thus destroying the spherical shape. Additionally, the acetone used in the standard lift-off of evaporated metals will very quickly dissolve polystyrene.

Here, we examine how electron-beam exposure affects the solubility and glass transition of colloidal crystals of 260 nm diameter PS spheres. It is known that UV [25, 26, 27] and e-beam exposure [17, 28] cause cross-linking in polystyrene, increasing the glass transition and chemical resistance [17, 18]. E-beam cross-linking was chosen here over UV for a couple of reasons: electron beams are easily controlled for patterning without masks, and their penetration into the polymer layers is stronger that that of UV. This is very important in our application, where 10-20 μm thick colloidal crystals need to be cross-linked. UV light will not penetrate deep enough in this case.

3.1. Process steps for the e-beam irradiation studies

The process of deposition of the PS spheres and their exposure by an electron beam is schematically shown in Fig. 1 (a).

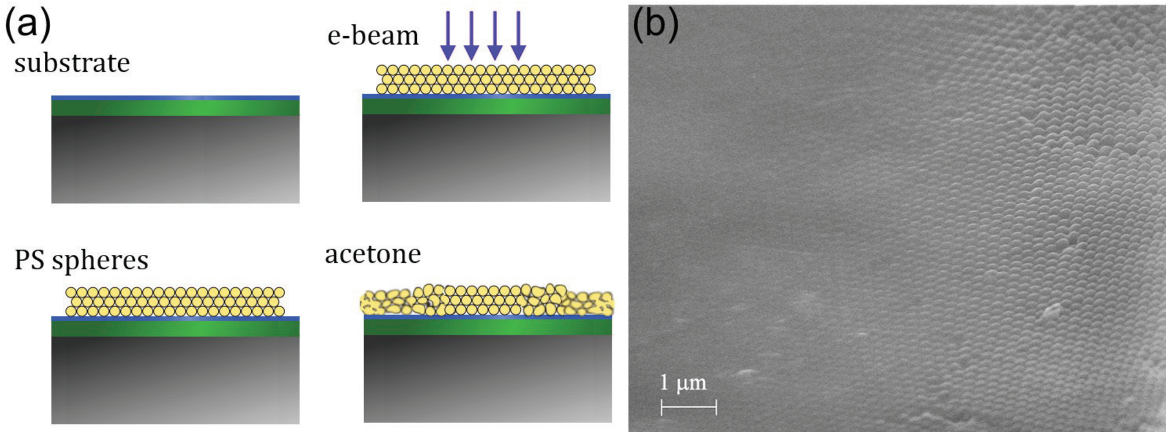

Figure 1: (a) The process steps for electron beam hardening of PS sphere colloidal crystals. Hydrophilic substrate is coated by spheres with vertical dipping, PS spheres are selectively cross-linked by an electron beam exposure, then sample is submerged in acetone for 5 minutes, to check the solubility. (b) An SEM micrograph of a vertical edge of an e-beam exposure area, showing a gradient of dissolution after an immersion into acetone.

A Si substrate with a TiOx surface layer (size $\sim$ 1 cm $\times$1 cm) was coated everywhere with a colloidal crystal of 260 nm diameter PS spheres by vertical deposition [20], with a speed 0.04 mm/min from a concentration of 5 %, resulting in a few layer thick colloidal crystal. The electron beam exposure was carried out in vacuum, using a JEOL JSM-840A scanning electron microscope operated at an acceleration voltage of 30 kV. All exposures were performed at 600 X magnification, resulting in exposed areas with dimensions 230 μm x 160 μm. The beam current was varied from 75 pA to 0.4 μA, with the exposure time kept constant at 5 minutes. Thus, the area dose ranged from 60 $\mu C/cm^2$ to 326 000 $\mu C/cm^2$. Exposed samples were then immersed in acetone for several minutes. For high enough doses, the spheres in the exposed areas were seen to be protected from dissolution in acetone, while in the surrounding areas they were dissolved and formed a bulk PS film after drying, as seen in Figure 1 (b). There is also a clear, continuous gradient of the deformation of the spheres around the edge of the irradiation area, several microns long.

3.2. Results on the increase of chemical resistivity of the PS colloidal crystals by electron-beam irradiation

The samples treated by e-beam cross-linking were inspected by scanning electron microscopy (SEM). A large, continuous range of solubility in acetone was seen as a function of the exposure dose. That is already evident in Fig. Figure 1 (b) as a spatial gradient of the dissolution around the edge of the irradiation area. SEM images were taken of each sample at several locations to ensure the results were consistent across the surface. Qualitative characterization was made by observing the degree to which the

PS spheres were dissolved by the acetone at a given exposure dose.

We discovered that below the exposure dose $\sim$ 2300 μC/cm^2, there was a range of doses where the solubility was highly controllable (Figs. 2 and 3). A lower critical dose for inducing chemical resistance to acetone was found to lie between 60 μC/cm^2 and 170 μC/cm^2, consistent with previous studies on bulk PS films [17]. The 1-2 layer thick samples exposed to 60 μC/cm^2 are seen in Figure 2 (a) (left) to dissolve completely in acetone, while those exposed with 170 μC/cm^2 Figure 2 (a) (right) exhibited some signs of spherical structures remaining within the dissolved mass.

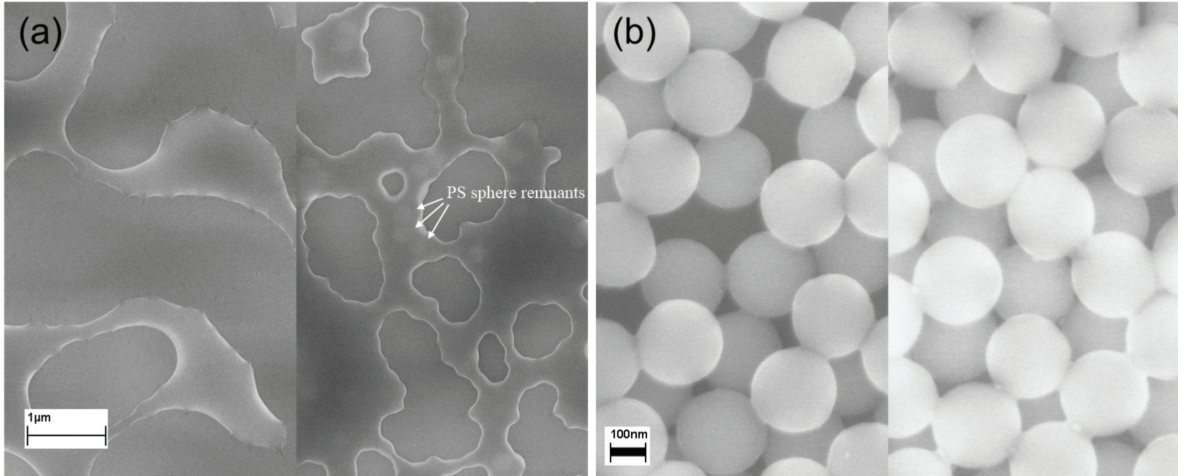

Figure 2: (a) PS spheres after e-beam exposure and acetone bath are shown for a dose of 60 μC/cm^2 (left) and 170 μC/cm^2 (right). Some PS sphere remnants can be seen within the dissolved mass on the right, while spheres are completely dissolved at the lower exposure dose on the left. Scale bar is 1 μm. (b) PS spheres after e-beam exposure and acetone bath are shown for a dose of 2285 μC/cm^2 (left) and 36850 μC/cm^2 (right). Solubility in both cases is negligible. Scale bar in black is 100 nm.

At a dose of $\sim$2200 μC/cm^2 and above, the solubility of the PS spheres in acetone was negligible. Figure 2 (b) shows a comparison between PS spheres given a dose of 2285 μC/cm^2 (left) and 36850 μC/cm^2 (right), exposed to acetone for 5 minutes. The spheres have clearly retained their original shape to a high degree, and we can state with confidence that both samples are effectively resistant against solubility.

Based on Fig. 2, it is worth while to study in more detail what happens with doses between 170 μC/cm^2 and 2285 μC/cm^2. Figure 3 shows the SEM images of samples exposed in this intermediate regime. We see that increasing the dose resulted in a controllable and gradual increase of the chemical resistivity in acetone. This range is large enough to allow precise tuning of the selected dose. There is even evidence that one has some control over the formation of narrow neck connections between individual PS spheres (at doses between 475 μC/cm^2 and 1225 μC/cm^2). The narrow necks can be extremely narrow, for example for the dose 1225 μC/cm^2 they are only $\sim$ 5 nm wide.

Although the acetone resistance studies in Figs. 1 - 3 were performed with thin

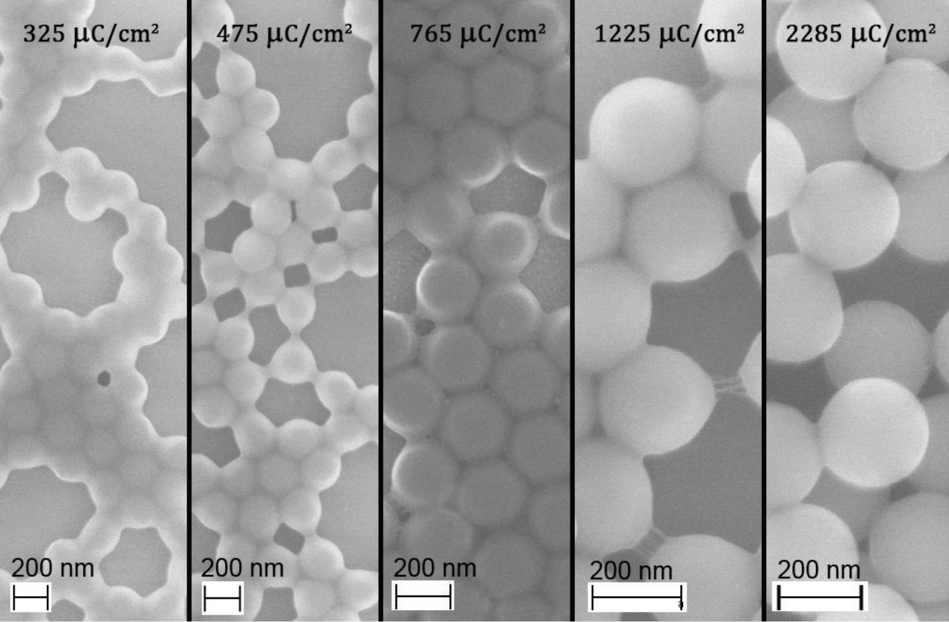

Figure 3: PS spheres after e-beam exposure and acetone bath are shown for doses ranging from 325 μC/cm^2 to 2285 μC/cm^2 (left to right). A highly tunable resistance to dissolution in acetone is seen.

1-2 layer colloidal crystals, we have also performed successful e-beam irradiations with doses above $\sim 1000\mu$C/cm^2 on much thicker crystals, up to 20 layers thick ($\sim 4\mu$m). For crystals thicker than that, we typically observed that the whole crystal peeled off from the substrate after irradiation. However, later in section 5 we show a templating method, with which the thickness could be increased to $\sim 10\mu$m without peel-off after irradiation.

4. Lithography on colloidal crystal surfaces

Lithographic testing was performed using two types of samples, both given cross-linking area doses of $\sim$ 24000 μC/cm^2 and immersed first in acetone for 5 minutes to check that no dissolution resulted. One set of samples were then spin coated with three layers of electron-beam resists baked at 70 °C for 5 minutes after each layer. The resist layers were spun coated onto the colloidal crystal, with spin speeds corresponding to nominal thicknesses on bare substrates of one 400 nm layer of copolymer poly(methyl methacrylate-methacrylic acid) [P(MMA-MAA)], and two layers of 200 nm poly(methyl methacrylate) (PMMA), giving a nominal total thickness 800 nm. This type of multilayer resist was used to help with the lift-off step, as it created an undercut structure. Another colloidal crystal sample set was first coated with AlO_x layer of thickness $\sim$ 100 nm by electron beam evaporation, using a rotating sample stage and angle evaporation from 70 degrees, before the spin coating with the three resist layers. A schematic for the second method using the AlOx capping is shown in Figure 4. After

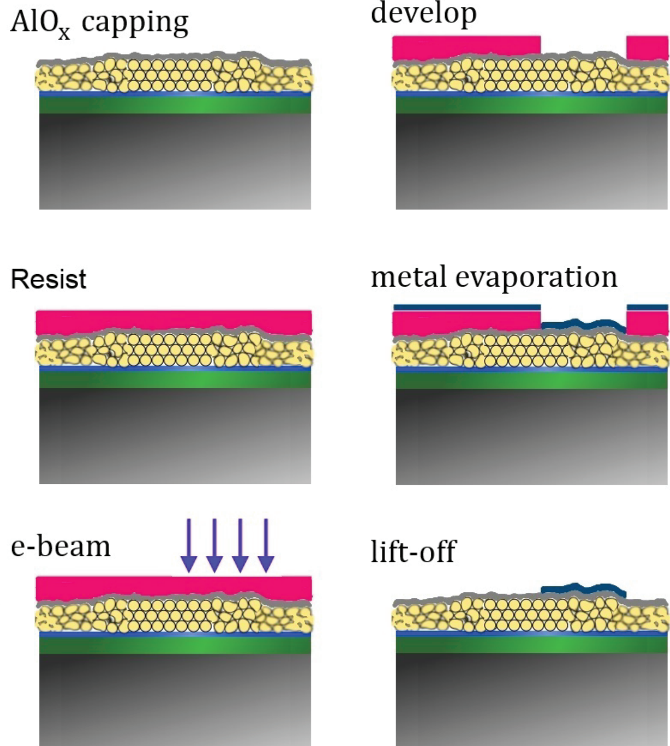

Figure 4: Process steps are shown for lithography on PS sphere colloidal crystal surface. AlO_x capping layer is e-beam evaporated on colloidal crystal sample, PMMA+P(MMA-MAA) three-layer resist is spin coated, e-beam pattern is exposed and then developed, metal is evaporated and lift-off is performed.

the e-beam resist coating, a lithographic pattern was exposed using a Raith e-LiNE tool with a 20 kV electron beam, developed in MIBK:IPA (1:3) solution for 60 seconds, rinsed in IPA for 15 – 30 seconds and dried under nitrogen flow. The developed samples were then coated with 40 nm to 80 nm of aluminum (Al) by electron beam evaporation in ultra-high vacuum, evaporated perpendicular to the substrate, and finally the metal lift-off was performed by placing samples in cold acetone for 30 minutes and then applying a mildly turbulent flow from a syringe.

For lithographic testing purposes, simple aluminum wires were deposited by the above electron beam evaporation and lift-off steps, with patterns of varying line width and typical film thickess 40-80 nm.

It was found that lithography without the AlO_x capping layer was possible, but produced inconsistent results. It seemed that the thickness of e-beam resist was notably less on the colloidal crystal surface than on a plain surface. On the PS sphere surface, a minimum of three layers of electron-beam resist was necessary to cover the self-assembled crystal surface. This may be due to resist penetration into the spaces between spheres, as well as inhomogeneous spreading over different heights of the PS sphere structures. Even with the increased resist thickness, the sharpness of lithographic structures was

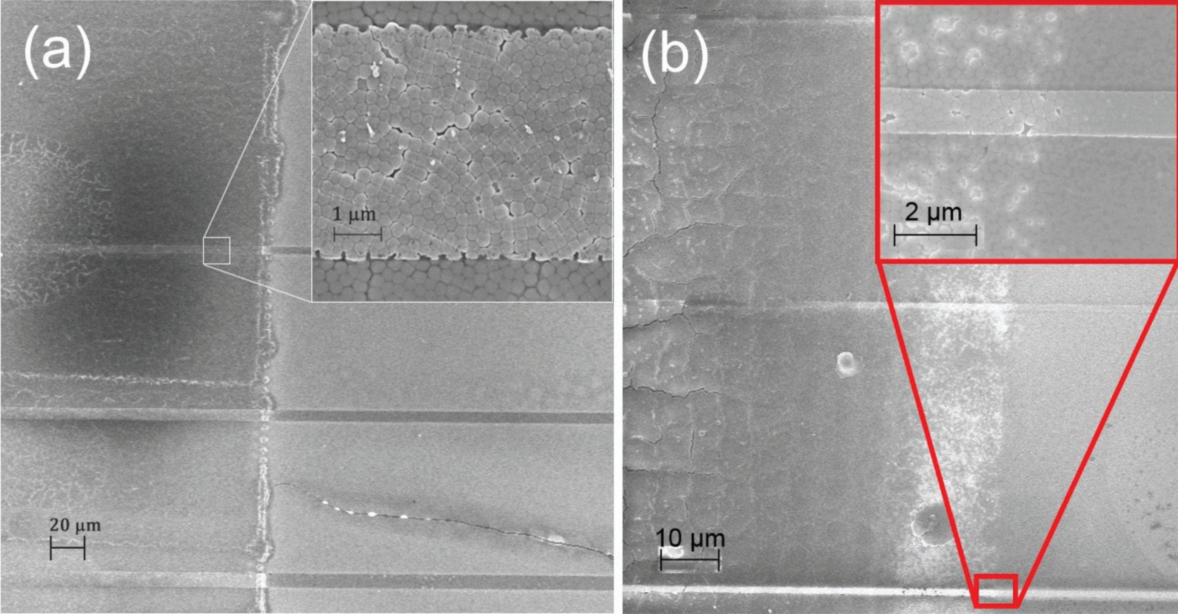

Figure 5: SEM imaging of Al wires deposited by electron beam evaporation is on top of a hardened PS sphere colloidal crystal with an AlO_x capping layer. (a) Wire widths ranging from 5 to 10 μm. (b) Wire widths around 1 μm. The roughness of the metal wire edge (insets) is seen to be less than the sphere size.

reduced compared to patterns made on plain substrates without PS spheres. Thus, a capping layer was needed to minimize the penetration of the resists into the crystal structure, and to smooth the top surface of the crystal.

Using a 100 nm thick evaporated AlO_x capping layer, we were able to produce continuous and conducting metal wires a few hundred μm in length and as narrow as one μm (Figure 5). Roughness at the edges of the wires, as seen in the insets in Figure 5, was found to be low enough to suggest the possibility of producing wires approaching the diameter of PS spheres. While sub-micron wires have also been fabricated, there are still issues with wire continuity and thus, electrical conductivity. Further development in our lithographic processing is expected to enable the fabrication of $\sim$500 nm conducting metal wires on the colloidal crystal surfaces.

5. Microscale template structure for colloidal crystals using 3D lithography

So far we have only discussed results where the PS colloidal crystals were deposited on large areas everywhere on the substrate. This may not be practical for eventual devices, where we would like to control the placement of the crystals on the chip, and also have the metal wiring routed from the surface of a colloidal crystal to an area on the chip without the colloids, where wire bonding would be performed (wire bonding is not easily possible on the soft PS colloidal film). There are several methods to lithographically control the deposition of colloidal crystals, such as by engineering contrast in the hydrophilicity of

the substrate [29, 22] or the local evaporation rate [30], or by a simple spatial confinement by patterned topographic structures [31, 32, 33, 34, 20]. Here we follow the route of topographic patterning, but in contrast to many previous studies, we want to control very thick colloidal crystals of the thickness range 10 - 20 μm. This is about the same thickness as in Refs. [31] and [32], but in contrast to Ref. [31] and our own previous work [20], we do not use deep etching in Si, but want to pattern a negative photoresist on glass substrates as an additive process, as in Ref. [32].

2D photolithographic patterning of negative photoresists such as SU-8, on the other hand, is naturally limited to simple 2D structures [32]. Here, we use three-dimensional patterning to create more complex, fully 3D shapes. This is possible with the help of direct laser-write lithography using two-photon absorption [35], where infrared light at 780 nm is focussed tightly with the help of a microscope. Only at the very focus of the beam two-photon absorption takes place, where the simultaneous absorption of two IR photons can excite the photoresist the same way as a single UV photon at 390 nm [19]. The patterning was performed with the instrument by Nanoscribe GmbH using the standard mode, where the laser beam was focused through a glass substrate onto a liquid polymer resist drop on the opposite surface.

The design of the structure is shown in Figure 6. It is a square shaped box of height 10 μm, with inside, "container area" dimensions 100 μm $\times$ 100 μm, surrounded by walls of width 25 μm which are themselves made from hollow beam structures for structural rigidity and ease of fabrication. Outside walls connect to sloped regions of angle 45 degrees, the purposes of which are to i) attach the box structure more securely to the substrate, and ii) to allow the eventual routing of metal wiring from the substrate surface, where the bonding pads will be located, to the top of the box structure. The SEM image shows that some distortion of the shape is observable, due to mechanical forces created by the shrinking of the IPL780 photoresist (Nanoscribe GmbH) during development. This slight distortion can, however, be improved by design improvements in the future.

With the support box available, we deposited PS colloidal crystals into them by the vertical dipping technique, using 1 % PS nano-sphere colloidal solution at a dipping speed of 0.01 mm/min. Figure 7 shows a SEM micrograph which shows part of the 3D box structure (top view) after colloidal crystal deposition. We see that crystals have been deposited inside the box, as hoped for, and the photoresist walls and slopes have no PS nanospheres on them. This is quite useful as further lithography of metal lines on the bare box structure is easier.

In addition, we make two other useful observations from Figure 7: i) Below the box structure, there is a region of bare glass substrate visible. It seems that the box structure prevented the deposition of colloidal crystal there. This kind of region can thus be used for the bonding pads and wiring, climbing over the slopes and finally onto the colloidal crystal surfaces inside the box. ii) The colloidal crystals can be in contact with the box inside wall (inset), without a significant crack. This is in contrast with our earlier work with etched silicon boxes [20], where cracks were always observed between

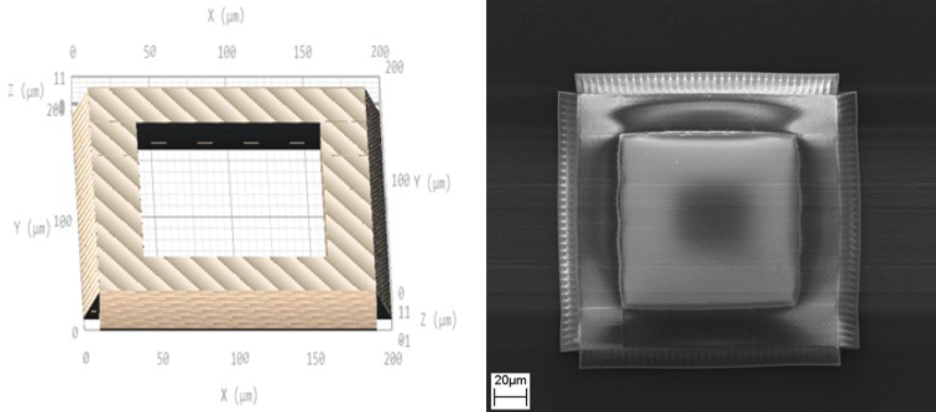

Figure 6: The design of the 3D resist box. Left: schematic design, with walls and slopes surrounding outside walls. Right: SEM micrograph of a fabricated structure from top view.

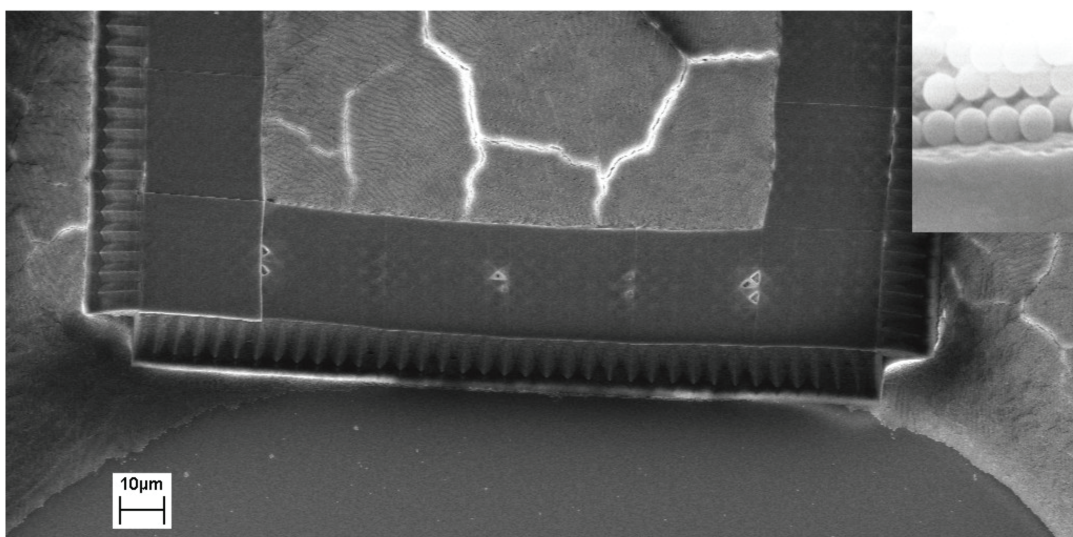

Figure 7: SEM image of PS colloidal crystals deposited on the 3D lithographically fabricated photoresist box structure. Inset: a zoom in of an area at the inside edge of the box.

the box wall and colloidal crystal. However, cracks were clearly observable inside the box structure. It is of course possible to reduce the lateral size of the box in the future to such a degree that only a single domain would fit inside.

To further prove that the routing of wires from a polymer box structure onto the colloidal crystal is possible, we also fabricated another device where 3 μm wide Al wiring of thickness 100 nm was deposited on a box structure of size 50 $\times$ 50 μm, containing a 10 μm thick PS colloidal crystal deposited by vertical dipping solely into the box container area, shown in a SEM micrograph in Fig. 8. For the fabrication of the structure in Fig. 8, all the techniques described earlier had to be combined, i.e. fabrication of a photoresist

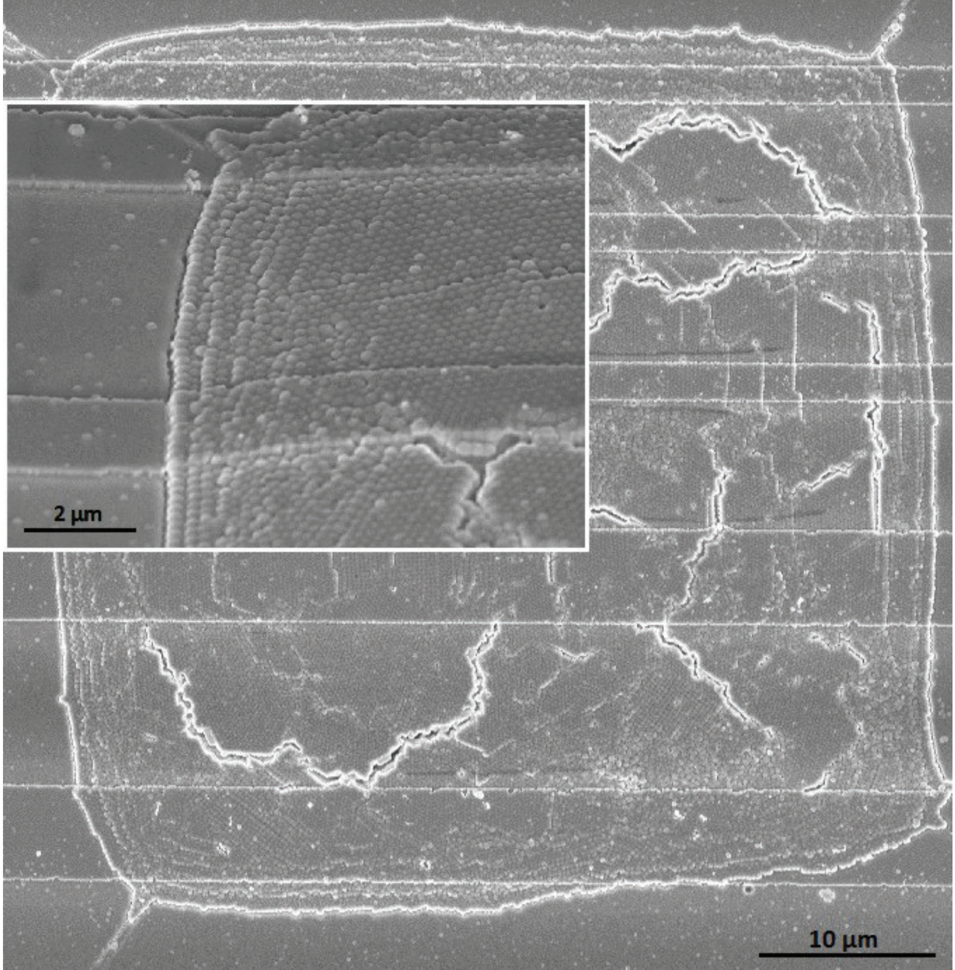

Figure 8: SEM image of 2 μm wide Al wiring integrated with 10 μm thick PS colloidal crystals which were deposited on a photoresist box structure of size 50 $\times$ 50 μm. The inset shows a zoomed-in image at around the edge of the box inside wall.

box structure, vertical dipping for colloidal crystal self-assembly, e-beam hardening of the PS crystal, AlOx capping layer deposition, and finally e-beam lithography of the Al line features using lift-off.

6. Conclusions

In conclusion, we have presented a versatile method for the fabrication of metallic wiring on top of polystyrene colloidal crystals, which will in the future allow for electronic devices to be processed on top of the crystals. The critical steps developed here were: i) Lithographically controlled, electron-beam induced cross-linking, to harden polystyrene colloidal crystals so that they can withstand the elevated temperatures and harsh chemicals used in electron-beam lithography. This allows standard lithographic processes to be used on top of the self-assembled polystyrene nanosphere colloidal crystals. ii) Deposition of micron-scale narrow metal wiring on top of the colloidal

crystals, and iii) Templated deposition of the colloidal crystals into pre-defined areas that can allow wiring to come from the substrate surface onto the crystals. These truly 3D shaped templates were patterned from a photoresist, using direct laser writing and two-photon absorption, which is thus a fully three-dimensional lithographic technique. The developed techniques will be used in the future to integrate heaters and thermometers on colloidal structures, which is critical for example for the future studies of phonon transport in three-dimensional phononic crystal structures. In addition, the methods developed here can be utilized in devices where complex metal structures need to be integrated with a 3D photonic crystal.

Acknowledgments

This research was supported by the Academy of Finland Project No. 260880. We thank Onni-Pekka Häkkinen and Emmi Kirjanen for fabrication assistance.

References

[1] P. Jiang, J. F. Bertone, K. S. Hwang, and V. L. Colvin. Single-crystal colloidal multilayers of controlled thickness. *Chemistry of Materials*, 11(8):2132–2140, 1999.

[2] Yurii A. Vlasov, Xiang-Zheng Bo, James C. Sturm, and David J. Norris. On-chip natural assembly of silicon photonic bandgap crystals. *Nature*, 414:289 – 293, 2001.

[3] J D Joannopoulos, Pierre R Villeneuve, and Shanhui Fan. Photonic crystals: putting a new twist on light. *Nature*, 386(6621):143–149, 1997.

[4] Younan Xia, Byron Gates, Yadong Yin, and Yu Lu. Monodispersed colloidal spheres: Old materials with new applications. *Advanced Materials*, 12:693–713, 2000.

[5] Juan F. Galisteo-Lopez, Marta Ibisate, Riccardo Sapienza, Luis S. Froufe-Perez, Alvaro Blanco, and Cefe Lopez. Self-assembled photonic structures. *Advanced Materials*, 23:30–69, 2011.

[6] Jae-Hwang Lee, Cheong Yang Koh, Jonathan P. Singer, Seog-Jin Jeon, Martin Maldovan, Ori Stein, and Edwin L. Thomas. 25th anniversary article: Ordered polymer structures for the engineering of photons and phonons. *Advanced Materials*, 26(4):532–569, 2014.

[7] T. J. Isotalo, Y. L. Tian, and I. J. Maasilta. Fabrication and modelling of three-dimensional sub-kelvin phononic crystals. *Journal of Physics: Conference Series*, 400:052007, 2012.

[8] Martin Maldovan. Sound and heat revolutions in phononics. *Nature (London)*, 503:209–217, 2013.

[9] Wei Cheng, Jianjun Wang, Ulrich Jonas, George Fytas, and Nikolaos Stefanou. Observation and tuning of hypersonic bandgaps in colloidal crystals. *Nature Materials*, 5:830 – 836, 2006.

[10] J. Tang, H.-T. Wang, D.H. Lee, M. Fardy, Z. Huo, T.P. Russell, and P. Yang. Holey silicon as an efficient thermoelectric material. *Nano Lett.*, 10:4279–4283, 2010.

[11] J.-K. Yu, S. Mitrovic, D. Tham, J. Varghese, and J.R. Heath. Reduction of thermal conductivity in phononic nanomesh structures. *Nat. Nanotech.*, 5:718–721, 2010.

[12] S. Alaie, D.F. Goettler, M. Su, Z.C. Leseman, C.M. Reinke, and I. El-Kady. Thermal transport in phononic crystals and the observation of coherent phonon scattering at room temperature. *Nat. Commun.*, 6:7228, 2015.

[13] Nobuyuki Zen, Tuomas A. Puurtinen, Tero J. Isotalo, Saumyadip Chaudhuri, and Ilari J. Maasilta. Engineering low-temperature thermal conductance using a two-dimensional phononic crystal. *Nature Communications*, 5:3435, 2014.

[14] Tuomas A. Puurtinen and Ilari J. Maasilta. Low-temperature coherent thermal conduction in thin phononic crystal membranes. *Crystals*, 6:72, 2016.

[15] R. Anufriev, J. Maire, and M. Nomura. Reduction of thermal conductivity by surface scattering of phonons in periodic silicon nanostructures. *Phys. Rev. B*, 93:045411, 2016.

[16] R. Anufriev and M. Nomura. Reduction of thermal conductance by coherent phonon scattering in two-dimensional phononic crystals of different lattice types. *Phys. Rev. B*, 93:045410, 2016.

[17] Wolfram Schnabel and Hideto Sotobayashi. Polymers in electron beam and x-ray lithography. *Progress in Polymer Science*, 9(4):297 – 365, 1983.

[18] R. L. Clough. High energy radiation and polymers: A review of commercial processes and engineering applications. *Nuclear Instruments and Methods in Physics Research B*, 185:8–33, 2001.

[19] Markus Deubel, Georg von Freymann, Martin Wegener, Suresh Pereira, Kurt Busch, and Costas M. Soukoulis. Direct laser writing of three-dimensional photonic-crystal templates for telecommunications. *Nature materials*, 3:444–447, 2004.

[20] Tero J. Isotalo, Yao-Lan Tian, Mikko P. Konttinen, and Ilari J. Maasilta. Statistical characterization of self-assembled colloidal crystals bysingle-step vertical deposition. *Colloids and Surfaces A: Physicochemical and Engineering Aspects*, 443:164–170, 2014.

[21] Zhong-Ze Gu, Akira Fujishima, and Osamu Sato. Fabrication of high-quality opal films with controllable thickness. *Chemistry of Materials*, 14:760–765, 2013.

[22] Charles-Andre Fustin, Gunnar Glasser, Hans W. Spiess, and Ulrich Jonas. Parameters influencing the templated growth of colloidal crystals on chemically patterned substrates. *Langmuir*, 20:9114–9123, 2004.

[23] Robert G. Shimmin, Alexander J. DiMauro, and Paul V. Braun. Slow vertical deposition of colloidal crystals: A langmuir-blodgett process? *Langmuir*, 22(15):6507–6513, 2006.

[24] Subbian Karuppuchamy and Jae Mun Jeong. Super-hydrophilic amorphous titanium dioxide thin film deposited by cathodic electrodeposition. *Materials Chemistry and Physics*, 93(2–3):251 – 254, 2005.

[25] R. Ranby and J. F. Rabek. *Photodegradation, Photo-oxidation and photostabilization of polymers*. John Wiley and Sons, New York, 1975.

[26] Lei Li, Caikang Chen, Aijuan Zhang, Xinyu Liu, Kun Cui, Jin Huang, Zhi Ma, and Zhaohui Han. Fabrication of robust honeycomb polymer films: A facile photochemical cross-linking process. *Journal of Colloid and Interface Science*, 331(2):446 – 452, 2009.

[27] Marta Palacios, Olga Garca, and Juan Rodrguez-Hernndez. Constructing robust and functional micropatterns on polystyrene surfaces by using deep uv irradiation. *Langmuir*, 29(8):2756–2763, 2013. PMID: 23363393.

[28] Siqi Ma, Celal Con, Mustafa Yavuz, and Bo Cui. Polystyrene negative resist for high-resolution electron beam lithography. *Nanoscale Research Letters*, 6(1):1–6, 2011.

[29] C.-A. Fustin, G. Glasser, H.W. Spiess, and U. Jonas. Site-selective growth of colloidal crystals with photonic properties on chemically patterned surfaces. *Advanced Materials*, 15(12):1025–1028, 2003.

[30] Daniel J. Harris, Hua Hu, Jacinta C. Conrad, and Jennifer A. Lewis. Patterning colloidal films via evaporative lithography. *Phys. Rev. Lett.*, 98:148301, Apr 2007.

[31] P Ferrand, M J Minty, M Egen, J Ahopelto, R Zentel, S G Romanov, and C M Sotomayor Torres. Micromoulding of three-dimensional photonic crystals on silicon substrates. *Nanotechnology*, 14(2):323, 2003.

[32] Jian Xu, Eoin S. O'Keefe, and Carole C. Perry. Opaline films on patterned substrates by a simple self-assembly method. *Materials Letters*, 58(2728):3419 – 3423, 2004.

[33] Shih-Kai Wu, Tzu-Piao Tang, and Wenjea J. Tseng. Self-assembly of polystyrene microspheres within spatially confined rectangular microgrooves. *Journal of Materials Science*, 43(19):6453–6458, 2008.

[34] Lidiya Mishchenko, Benjamin Hatton, Mathias Kolle, and Joanna Aizenberg. Patterning hierarchy in direct and inverse opal crystals. *Small*, 8(12):1904–1911, 2012.

[35] Satoshi Kawata, Hong-Bo Sun, Tomokazu Tanaka, and Kenji Takada. Finer features for functional

microdevices. *Nature*, 412:697–698, 2001.